Current Ground Deformation Derived from GPS Observations near PBO Station AC 55 along the Yentna River, South of Denali National Park Reserve, Alaska

A Thesis Presented to

the Faculty of the Department of Earth and Atmospheric Science

University of Houston

In Partial Fulfillment

of the Requirements for the Degree

Master of Science

by

Yanet Cuddus

May, 2015

Current Ground Deformation Derived from GPS Observations near PBO Station AC 55 along the Yentna River, South of Denali National Park Reserve, Alaska

____

Yanet Cuddus

APPROVED:

____

Dr. Guoquan Wang, Chairperson

____

Dr. Alex Robinson

____

Dr. Craig Glennie

____

Dean, College of Natural Sciences and Mathematics

ACKNOWLEDGEMENTS

I would like to express my gratitude to several people whose contributions made this work possible. The support, instruction and guidance provided by my advisor, Dr. Guoquan Wang, has been invaluable. His oversight was essential in the development and execution of this project. In addition, I would like to thank Dr. Alex Robinson (Department of Earth and Atmospheric Science) and Dr. Craig Glennie (UH Department of Civil Engineering), who not only oversaw this project as committee members, but were integral in refining the project scope. I thank them for their guidance, insight, instruction, and unrelenting patience.

I am also thankful to my colleagues in the Geodesy Lab who have helped me in so many ways, from hardware and software assistance to being a supportive sounding board on my path of knowledge. I would like to thank my dearest friends– who have all demonstrated extreme patience and support on what felt like an endless journey. My deepest thanks are reserved for my family. To my parents thank you for your love and support throughout my life. Dad, thank you for your constant encouragement, the technical curiosity and ambition you passed down to me, and your unwavering support. Mom, thank you for showing me how to sacrifice everything in order to achieve your goal, and to have the courage to never give up.

To all those I have unintentionally forgotten, thank you.

Current Ground Deformation Derived from GPS Observations near PBO Station AC 55 along the Yentna River, South of Denali National Park Reserve, Alaska

An Abstract of a Thesis
Presented to
the Faculty of the Department of Earth and Atmospheric Science
University of Houston

In Partial Fulfillment
of the Requirements for the Degree
Master of Science

by
Yanet Cuddus
May, 2015

ABSTRACT

The Plate Boundary Observatory (PBO) has a network of 1100 permanent continuously operating Global Positioning System (GPS) stations, of which approximately 200 are located in Alaska. GPS station AC55 was accidently installed on a slow moving landslide. In order to isolate the landslide motion, this study uses 20 stations within 100 km proximity of AC55 to separate regional ground motion associated with seasonal variability and postseismic deformation from the 2002, M 7.9 Denali earthquake. Time series of motion in the horizontal and a vertical component was plotted for the entire network spanning the observation period (2002-2014). GPS observations were originally processed in IGS08. This study then established a local reference frame, which allows for intra-regional deformation analysis on areas of interest located within the local reference frame. From these measurements, a baseline of the relative motion located outside of the landslide body was calculated. The seasonal variability due to hydrological loading and the regional tectonic motion were calculated and removed. Hence the pure relative motion associated with the landslide event was derived.

The relatively stable local reference frame is able to provide an accuracy of ± 1.5 mm/year for local ground motion. The results show that PBO station AC55 moves with a steady horizontal velocity of 5.5 cm/year toward N 75° E, and has a subsidence rate of 2.6 cm/year. The mechanism of the steady displacement velocity at AC55 is not fully understood and requires geotechnical field investigation to understand the kinematics of the landslide motion.

More broadly, this GPS signal processing method has wider application allowing researchers to conduct precise landslide monitoring in remote regions using long-history (>5 years) GPS stations.

TABLE OF CONTENTS

LIST OF FIGURES

LIST OF TABLES

1 INTRODUCTION

Over the last three decades, advancements in technology have resulted in an explosion in observational research and significant advancements in geodesy. This has resulted in an unprecedented accuracy and coverage of spatial and temporal data. The Global Positioning System (GPS) has become a primary scientific tool used in the detection of earth mass movements associated with earthquakes, plate movements, fault motions, volcanoes, subsidence, and landslides. The rapid addition of GPS stations in Alaska after the Denali Earthquake in 2002 improves the accuracy of GPS position data by increasing the sampling, identifying signal noise and correcting common errors (Firuzabadí and King, 2012).

The purpose of this study is to inspect the surficial deformation associated with the slow landslide event recorded at the UNAVCO PBO GPS station Yentna_rvrak2006 (AC55) covering the period from August 25, 2006 to July 10, 2010. The study area is along the southern slope of Denali National Park surrounding the Cook Inlet Watershed (Fig. 1.1; Fig. 1.2), which is referred to as the Greater Cook Inlet Basin. Twenty GPS stations within the study area were inspected. This study investigated a landslide event in an area undergoing post-seismic deformation resulting from the 2002 M 7.9 Denali earthquake. In order to evaluate the motion of the landslide the regional post-seismic motion needed to be dampened. Using a few of these stations that had near zero displacement, a Local Reference Frame (LRF) was established. This reference frame was used to calculate common local ground motion that was observed in all the stations within the study area. In essence the study area serves as a “fixed” zone where independent displacement and cyclical components of anomalous movements can be recovered. This study is able to derive the motion at AC55 and examine the slow landslide displacement. High-accuracy GPS techniques are able to detect slow landslide movements at a level of 1-2 mm/year within a period as short as three years (Wang and Soler 2012; Wang et al. 2014). With the added complexity of Alaska’s active tectonics and sub-arctic climate, a new method was created for GPS processing. The technique executed in this study was achieved by:

(1) Improving the quality of the GPS signal

The daily direct signals from the GPS satellites were examined, biased position data were filtered and model was created for the GPS signal variability for each GPS station in the study area.

(2) Creating a Stable Local Reference Frame

A network of GPS stations can further assist in the understanding of surface and subsurface deformation by expanding the resolution of the position data, while simultaneously improving the accuracy of these solutions (Zumberge, et al., 1997). This in essence created a proxy tectonic zone that has near zero motion within the LRF.

(3) Excluding the common motion within the Local Reference Frame

After calculating a baseline for the relative motion associated with post-seismic deformation located outside of the landslide body, and removing the seasonal variability (Watson et al., 2002; Geirsson et al., 2006) the pure relative motion associated with the landslide event was derived (Wang et al., 2015).

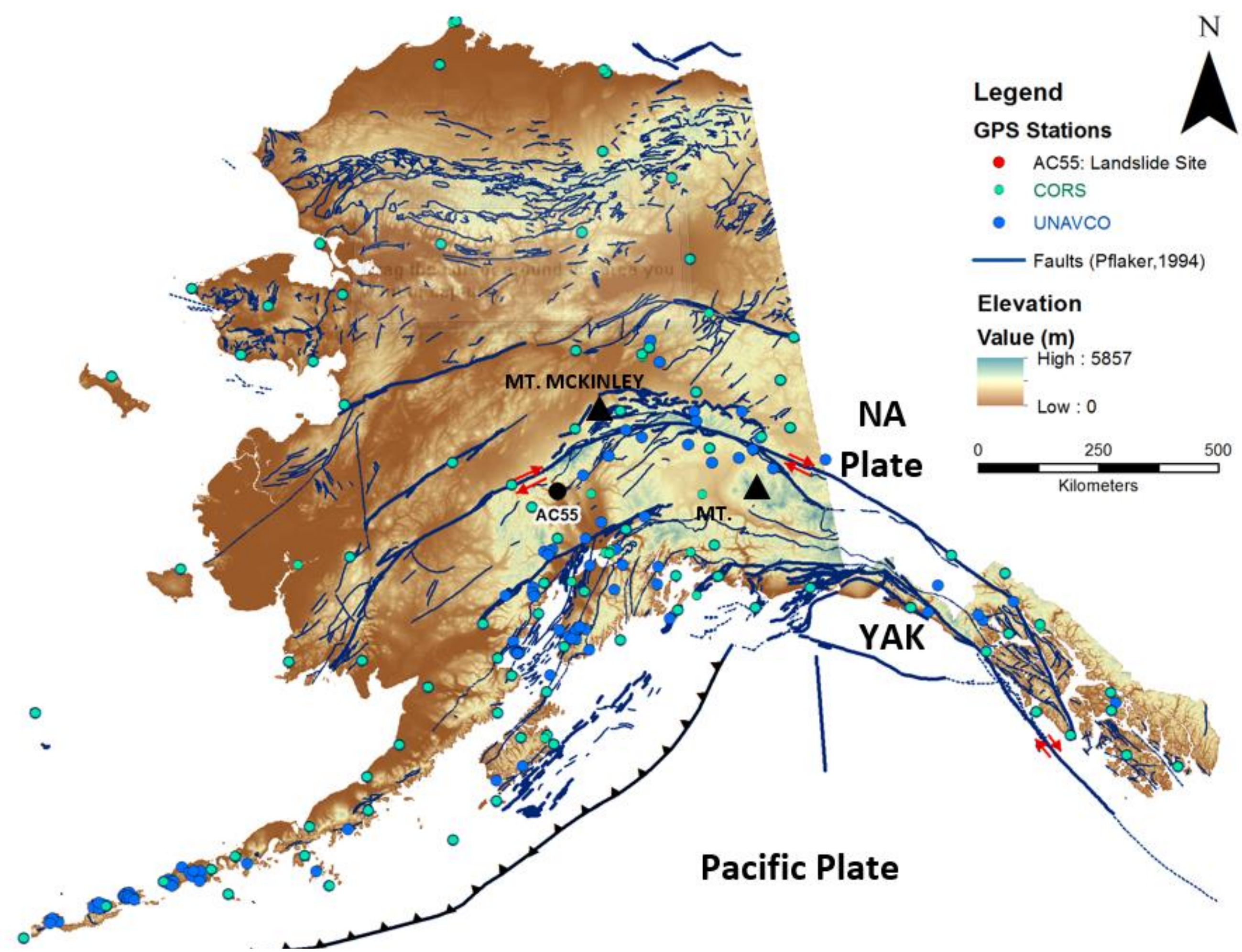

Figure 1.1: Alaska Regional Map. Shows the dense network of GPS stations, location of the landslide site (black dot, AC55) and major regional faults. A more detailed view of the study area is illustrated in Figure 1.2 (Data for the map was gathered from the USGS, and the fault locations were digitized after Pflaker, et al., 1994).

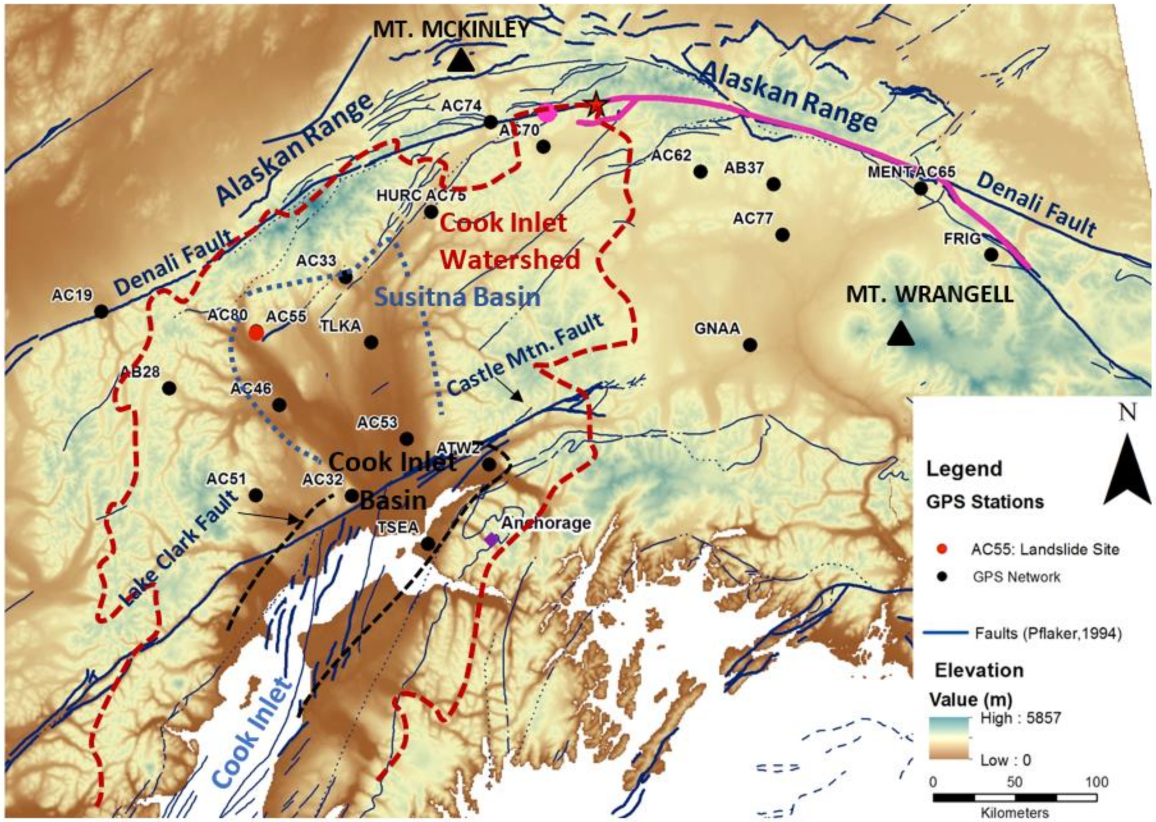

Figure 1.2: Study Area Locator Map. Shows the location of the landslide site (red dot, AC55) and regional faults. The study area surrounds the Cook Inlet Watershed (the Greater Cook Inlet Basin), which is composed of the Cook Inlet and Susitna Basins. The pink dot represents the M6.7 October 23 foreshock event, the red star represents the epicenters of the 2002 Denali earthquake (M7.9) and the purple line represents the fault rupture (Data for the map was gathered from the USGS, and the fault locations were digitized after Pflaker et al., 1994).

2 BACKGROUND

2.1 TOPOGRAPHY

The area of interest has an elevation range from sea level to 1,400m. The topography ranges from the Susitna Lowlands which are characterized by moraines, outwash plains, and a relief of 15-75 meters (50-250 ft.) to the extremely high rugged Alaskan Range which is characterized by glaciated ridges with an average relief of 1.8-2.7 km (6,000-9,000 ft.) (Fig. 1.2). The glaciers of the Alaskan Range are the headwaters of the braided Susitna River.

2.2 CLIMATE

The Greater Cook Inlet Basin has three climate zones due to its large size and range in altitude (Brabets et al., 1999). The study area straddles two zones, the Continental Zone and the Transitional Zone. The Continental Zone is characterized by an average annual precipitation of about 75 cm (30 in.) and an average temperature of about -5°C. Average annual precipitation in the Transition Zone is about 150 cm (60 in.) and temperatures average about -3 °C (Brabets et al., 1999). The location at AC55 is characterized by 175 cm (70 in.) in mean annual precipitation and an annual mean temperature -5°C to 0°C; winter average air temperatures are approximately -10°C.

2.3 HYDROLOGY

The Greater Cook Inlet Basin consists of four major drainage areas; the one relevant to this study is the Susitna River Basin (Brabets et al., 1999). Susitna River Basin is the largest basin surrounding Cook Inlet (53,747 km^2 or 20,752 mi^2) and happens to be the fifth largest basin in Alaska (Brabets et al., 1999). The elevation within the Susitna River Basin has a large contrast, ranging from 6,194 meters (20,320 ft.) at Mt. McKinley to sea level where the Susitna River empties into Cook Inlet (Brabets et al., 1999). In the high, mountainous areas that surround the Greater Cook Inlet Basin, most of the precipitation is in the form of snow and ice (Brabets et al., 1999). Glaciers store an enormous quantity of water and this feature makes any drainage basin containing glaciers complex. This complexity adds a great deal of uncertainty in modeling ground surface motion due to the interannual variations in the horizontal component as well as the annual variations in the vertical component.

2.4 GLACIOLOGY

Central to Southern Alaska has been dominated by Holocene glacial fluctuations (Barclay et al., 2009). Approximately 10,800 km^2, or 11 percent of the Greater Cook Inlet Basin is covered by temperate glaciers (Brabets et al.,1999). Glaciers are presently found in western Cook Inlet and the Alaska Range (Brabets et al., 1999). Most of the glacial mass (727,800 km^2) during the last glacial maximum was located in this region (Barclay et al., 2009). Due to the glacial retreat late in the Pleistocene the current glacial mass is about 74,700 km^2 (Barclay et al., 2009). Southern Alaska has experienced considerable ice volume loss (approximately 90%) and this results in ongoing isostatic rebound (Brabets et al., 1999). The extensive rebound results in large vertical motions, which can be seen in GPS data, and often overshadows the tectonic subsidence. Sauber and Molnia (2004) modelled the glacial mass fluctuations in Southern Alaska. This model predicted the surface displacements north of ice thickness change were upward and trends northward; whereas just south of the ice change region surface displacements were directed upward and trends southward (Sauber and Molnia, 2004).

2.5 ECOLOGY

There is a connected feedback relationship between ecology and landslides, which must be examined in order to understand slope stabilization, landslide prediction, and mitigation. Landslide probability variables can be grouped into two categories: (1) the “stable state” variables which make the slope susceptible to failure (without actually initiating it) such as geology, slope gradient and aspect, elevation, soil/bedrock geotechnical properties, vegetation cover, and long term drainage patterns and weathering; and (2) the triggering variables that initiate failure in an area of given susceptibility, such as heavy rainfall and earthquakes (Dai et al., 2002). The “stable state” variables of interest are related to the loss of material strength (geotechnical properties) due to weathering of the bedrock, snowmelt, and permafrost contributions to the drainage patterns.

AC55 is located on a bedrock, therefore the active soil layer will be very thin. The dominant soil suborder in the vicinity of AC55 (along the Alaskan Range) is classified as Pergelic Haplocryods. The dominant feature of these soils is the presence of permafrost, which restricts moisture movement through the soil as well as plant root penetration, and become unstable if allowed to warm and thaw (Brabets et al., 1999).

2.5.1 PERMAFROST

A significant factor that contributes to landslides in alpine regions is permafrost degradation. Permafrost units at depths have thermal complexity which induce a loss of material strength. Studies dating back to the 1990s in central Alaska documented that permafrost degradation is widespread and rapid (Jorgenson et al., 2008a). The degradation of permafrost can lead to large changes in ecosystems. Alpine permafrost may be degrading under the present warmer climate, reducing soil/bedrock cohesion, and thus decreasing slope stability (Haeberli et al., 1990; Harris et al., 2001). Jorgenson et al. (2008a) studied the changes to the ecosystem in central Alaska as a result of permafrost degradation and thermokarst (karst-like hollows produced by melting permafrost) development. According to Jorgenson et al.'s (2008a) classification, the location of the landside at AC55 (Fig. 2.1) is categorized as being in a discontinuous permafrost area associated with a retrogressive thaw slump. Retrogressive thaw slumps (RTS) are slope failures resulting from thawing of ice-rich permafrost (Fig. 2.3). These lateral thermokarst features develop along streams or coastlines and expand inland to form landslide-like U-shaped scars (Lantuit et al., 2013).

Permafrost degradation also affect alpine bedrock due to the presence of ice lenses and ice filled fracture joints (Gruber and Haeberli, 2007). Ice-filled joints are abundant in bedrock permafrost and lead to destabilization (Fig. 2.2; Fig. 2.3) as a result of warming (Gruber and Haeberli, 2007).

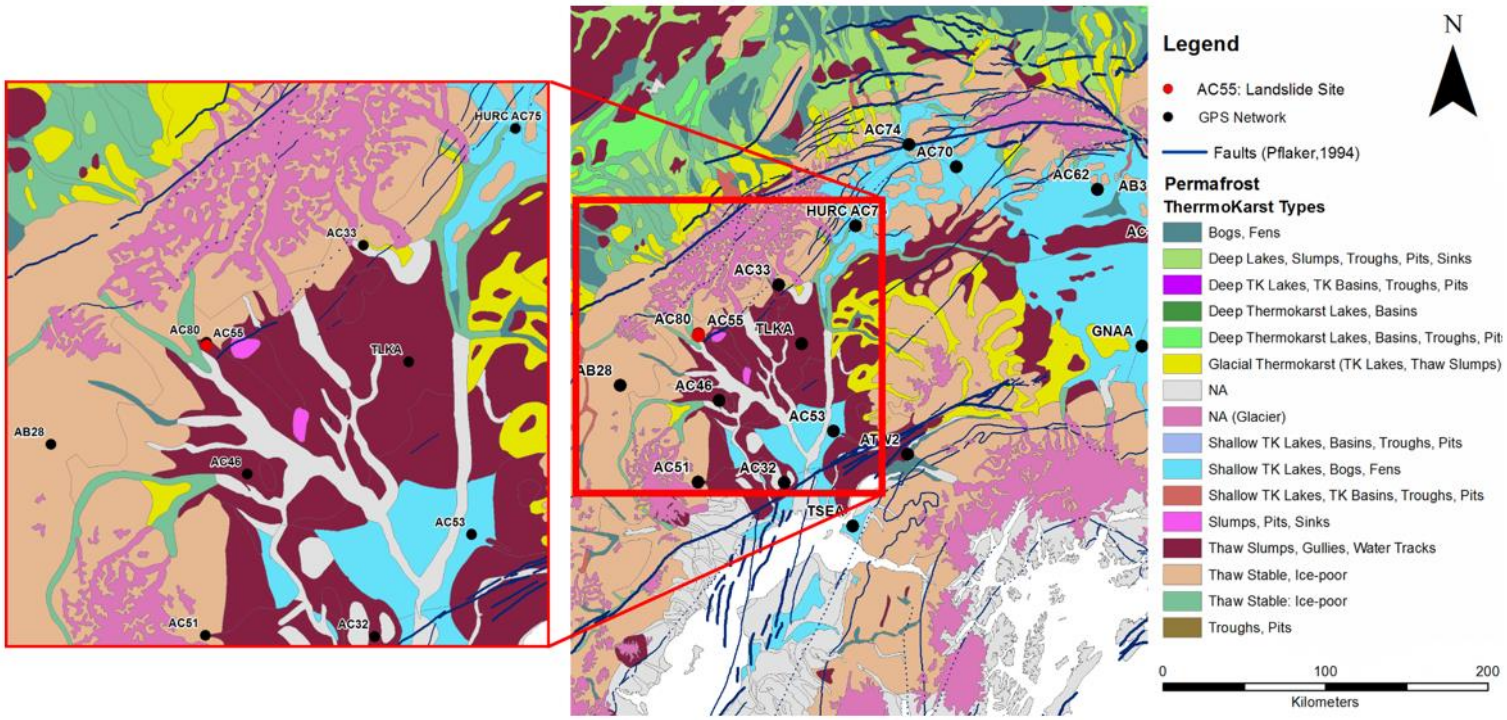

Figure 2.1: Permafrost Coverage Map. Massive permafrost covers over a great majority of the region, the enlarged view on the left focuses attention around AC55. Regional permafrost degradation, particularly the formation of thermokarst features, contributes to slope instability (Jorgenson et al., 2008a; Harris et al., 2001). An example can be seen in the insert, where a thermokarst pit has formed a minor fault, approximately 6 km S 45° E of AC55 (Data for the map was gathered from Jorgenson et al., 2008a).

2.5.2 SLOPE FAILURE CLASSIFICATION

Due to the thermal complexities, landslides in permafrost regions require a special slope failure classification (McRoberts and Morgenstern, 1974a; McRoberts and Morgenstern, 1974b; Darrow et. al., 2012).

1. Flow

A flow is broadly defined as a mass (composed of earth or debris) that behaves like a viscous fluid while moving downslope (McRoberts, 1978). These types of movement are commonly associated with the warming and/or thawing of permafrost (Darrow et. al., 2012).

2. Slide

A slide occurs when a rigid body of mass (composed of earth, debris or rock) moves as a coherent mass downslope. Additionally, slides are attributed to shear failure within frozen bedrock (McRoberts and Morgenstern, 1974a; McRoberts and Morgenstern, 1974b; Darrow et. al., 2012).

a. A ‘‘block slide’’ is a single large coherent mass that moves out and down with some degree of back-tilting near the head and continues to support living vegetation on its surface (Darrow et. al., 2012).

b. A ‘‘multiple retrogressive slide’’ consists of a series of blocks that step backward and upward to the highest head scarp (McRoberts and Morgenstern, 1974a). McRoberts (1978) indicated that the term ‘‘rotational slide’’ should be reserved for instances occurring in completely thawed material (earth, debris or rock) (Darrow et. al., 2012).

3. Falls

Falls occur when the mass travels most of the distance in the air (Darrow et. al., 2012).

4. Creep of frozen ground

The slow deformation that results from long-term application of a stress too small to produce failure in the frozen material (NSIDC, 2015).

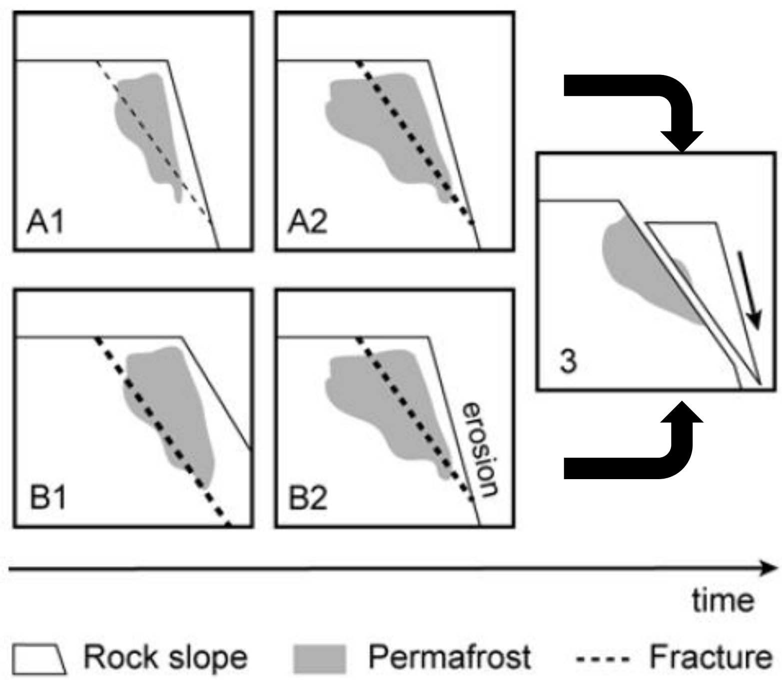

Figure 2.2: Slope Failure during Permafrost Degradation. Two scenarios that can precede the destabilization of a slope by permafrost warming are proposed: A slope with a stable fracture freezes (scenario A1) that is then widened by ice segregation (scenario A2). A slope with a stable fracture freezes (scenario B1) and is subject to stability-relevant modifications to the geometry (scenario B2). Both scenarios result in slope failure (3) (Gruber and Haeberli, 2007).

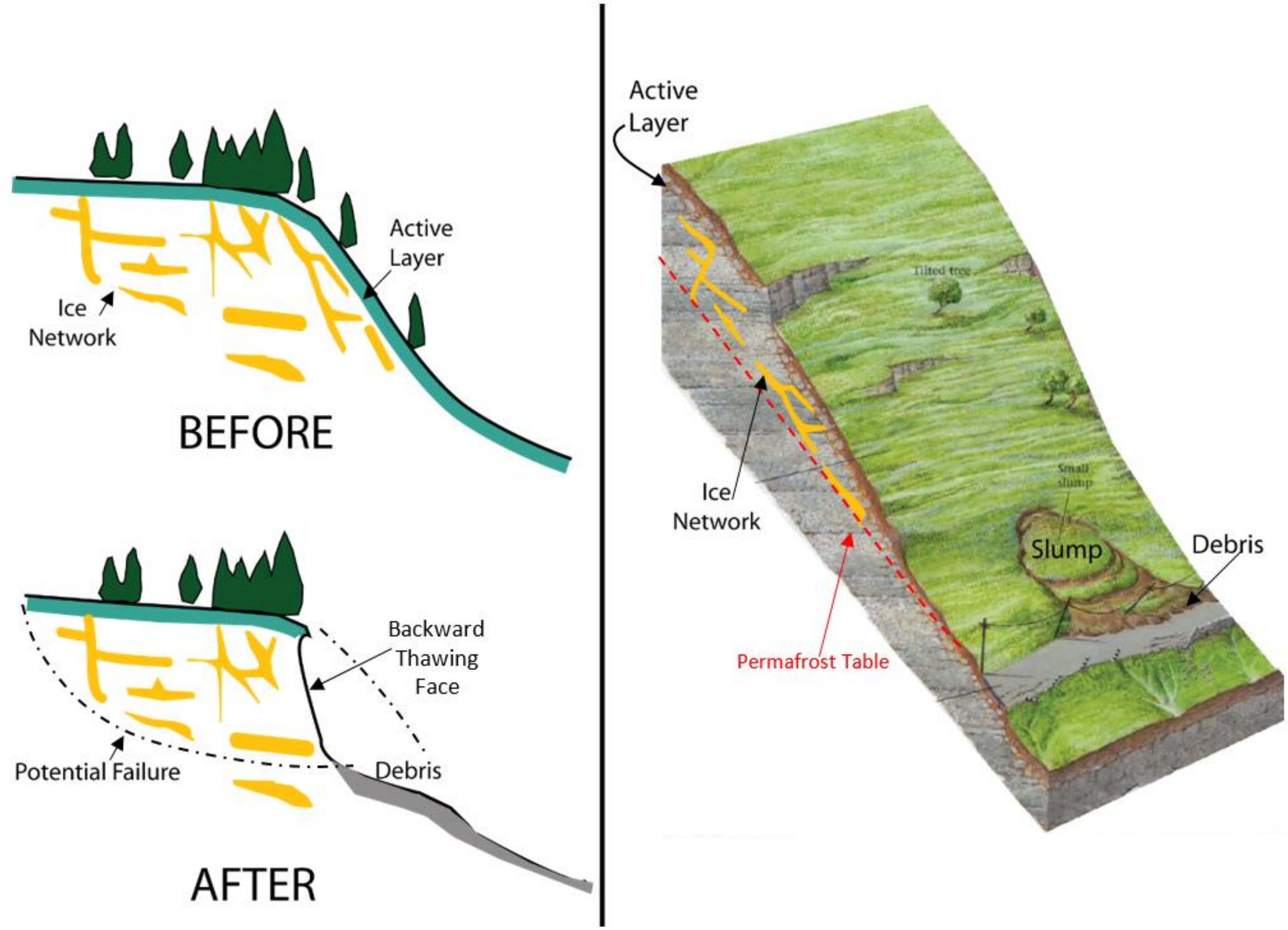

Figure 2.3: Proposed Slope Mechanisms at AC55. (A) Cross-section of permafrost retrogressive thaw slump (modified from AGU, 2015). As the permafrost ice lenses melt, fracture joints will enlarge and connect. That could create a potential failure surface that may result in a failure event. (B) Creep of frozen ground. Slow landslide motion due to permafrost thaw.

2.6 GEOLOGY AND TECTONICS

The study area (Fig. 1.2) is a mosaic of bedrock geology (Silberling et al., 1994) separated into four main terranes: the Chugach, Peninsular, Kahiltna, and Wrangellia terranes (Fig. 2.4). These terranes and their relative motion provide a framework for the tectonic evolution of the region.

Southern Alaska acts as a diffuse plate boundary, where convergence between the Pacific and North American plates is accommodated both along the Aleutian megathrust and by translating strain more than 600 km into central Alaska (Fig. 1.1) (Bemis et al., 2012). Two major collisional events define the tectonic evolution of this region: the Mesozoic collision of the Wrangellia composite terrane and the Cenozoic collision of the Yakutat terrane (Haeussler et al., 2000; Trop and Ridgway, 2007).

2.6.1 TERRANE COLLISIONS AND ACCRETION

The geologic setting of Southern Alaska is a result of multiple tectonic terrane accretion and collision events from the Jurassic to Cenozoic (Fig. 2.4). This study focuses on four terranes that consist of the Kahiltna terrane or the Wrangellia composite terrane. The Kahiltna terrane consists largely of basinal deposits and the Wrangellia composite terrane consists of mafic deposits (Silberling et al., 1994). The Wrangellia composite terrane consists of the Wrangellia terrane (Jurassic), the Peninsular terrane and the Chugach terrane (Triassic) (Silberling et al., 1994).

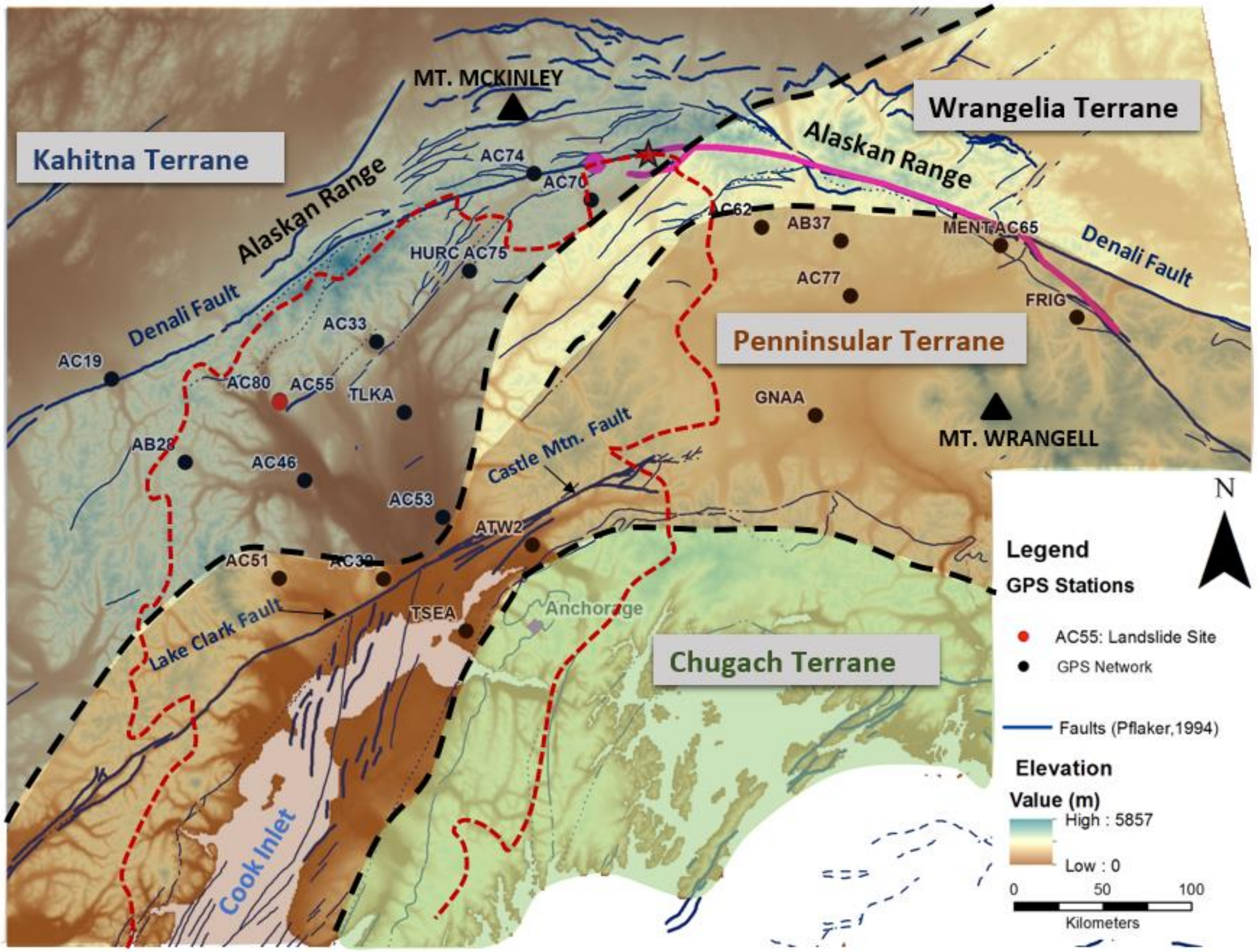

Figure 2.4: Terrane Locator Map. Modified location map identifying the approximate boundary location of the four terranes surrounding the Greater Cook Inlet Basin (Brabets et al., 1999). Shows the location of the landslide site (red dot, AC55) and regional faults. The pink dot represents the M6.7 October 23 foreshock event, the red star represents the epicenters of the 2002 Denali earthquake (M7.9) and the purple line represents the fault rupture (Data for the map was gathered from the USGS, and the fault locations were digitized after Pflaker, 1994).

2.6.2 MAJOR FAULTS

The study area is bound by two major fault systems, to the north the Denali fault and to the south the Castle Mountain-Lake Clark Fault system. The Denali fault is the principal intracontinental strike-slip fault of interior Alaska identified with the Yakutat plate convergence zone. Long strike-slip faults are common along continental plate boundaries (e.g. the San Andreas in California or the North Anatolian in Turkey) and can produce large shallow earthquakes (Eberhart-Phillips et al., 2013). The Denali fault is integral to this study and many researchers have been examining the relative motion and importance of the Denali fault. Reed and Lanphere (1973) found evidence of at least 38 km of total displacement in the past 38 m.y. (Matmon et al., 2006). In addition, field measurements found recent displacement of 3–4 km during the Pleistocene and Holocene (Richter and Matson, 1971; Plafker et al., 1978) More recently, field measurements of Quaternary features indicate that the Denali slip rate is 8-13 mm/yr., while GPS measurements indicate 8-9 mm/yr. slip (Eberhart-Phillips et al., 2013)

The Castle Mountain - Lake Clark fault system (Fig. 1.2), is a southwest-dipping, oblique right-lateral strike-slip fault. The Castle Mountain portion of the fault shows evidence of Holocene faulting and has a maximum slip rate of 3.6 to 2.8 mm/yr. (Kalbas et al., 2008). The Lake Clark portion of the fault has had ~26 km of offset in the last ~ 35 Ma. (Haeussler et al., 2000; Haeussler and Saltus, 2004) and has a slip rate of 0.67- 0.76 mm/yr. (Kalbas et al., 2008).

2.7 EARTHQUAKES

Alaska's vast network of faults is a result of tectonic activity. Since 1964, there have been ~ 2,600 M5+ earthquakes (West et al., 2014). Alaska experiences magnitude 6-7 earthquakes at least 5 times a year and a magnitude 8 about every 13 years (State of Alaska, 2014). All of the activity is due to the North American plate colliding with the Pacific Plate (Fig. 1.1), producing some of the world's largest earthquakes including the 1964 Prince William Sound M 9.2 earthquake. This study focuses on the events surrounding the 2002 M7.9 Denali Earthquake.

2.7.1 NENANA MOUNTAIN M6.7 QUAKE

The October 23, 2002 M6.7 Nenana Mountain earthquake was a foreshock event that preceded the November 3rd Denali earthquake. Both quakes occurred less than 20 km apart on the same fault (Fig. 2.5). The Nenana Mountain quake did not create surface ruptures but triggered the more powerful Denali quake (Fuis and Wald, 2003).

2.7.2 DENALI M7.9 QUAKE

The Pacific Plate is actively subducting the overriding North American Plate, and the Denali fault is accommodating significant strain due to that motion (Fig. 1.1). Prior to the 2002 earthquakes, the Denali fault was known to be seismically active, but scientists were not sure if it was capable of generating a large earthquake (USGS, 2014). Denali marks the largest quake to hit the U.S. since the 1964 M9.2 Great Alaska Earthquake.

The earthquake began at 1:12 p.m. Alaska local time, and was centered approximately 135 kilometers (84 mi.) south of Fairbanks and 283 kilometers (176 mi.) north of Anchorage (Fig. 1.2; Fig. 2.5) (USGS, 2014). It originated on the previously unknown Susitna Glacier fault, and propagated eastward along the well-known Denali fault at a speed of over 11,265 km (7,000 mi.) per hour before branching southeast onto the Totschunda fault (AEIC, 2014). The resulting surface rupture was approximately 336 km (209 mi.) long, and it cut through streams, divided forests, opened chasms in roads (Fig. 2.5), generated fault traces visible across several glaciers, and triggered thousands of landslides, especially on the steep slopes of the Alaska Range (AEIC, 2014). Like some other large earthquakes, the Denali fault quake triggered small shocks as far as 3,200 km (2,000 mi.) away (Fig. 2.5), mainly in volcanic areas (Fuis and Wald, 2003). Since the earthquake released most of its energy on the sparsely populated eastern end of the fault, Alaska's major cities were spared serious damage (AEIC, 2014; USGS, 2014).

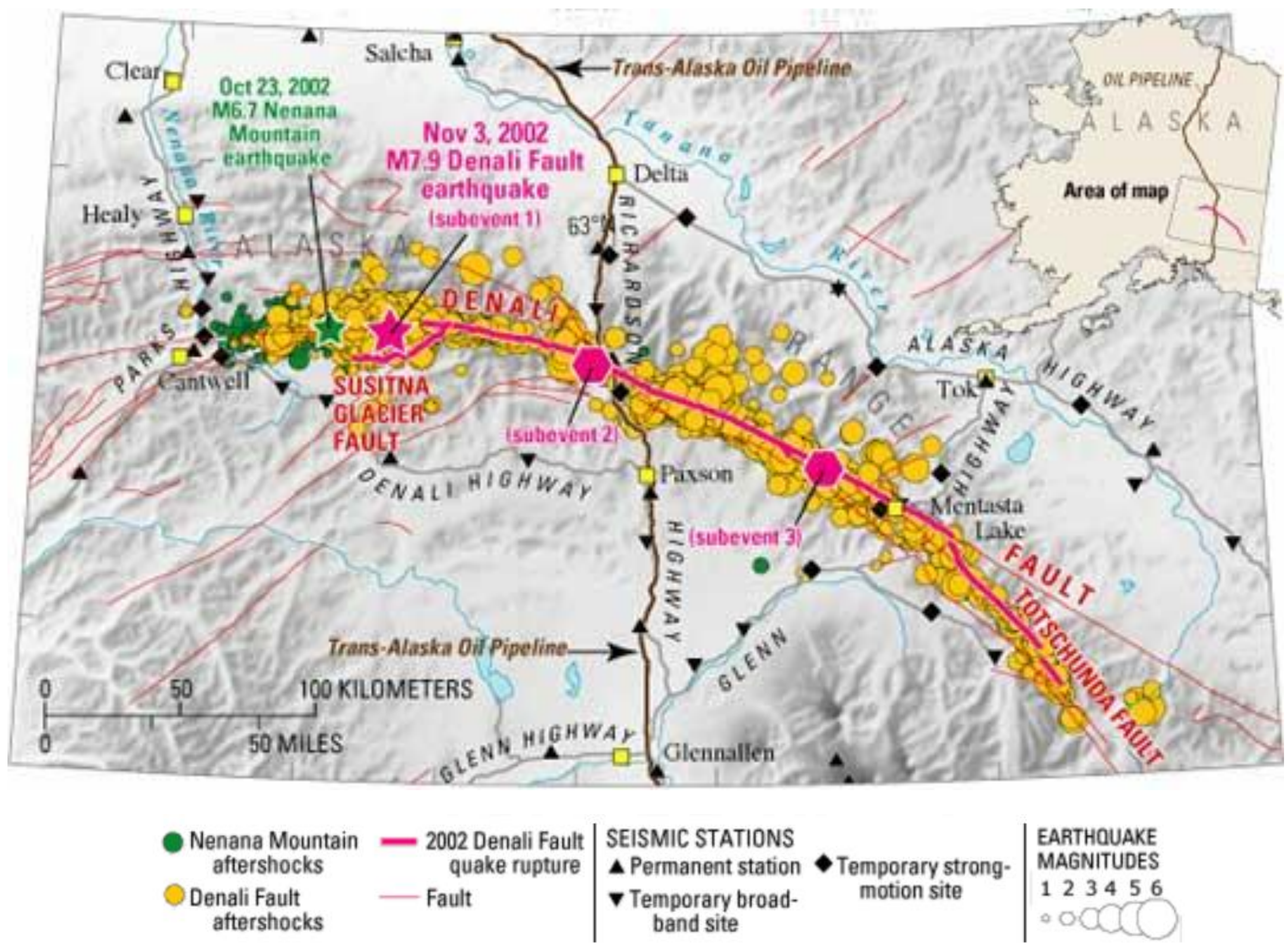

Figure 2.5: Denali Earthquake Map. This map of Susitna Glacier and the Totschunda Faults shows the locations of the October 23, 2002 and November 3, 2002 earthquakes and their aftershocks. The Denali Fault earthquake ruptured the Earth's surface for 209 miles, crossing beneath the vital Trans-Alaska Oil Pipeline, which carries 17% of the U.S. domestic oil supply. Although slightly damaged by movement on the fault and by intense shaking, the pipeline did not break in the quake, averting a major economic and environmental disaster. This success is a major achievement in U.S. efforts to reduce earthquake losses (USGS, modified from Eberhart-Phillips et al., 2003).

2.8 DEFORMATION

Alaska has a complex tectonic setting due to the dynamics of the subduction process, large-scale continental deformation, volcano deformation, and glacial isostatic loading signals (Appendix A). As a result some places experience subsidence while others are rebounding. The post-seismic deformation from the 2002 Denali earthquake affects the landslide area. Surprisingly, the 1964 Alaska earthquake continues to produce deformation after 50 years (Suito and Freymueller, 2009), and contributes considerable velocities (1-2 cm/year) to the present-day velocity field in the landslide area (Cohen and Freymueller 1997; Zweck et al. 2002; Cohen and Freymueller 2004; Suito and Freymueller 2009).

3 GPS OBSERVATIONS

3.1 DATA SOURCES

There are two main organizations that have installed GPS stations throughout Alaska, UNAVCO and NOAA (Fig. 1.1). Furthermore, the U.S. National Science Foundation (NSF) launched a large scientific program called EarthScope in 2003, which deployed thousands of seismic, GPS, and other geophysical instruments to study the structure, dynamics, and evolution of the North American continent (EarthScope, 2014). The Plate Boundary Observatory (PBO) is the geodetic component of EarthScope. PBO is operated by UNAVCO, and funded by the National Science Foundation, whose goal is to measure crustal deformation. The PBO consists of a network of about 1200 permanent GPS stations (PBO, 2014) and other instruments. In Alaska there are 210 UNAVCO installed GPS stations, of which 12 are used in this study.

The National Geodetic Survey (NGS), an office of NOAA's National Ocean Service, manages a network of Continuously Operating Reference Stations (CORS) that provide GPS data. As of January 2014, the CORS network contains more than 1,900 stations, contributed by over 200 different organizations (NGS, 2014). In Alaska, there is a network of 140 CORS GPS stations, of which 8 are being used in this study.

In the Geodetic community there are many data repositories where researchers can download raw GPS data. This study utilizes raw data from The Nevada Geodetic Laboratory (NGL) from the University of Nevada. NGL conducts research in the field of space geodesy to study tectonic problems that have both regional and global significance. NGL processed the GPS PINEX data files using the JPL GIPSY-OASIS II software. The software comparison has proven that the GPS network is producing high precision, sub-millimeter level results (NGL, 2014). NGL has reprocessed GPS data from UNAVCO, CORS and other GPS Data repositories and has aggregated the results for more than 8,000 stations.

3.2 DATA PROCESSING METHOD

There are two widely used GPS data post-processing approaches: relative positioning and absolute positioning. Relative Position Processing was historically the most precise GPS measurement technique, utilizing a processing method known as Double Differencing (DD). This technique requires a minimum of two receivers: one "rover" station with an unknown position and at least one reference station whose position is known (Soler, et al., 2001; Gao and Chen, 2004). These stations must observe identical satellites simultaneously, in order to compensate for common errors. Through the comparison of multiple series measurements made by unique receiver-satellite pairs, any mutual errors due to hardware can be differenced, and significantly reduced (Wang et al., 2013b).

Absolute Position Processing is often referred to as **P**recise **P**oint **P**ositioning (PPP) in geodetic literature, and allows users to employ the undifferenced data from a single receiver to generate positions (Gao and Chen, 2004). Zumberge, et al. (1997) explains that many aspects of the GPS system (i.e. satellite orbits and clocks) can be estimated from a global network of stations, and these estimates can be applied to individual stations, which might not have contributed to the initial estimations. This system is currently the best alternative to the double-differencing method (Wang et al., 2013b).

During this investigation, both processing methods (DD and PPP) were simultaneously analyzed (Fig. 3.1). In this study, the PPP strategy for long-term landslide monitoring is preferred. In order to highlight the advantages of the PPP method (blue plots in Fig. 3.1), landslide displacements derived (Wang et al., 2015) from the double difference (DD) method are also plotted (Fig. 3.1) for comparison. Although the double difference (DD) method generally offers higher accuracy due to simultaneous observations from two or more GPS stations, the primary disadvantage of this method is that not all the GPS stations in this study were operational for the entire observation period. In order to overcome the accuracy dilemma, a longer observation period was established (> 5 yrs.) using the absolute GPS (PPP) strategy. The PPP method is plotted using a local reference frame (Fig. 3.2; Fig. 3.3) that is explained in the next section.

The absolute positioning approach is accomplished by using the PPP method, which uses un-differenced dual frequency pseudo-range and carrier-phase observations along with precise satellite orbit and clock information to determine the position of a stand-alone GPS antenna (Blewitt et al. 1992; Zumberge et al. 1997; Kouba and Springer 2001). However, the initial positional coordinates of the PPP solutions are within the global reference frame that defines the satellite orbits. More details about these positions and the global reference frame are discussed in later sections.

The PPP method has been integrated into several scientific GPS software packages, such as the GIPSY/OASIS software developed by Jet Propulsion Laboratory (JPL) (Blewitt 1989; Webb and Zumberge 1997) and the Bernese GPS software (V5.0 or higher) developed by Astronomical Institute of the University of Berne (Dach et al. 2007; Teferle et al. 2007). This study applied the GIPSY/OASIS software package (V6.3) (https://gipsy-oasis.jpl.nasa.gov) in calculating daily GPS antenna positions, which are single receiver phase ambiguity fixed PPP solutions (Bertiger et al., 2010). According to numerous investigations, the single receiver phase ambiguity fixed PPP positions (24-hour) achieves a 2-4 mm horizontal accuracy (repeatability) and 6-8 mm vertical accuracy (Bertiger et al. 2010; Wang et al., 2013; Wang et al., 2013b).

Daily GPS solution coordinates were initially calculated in a nonfiducial reference frame employing final fiducial free ("flinnR_nf") satellite orbits and clock corrections provided by JPL (Blewitt et al. 1992; Dow et al. 2009). The loosely constrained station coordinates were then transformed to IGS08 using daily 7-parameter Helmert transformations ("x-files") provided by JPL.

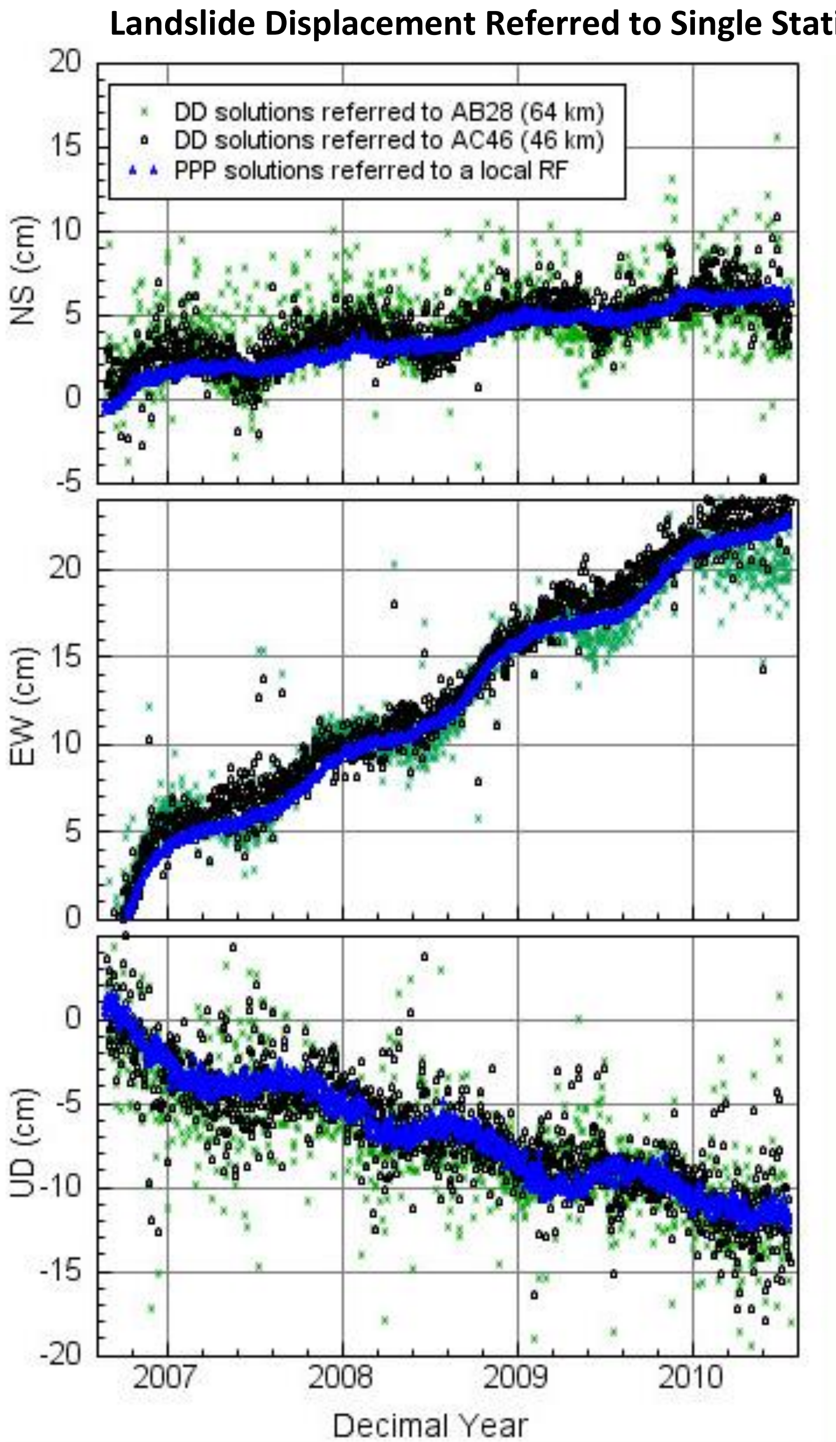

Figure 3.1: Three-component GPS antenna positional time series derived from the double difference (DD) indicating relative motion to the North (positive NS values), East (positive EW values) and vertical subsidence (negative UD values). The DD solutions are referred to two single reference stations AB28 (baseline 64 km) and AC46 (baseline 46 km). No outliers have been removed.

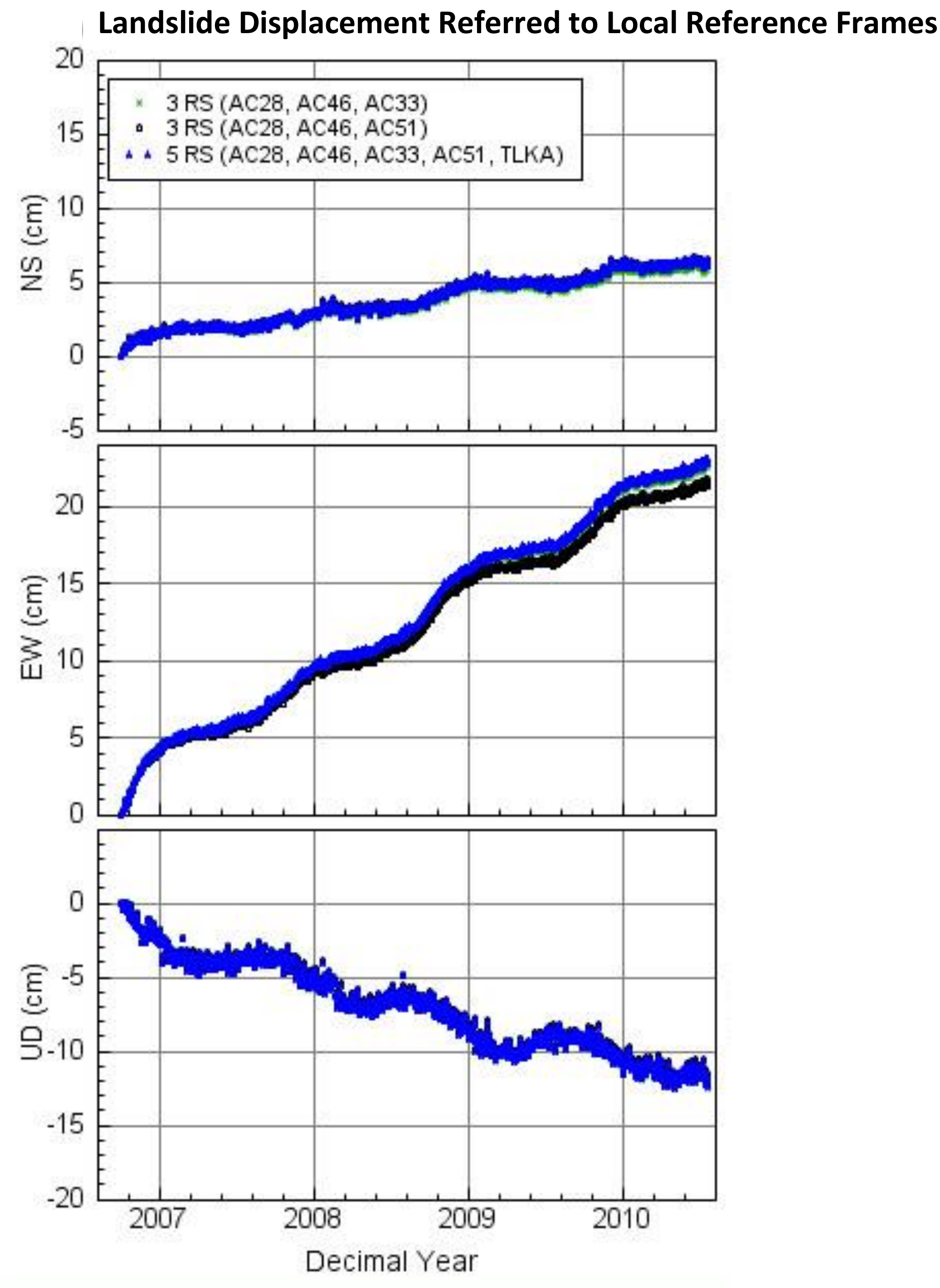

Figure 3.2: Three-component GPS antenna positional time series derived from the PPP methods. The relative motion is to the North (positive NS values), East (positive EW values) and vertical subsidence (negative UD values). The PPP solutions are referred to a local reference frame realized by five local CORS GPS Stations (Fig. 3.3). No outliers have been removed.

3.3 REFERENCE FRAMES

All positions, by definition, must be presented relative to an established reference point or frame (Bawden, et al., 2012). Reference frames may be celestial, global, regional, national, or local (Matsuzaka, 2012). This study's emphasis is on transforming the position data from a global reference frame to a regional and a local reference frame.

<u>IGS08</u>

Processing GPS data with GIPSY-OASIS generates solutions georeferenced to the Earth-Centered-Earth Fixed-International GNSS Service Reference Frame. The global reference frame that defines the satellite orbits is currently the International GNSS Reference Frame of 2008 (IGS08). The solutions achievable with modern GPS analyses are highly accurate and reliable, largely due to the precise software products provided by the International GNSS Service (Soler and Snay, 2004). The IGS began formatting its precision products within the International Terrestrial Reference Frame (ITRF) in 1994 (Kouba and Springer, 2001). In 2011, the IGS adopted the IGS08 reference frame, which replaces the previous IGS05 and is based on the current ITRF08 Frame. Currently, all IGS products are referred to this IGS 08 reference frame.

<u>NAD83</u>

Localization in GPS studies has resulted in an increase in the creation of local and regional reference frames, i.e. the North American Datum of 1983 (NAD 83), the South American Geocentric Reference System (SIRGAS) (Soler and Snay, 2004; Soler and

Marshall, 2003). This can be attributed to the fact that researchers working in these areas want to define intra-regional processes rather than global-scale processes. The implementation of a regional reference frame greatly improves the utility and comprehension of GPS-derived positions (Wang et al., 2013b). For the purpose of this study, it is inconvenient to study long-term landslide movements within the NAD 83 reference frame because everything moves within the NAD 83 reference frame. Instead a smaller local reference frame is needed for conducting precise local ground deformation using GPS (Wang et al. 2013b).

<u>LOCAL</u>

In order to know what and how something is moving, it is important to know what is "fixed" having near zero motion. The main physical and mathematical properties of a reference frame are the origin, the scale, the orientation, and the change of these parameters over time. A local reference frame is often realized by a reference frame transformation from a global reference frame. This process depends on first establishing a local reference frame made up of stable reference GPS stations and then performing a transformation.

Establishing a local reference frame requires three or more common points (reference stations) in order to tie the two reference frames (Wang et al., 2013; Wang et al. 2013b; Wang et al. 2014). A locally stable site would keep zero or "near-zero" three-component velocities within a "stable" reference frame. This principal is used to assess the stability (or accuracy) of local reference frames in this study. In practice, at least three reference stations are used to obtain greater accuracy for transformation parameters with the least squares iteration routine. More reference stations often result in better transformation parameters (Snay 1999; Soler and Snay 2004; Pearson et al. 2010); however, a reference station that is not locally stable will degrade the accuracy of the reference frame. Thus, the selection of reference stations is critical for establishing a stable local reference frame for precise landslide study. While, it is always a challenge to establish a stable local reference frame in remote and tectonically active regions, there are numerous permanent GPS stations in southern Alaska; most of which were installed by the PBO project. However, there are significant spatially and temporally complex patterns of "intra-plate" crustal deformation associated with post-seismic deformation, spatial variations in plate coupling, irregular translation and rotation of large crustal blocks in Alaska (Freymueller et al. 2008). As a result, it can be challenging to find a local-scale rigid block (i.e., 100 km by 100 km) for establishing a "stable" reference frame. An unstable reference frame could degrade the accuracy of landslide movements and thus over- or underestimate the risk of a landslide hazard (Wang et al. 2014). Hence, assessing the stability of a local reference frame is critical for precise landslide studies.

The Alaska landslide is located in a tectonic block between the central Denali fault and the Castle Mountain fault (Fig.1.2). There are no identified active faults between these two major faults. There are several long-term (> 5 years) continuously operating reference GPS stations (CORS) close to the landslide site, which can be used to realize a local reference frame for delineating local ground motions. Figure 3.3 illustrates velocity vectors within three local reference frames realized by different reference station configurations. Yellow dots represent reference stations used for realizing each local reference frame. The first reference frame (fig. 3.3a) was realized using five local reference stations (AB28, AC51, AC46, AC33, TLKA) surrounding the landslide. The network of these five references covers an area of about 100 km by 150 km. Three reference stations (AC51, AC46, AC33) shows zero or near-zero velocities (< 0.5 mm/year) within the local reference frame, but two reference stations (AB28 and TLKA) show 2 to 3 mm/year horizontal velocities. The average horizontal velocity of these five reference stations within the local reference frame is 1.6 mm/year. Accordingly, a "stable" site within the reference frame could have a minor velocity. Thus, this reference frame is not a strictly "stable" local reference frame. The second reference frame (Fig. 3.3b) was realized by three reference stations (AB28, AC51, AC46) located southwest of the landslide site. All three reference stations show near-zero velocities (< 0.5 mm/year) within the reference frame, which seems to be a "stable" reference frame. However, the landslide site is located outside of the area surrounded by the three reference stations. The distance between the landslide and the nearest reference station (AC46) is 46 km. AC33 is about 88 km away from the nearest reference station (AC46), which shows a 2.6 mm/year velocity referred to the second reference frame. Assuming a simple linear regression of ground deformation, a 1.5 mm/year velocity would be expected at the landslide site referred to the second reference frame. The third local reference frame (Fig. 3.3c) was realized by three stations (AB28, AC46, AC33) surrounding the landslide site. Two reference stations (AC46, AC33) show near zero velocities (< 0.5 mm/year), whereas one (AB28) shows about 2.5 mm/year of horizontal velocity. The average horizontal velocity of these three reference stations is 1.2 mm/year within the local reference frame. The reference frame calculated from five reference stations (Fig. 3.3a) is preferred due to the spatial geometry of the stations relative to AC55. This is not a strictly "stable" local reference frame because the uncertainty of velocities at sites within the reference frame is about $\pm$ 1.5 mm/year. The high uncertainty is a result of the undergoing tectonic deformation within the crustal block. Comparatively, the Stable Houston Reference Frame is a more rigid body and has an accuracy of $\pm$ 0.5 mm/year.

This study uses a 14-parameter Helmert transformation to realize local movement (Soler and Snay, 2004; Dawson and Woods, 2010; Pearson, et al., 2010; Wang et al., 2013b; Wang et al. 2014). The transformation was applied to convert positional coordinates from IGS08 to the local reference frame following the methodology of Wang et al. (2013b). The following equations were used in the realization of the Local Reference Frame (LRF) and are defined as functions of time. This time-dependency allows the transformation process to accommodate any change in position through time using the following transformation equation.

Local Reference Frame (LRF) Transformation Equations:

$$X(t)_{LRF} = T_X(t) + [1+s(t)] \cdot X(t)_{igs08} + R_z(t) \cdot Y(t)_{igs08} - R_Y(t) \cdot Z(t)_{igs08}$$

$$Y(t)_{LRF} = T_Y(t) - R_Z(t) \cdot X(t)_{igs08} + [1+s(t)] \cdot Y(t)_{igs08} + R_X(t) \cdot Z(t)_{igs08}$$

$$Z(t)_{LRF} = T_Z(t) + R_Y(t) \cdot X(t)_{igs08} - R_X(t) \cdot Y(t)_{igs08} + [1+s(t)] \cdot Z(t)_{igs08}$$

From the equations, *X(t)IGS08, Y(t)IGS08,* and *Z(t)IGS08* represent the X,Y, and Z position of the GPS station at time *t*, calculated by the GIPSY-OASIS software package (which is referenced within the IGS08 global reference frame). Comparatively, *X(t)LRF, Y(t)LRF,* and *Z(t)LRF* are representative of the X,Y, and Z position of the ground station within the stable Local Reference Frame, at time *t*. The equations shown demonstrate that the X, Y, and Z coordinates in the IGS08 reference frame are transformed into the LRF through the following processes: (a) A translation along the respective axis (in meters). This is represented by the *Tx(t), TY(t),* and *TZ(t)* terms; (b) Differential scaling of the respective axis. This is represented by the *s(t)* term; and (c) Counter-clockwise rotations (in radians) around the remaining two axis, represented by the *Rx(t), RY(t),* and *RZ(t)* terms (Wang et al. 2013).

Three component time series (Appendix B) were plotted for 20 GPS stations in the study and then displacement values (Appendix C) were used to create velocity vector maps. Displacement vector maps allow for easy comparison of the surface motion at varying reference frames (Fig. 3.4a-c). To evaluate GPS motion during the observed landslide, the velocity vectors were recalculated for the 2006-2010 period (Fig. 3.5). Figure 3.6 is an enlarged view of the velocity vectors (>1mm/year) during the landslide period in the Local Reference Frame. This map focuses attentions to anomalous independent surface motion. The post-seismic motion is bundled into the common seasonal ground motion model. Only one of the GPS stations in the study area was in operation prior to the 2002 Denali Earthquake, TLKA. The three component displacement time series for TLKA in the LRF with co-seismic and post-seismic deformation (Fig. 3.7).

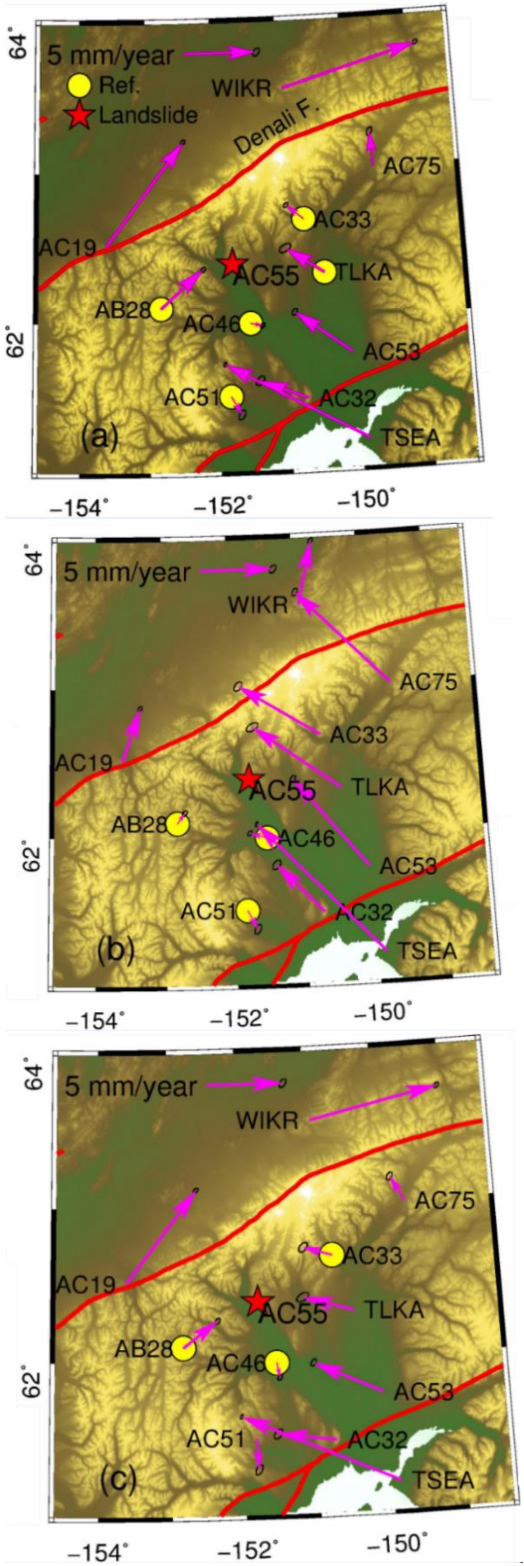

Figure 3.3: Local Reference Frame. Velocity vectors at GPS stations surrounding the landslide (AC55) referred to three local reference frames. Yellow dots represent local reference stations used to realize the local reference frame; (a) top, (b) middle, and (c) bottom. The northern and southern faults are the central Denali Fault and the Castle Mountain Fault, respectively.

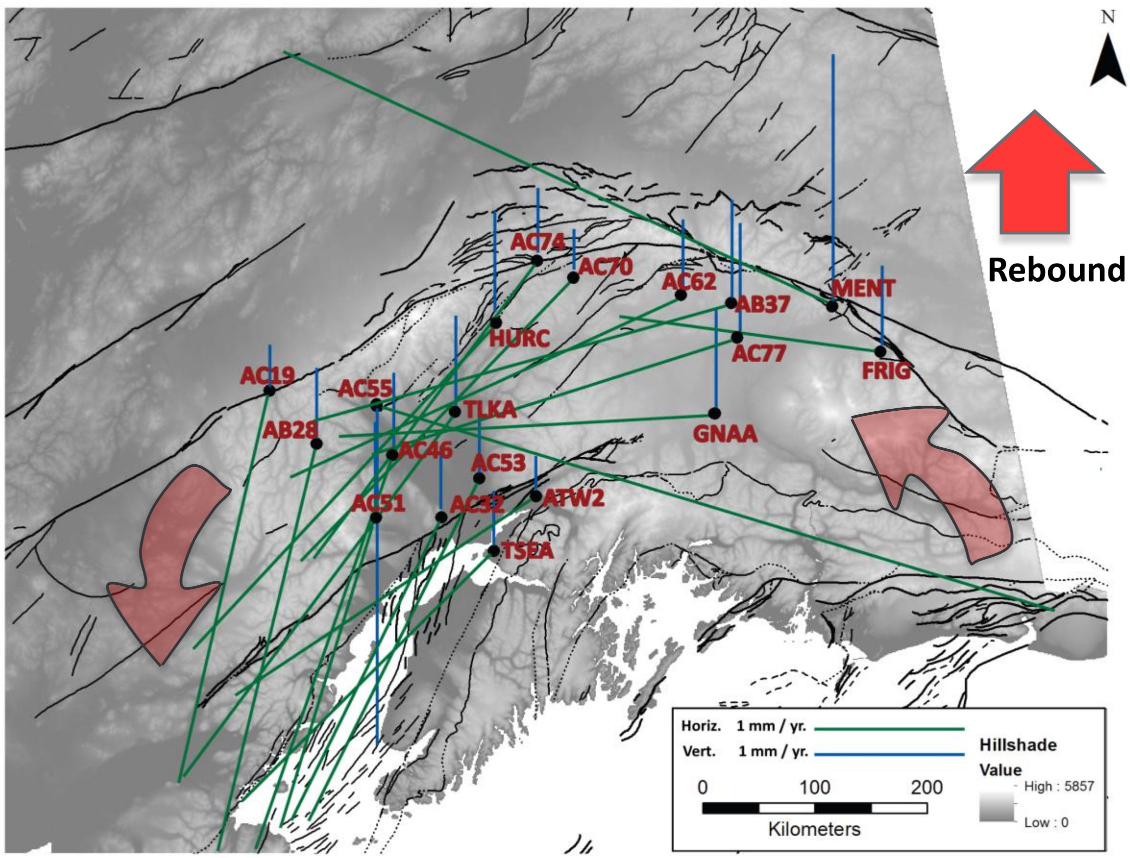

Figure 3.4a: Long term velocity vectors in the IGS08 Reference Frame. Reflects the entire GPS data covering the life span of all the stations. Black vector lines represent horizontal motion while blue vector lines represent vertical motion. Red arrows reflect the motion of the Wrangell block that overshadows horizontal motion. The dominate vertical motion (except for AC55) is responding to isostatic rebound.

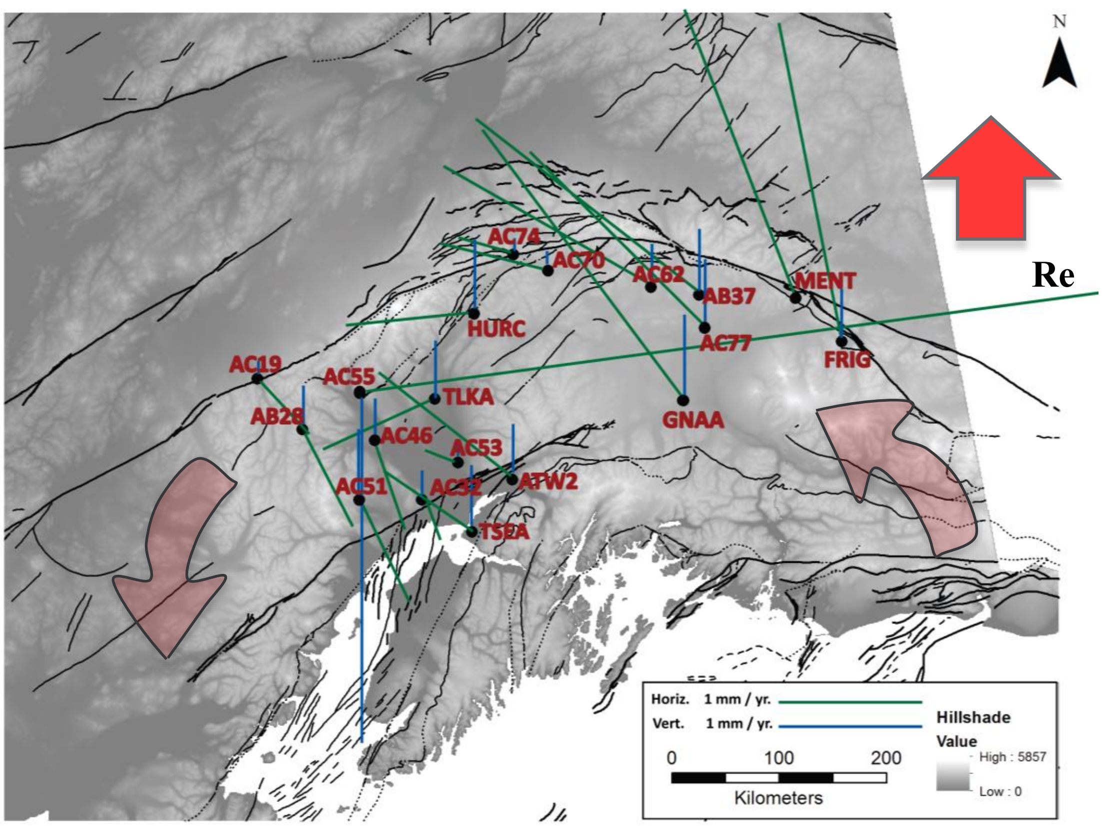

Figure 3.4b: Long term velocity vectors in the NAD83 Reference Frame. Reflects the entire GPS data covering the life span of all the stations. Black vector lines represent horizontal motion while blue vector lines represent vertical motion. Red arrows reflect the motion of the Wrangell block that influences horizontal motion. The dominate vertical motion (except for AC55) is responding to isostatic rebound.

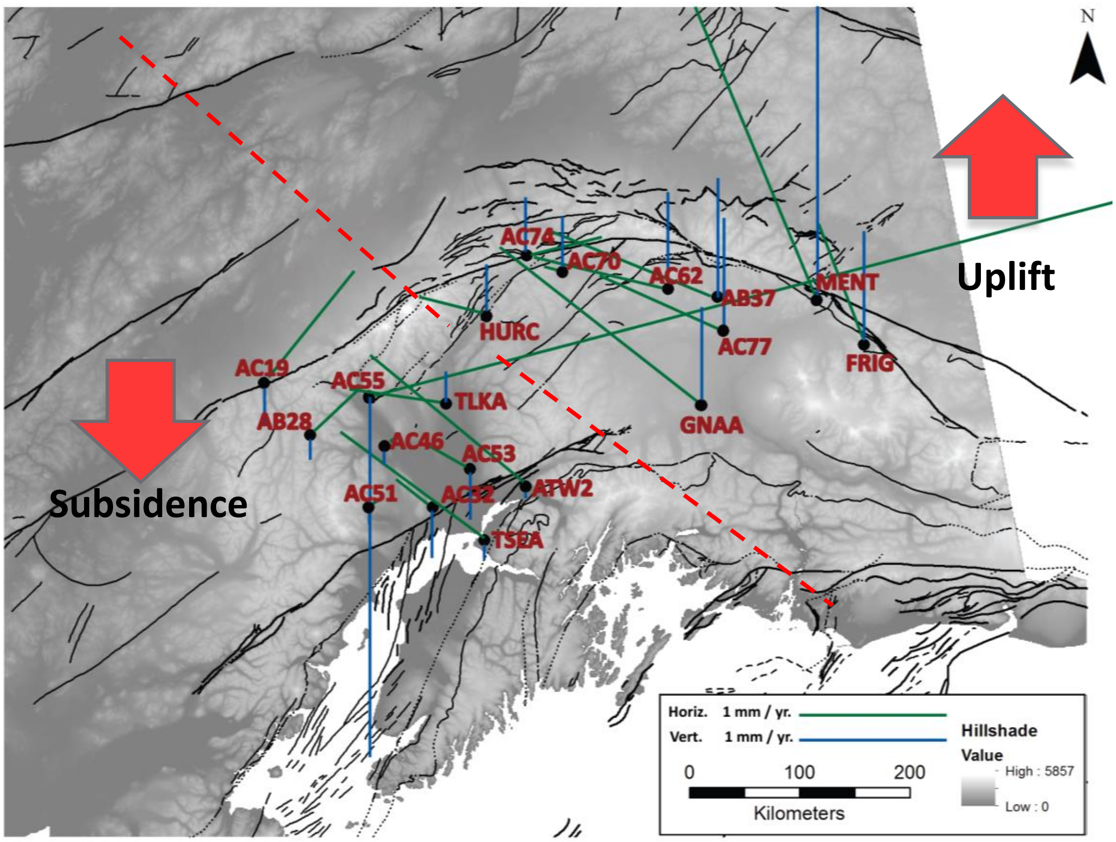

Figure 3.4c: Long term velocity vectors in the Local Reference Frame. Reflects the entire GPS data covering the life span of all the stations. Real GPS motion is realized in the Local Reference Frame. Black vector lines represent horizontal motion while blue vector lines represent vertical motion.

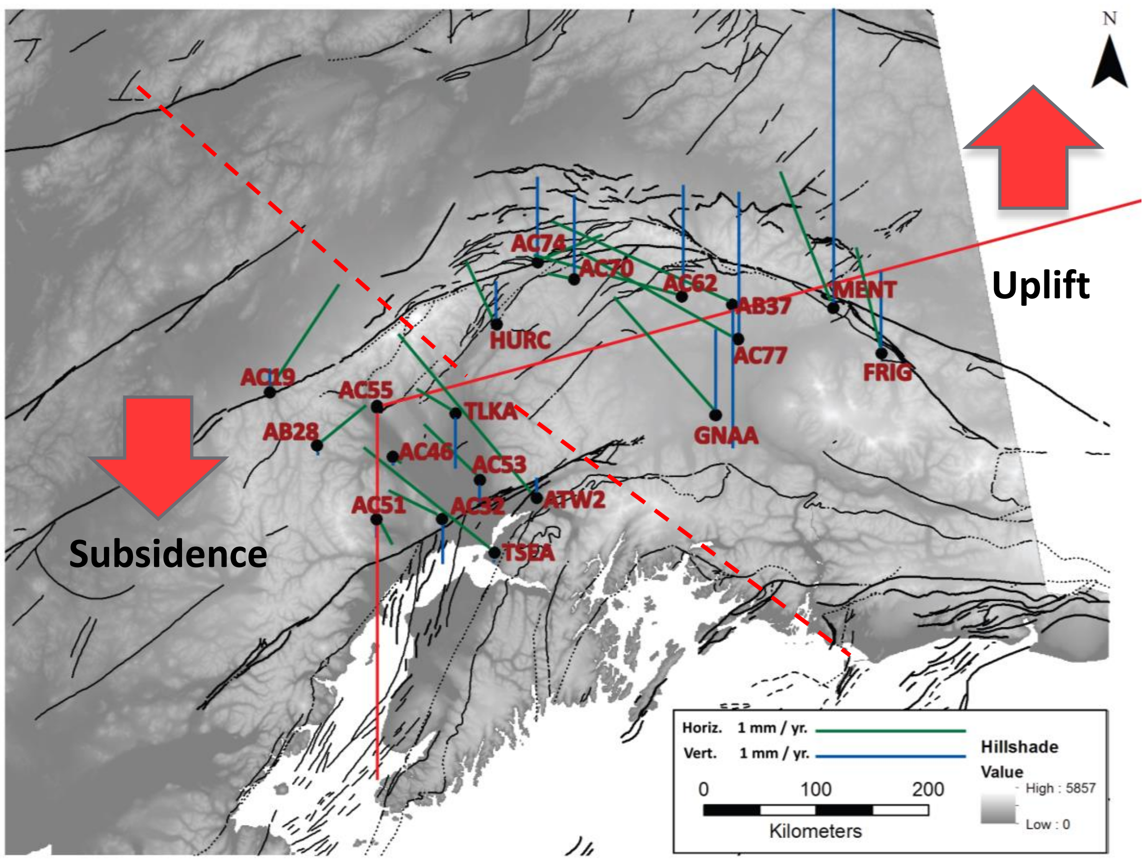

Figure 3.5: Short Term velocity vectors in the Local Reference Frame. Reflects GPS data covering 2006-2010 of all the stations. Corresponds to the operation of AC55 landslide observation. Black vector lines represent horizontal motion while blue vector lines represent vertical motion.

.

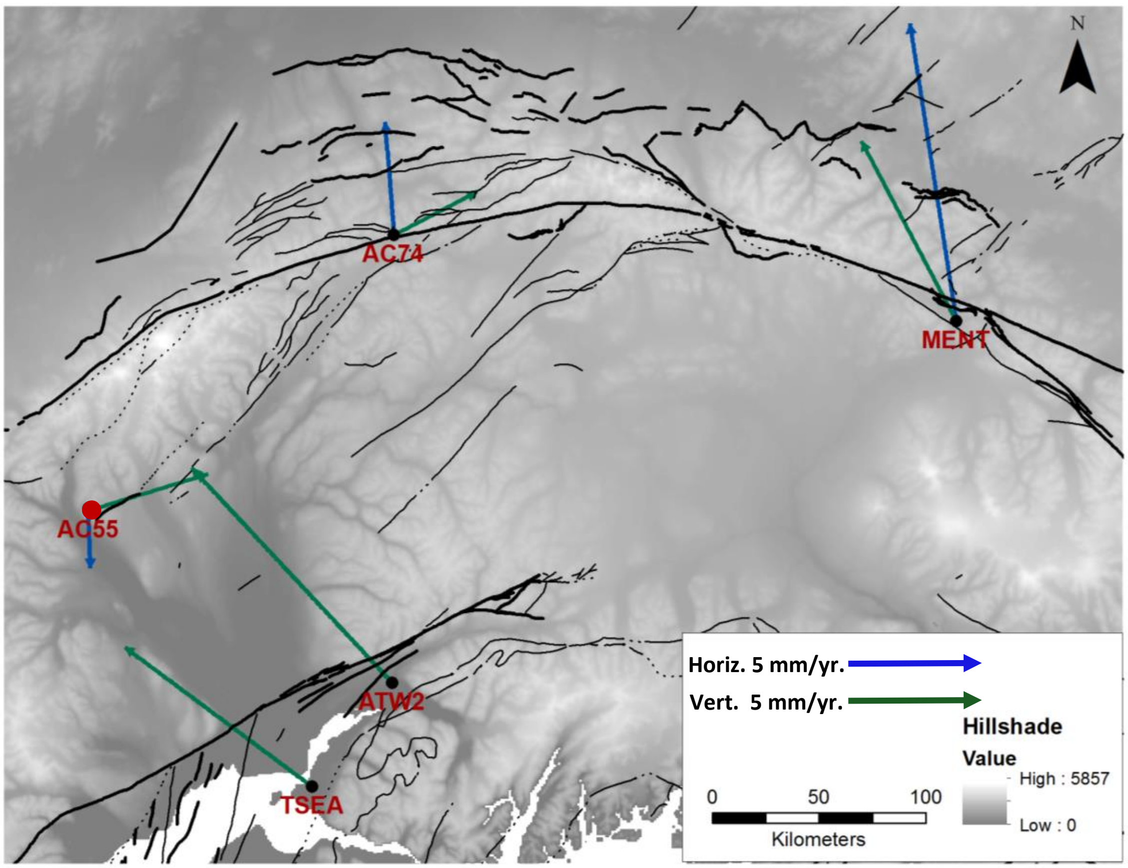

Figure 3.6: Enlarged view of velocity vectors (> 1mm/yr.) during the recorded landslide period (2006-2010) for Local Reference Frame. Blue vectors represent horizontal motion while green vectors represent vertical motion. Ignoring the velocities of ATW2 and TSEA located to the south of the long lateral Castle Mountain- Lake Clark fault, the central fault block is relatively stable with minimal motions. The only exceptions to this are those located along the Denali fault and the landslide at AC55. Red dot represents AC55, which has a large eastward component.

Displacement at TLKA Referred to Local Reference

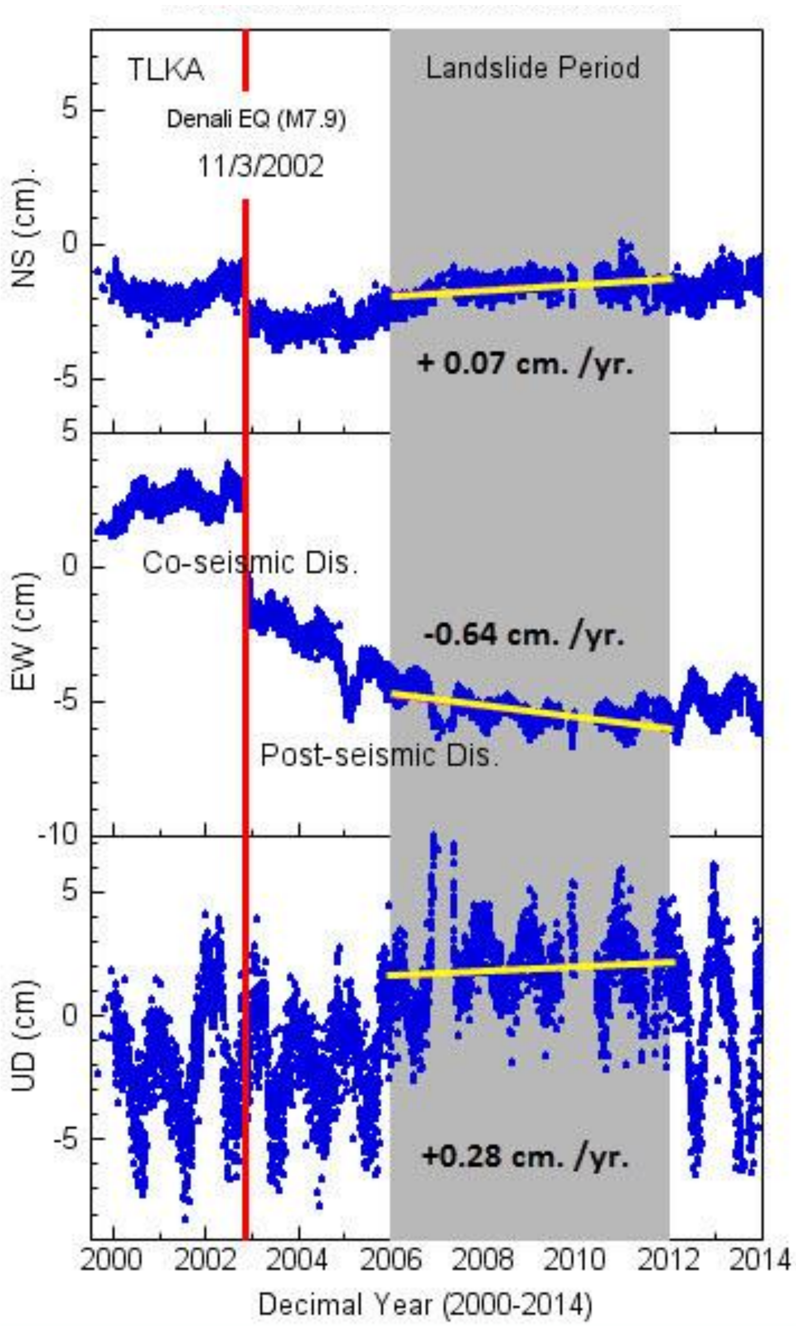

Figure 3.7: Three-component long-term displacement time series recorded at permanent GPS station TLKA. The GPS-derived positions are referred to a local reference frame realized by five local reference stations (Figure 3.2a). Only a segment of the positions time series from 2006 to 2011 was applied in realizing the local reference frame and plotting local velocity vectors in this study. The surface motion trend is to the North (positive NS values), West (negative EW values) and a slight vertical rebound (positive UD values).The plots show significant co-seismic displacements and long-term post-seismic deformations. The vertical line shows the time of the 2002 Denali fault earthquake (M7.9, November 3, 2002).

3.4 SEASONAL VARIABILITY

The vertical component of the GPS time series has a seasonal height variation (the red sinusoid curve in Fig. 3.9; Fig. 3.10), which in this region reflects a change in snow accumulation (Fig. 3.8) and meltwater discharge. Several previous investigations have pointed out that GPS-derived positions in cold regions can be contaminated by snow and ice accumulating on GPS antennas during cold seasons (Webb et al. 1995; Jaldehag et al. 1996; Lisowski et al. 2008; Larson 2013; Wang et al., 2015). The winter season in central Alaska essentially lasts from October through March. Snow and ice can delay, attenuate, and scatter received GPS signals and thus affect the GPS observations (Fig. 3.8). As a result, the GPS-derived positions on these days could be biased, and often appear as outliers in positional time series (Fig. 3.9). These positioning outliers are typically removed by assuming a linear ground motion trend in plate tectonic studies. This is an effective way to get a “clean” positional time series for calculating linear velocity vectors for plate tectonics study; however, landslide movements are often nonlinear. Heavy rainfall, earthquake, snow loading, and other external forces can temporally accelerate landslide movements. Local groundwater level changes can also affect landslide movements. For a long-term landslide monitoring project, snow and ice biased positions could be mixed with seasonal movements of the landslides induced by annual snow loading and melting cycles; moreover the biased positions could easily be misinterpreted as signals of rapid sliding events. Therefore the GPS antennas with snow and ice accumulation must be identified and biased daily signals need to be filtered to remove false motion.

Seasonal variations are often observed in GPS-derived positional time series. Earlier studies relate this observation to seasonal phenomena, such as variations in the groundwater table (Watson et al., 2002), surface water load (Dong et al., 1997; van Dam et al., 2001; Bevis et al., 2005), snow loading (Heki, 2001), soil moisture (Blewitt et al., 2001), bedrock thermal expansion (Dong et al., 2002), and errors related to satellite orbits, reference frames, and software packages. Southern Alaska has a long winter season for snow and ice accumulation (Fig. 3.8) and a relatively warm summer season for melting. Thus snow loading and melting can cause substantial variations in positional time series (Geirsson et al., 2006). Indeed, significant seasonal ground deformation associated with snow loading and melting, particularly in the vertical direction, had been observed from GPS-derived positional time series in Alaska (Freymueller, 2009). These variations are often annual in period. In order to recover real landslide movements, the local or regional seasonal ground motions need to be excluded from GPS-derived landslide displacement time series.

One complication is that there is considerable correlation between annual snow loading and melting cycles and seasonal variations of the landslide displacements. The seasonal movements vary year to year with average peak-to-peak amplitude of 1.5 cm and 1.0 cm in vertical and horizontal directions, respectively.

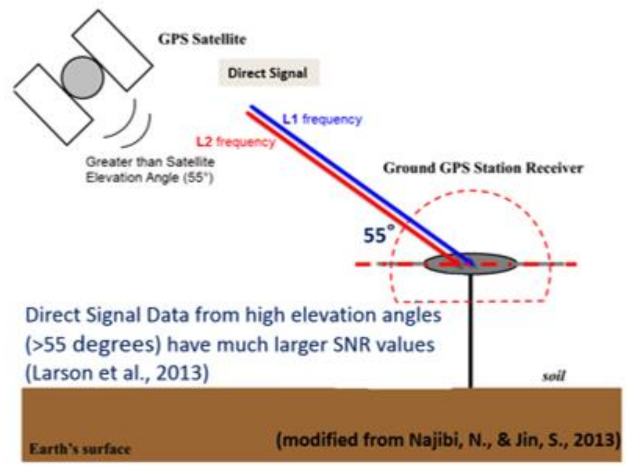

(a)

(c)

(Wang et al., 2015)

Figure 3.8: (a-b) GPS Signal contamination from snow/ice. GPS-derived positions can be contaminated by snow and ice accumulating on GPS antennas (Larson 2013). Snow and ice can delay, attenuate, and scatter GPS signal adding to errors. GPS-derived positions on snow and ice days are biased and appear as outliers in the time series plots (Fig. 3.9). (c-d) AC33 was in the study area but was not used due to the sever snow and ice contamination.

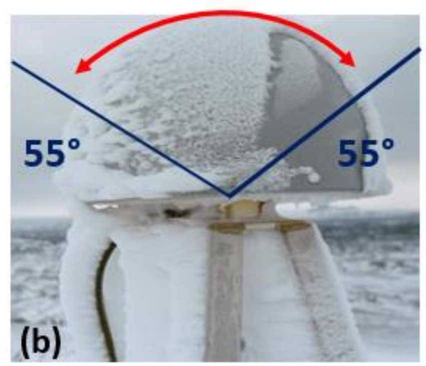

(b)

http://hraun.vedur.is/ja/englishweb/gps/skro.html

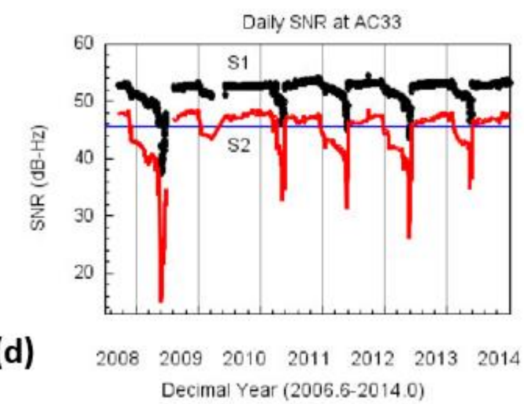

(d)

(Wang et al., 2015)

The GPS stations investigated in this study operate Trimble NetRS dual-frequency GPS receivers with Trimble choke ring antennas. The choke ring antenna is covered by an acrylic radome, whose main purpose is to reduce the buildup of snow and ice (Fig. 3.8). The Trimble NetRS GPS receivers also commonly record the strength of the received satellite signals, which is also described as the signal-to-noise-ratio (SNR). The SNR data can be output to the standard Receiver Independent Exchange (RINEX) file (Gurtner 1994). The raw GPS data used in this study are recorded at a rate of one observation every 15 seconds. In a typical RINEX file of PBO stations archived at UNAVCO, the GPS observations contain “L1” and “L2” carrier phase data. “S1” and “S2” are signal-to-noise-ratios (SNR) in unit of “dB-Hz” (Larson 2013). These SNR data indicate signal power relative to a receiver-calculated noise level. Snow and ice accumulated on GPS antenna would mainly affect high elevation satellite signals. In general, the travel time of satellite signals would be delayed, and the strength of the satellite signals received by the antenna would be degraded because of the attenuation of GPS signals when travelling through snow and ice. Thus, the SNR data can be used as an index to determine the validity of the GPS-derived positions (Wang et al., 2015).

This study implemented an algorithm using daily SNR data to detect GPS positions impacted by snow and ice on antennas, which was proposed originally by Larson (2013). Snow and ice mostly accumulate on top of the antenna radomes, thus the snow and ice will have minor effects on signals from low-elevation satellites. In this study, daily SNR is defined as the averaged SNR values (“S1” or “S2”) of all received satellite signals with elevation above 55 degrees during a 24-hour time window. The daily-SNR can be calculated through the following mathematical formula:

$$\mathrm{SNR_{Daily}} = \frac{1}{N}\sum_{i=1}^{N}\left(\frac{1}{M}\left(\sum_{j=1}^{M} S(j)\right)\right) \qquad \text{(Eqn. 1)}$$

Where N is the total number of epochs within a 24-hour observation period. For a 15-second sampled GPS observation daily RINEX file, N is 5760 or less if there are gaps in observations. M is the number of total visible GPS satellites with an elevation degree larger than 55 degrees at each epoch. M varies from 3 to 7 in the landslide area depending on the time of day.

Figure 3.9 and Figure 3.10 illustrates the daily SNR (“S1” and “S2”) time series derived from four-year continuous GPS data at the landslide (AC55) site. The daily SNR time series of AC55 show fairly consistent annual harmonic behavior from year to year. Annual variations of S1 and S2 were 0.5 dB-Hz and 1 dB-Hz, respectively. There are consistent lower values in the summer and higher values in the winter. The periodic change of daily SNR value is largely driven by seasonal variations of temperature. In general, GPS receivers and antennas have lower noise levels in lower temperature environments, and thus, the SNR values recorded by the receivers will be higher in winter and lower in summer (Misra and Enge, 2006; Larson, 2013). AC55 was installed at a higher position close to the edge of a hill (Fig. 3.11). Thus, snow on the antenna could be easily blown away by wind.

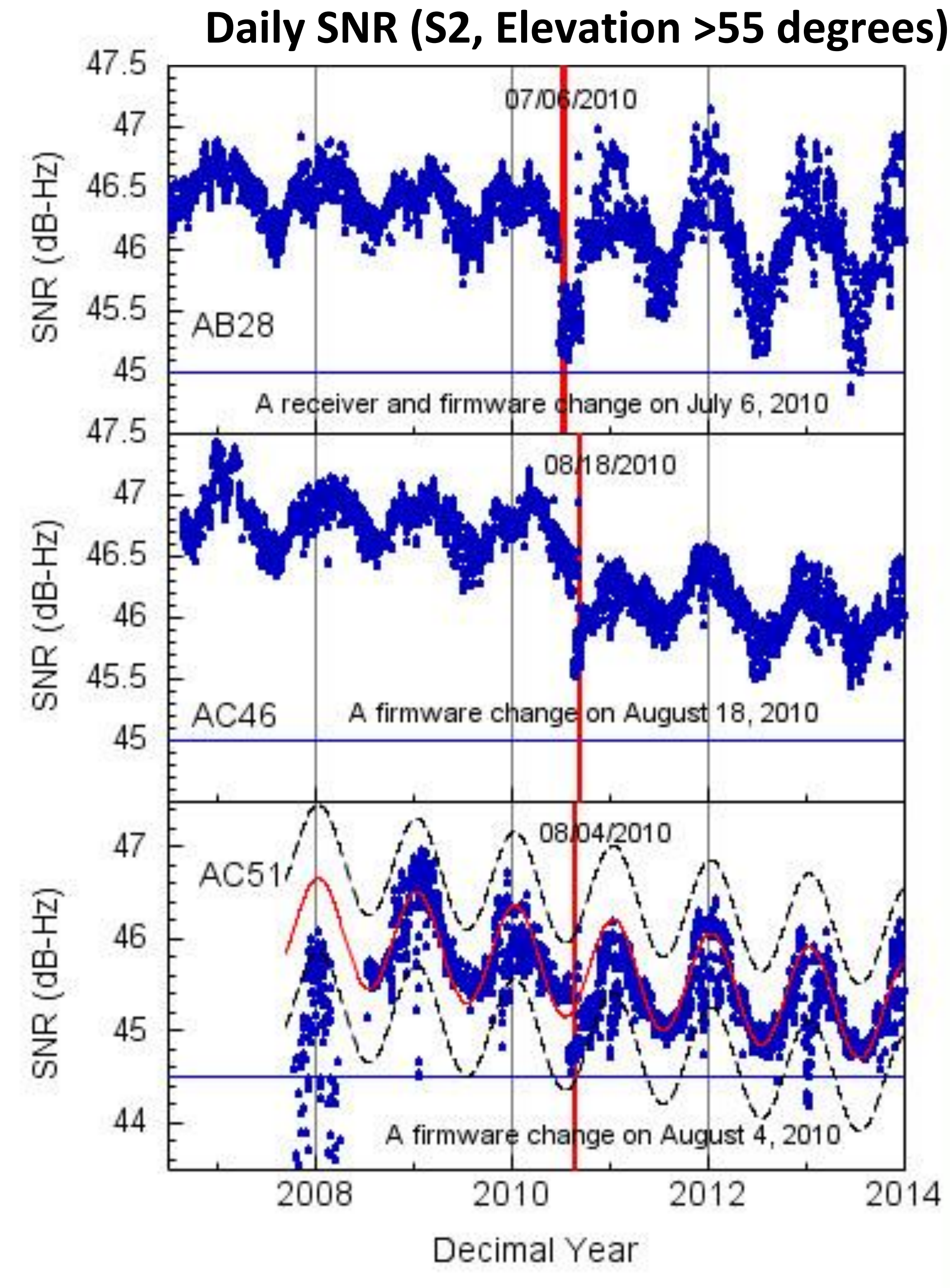

Figure 3.9: Daily signal-noise-ratio (SNR: S2) time series derived from GPS observations at AB28, AC46, and AC51. The GPS receivers are Trimble NetRS receivers. There was a firmware change from 1.1-2 to 1.3-0 on July 6, August 18, and August 4, 2010 at AB28, AC46, and AC51, respectively. The sinusoid (red) is the modeled SNR with Eqn. (3) using least square fit polynomial regression. The black dashed lines represent two times the standard deviations (±2σ). Biased data are outliers outside the dashed lines (in black).

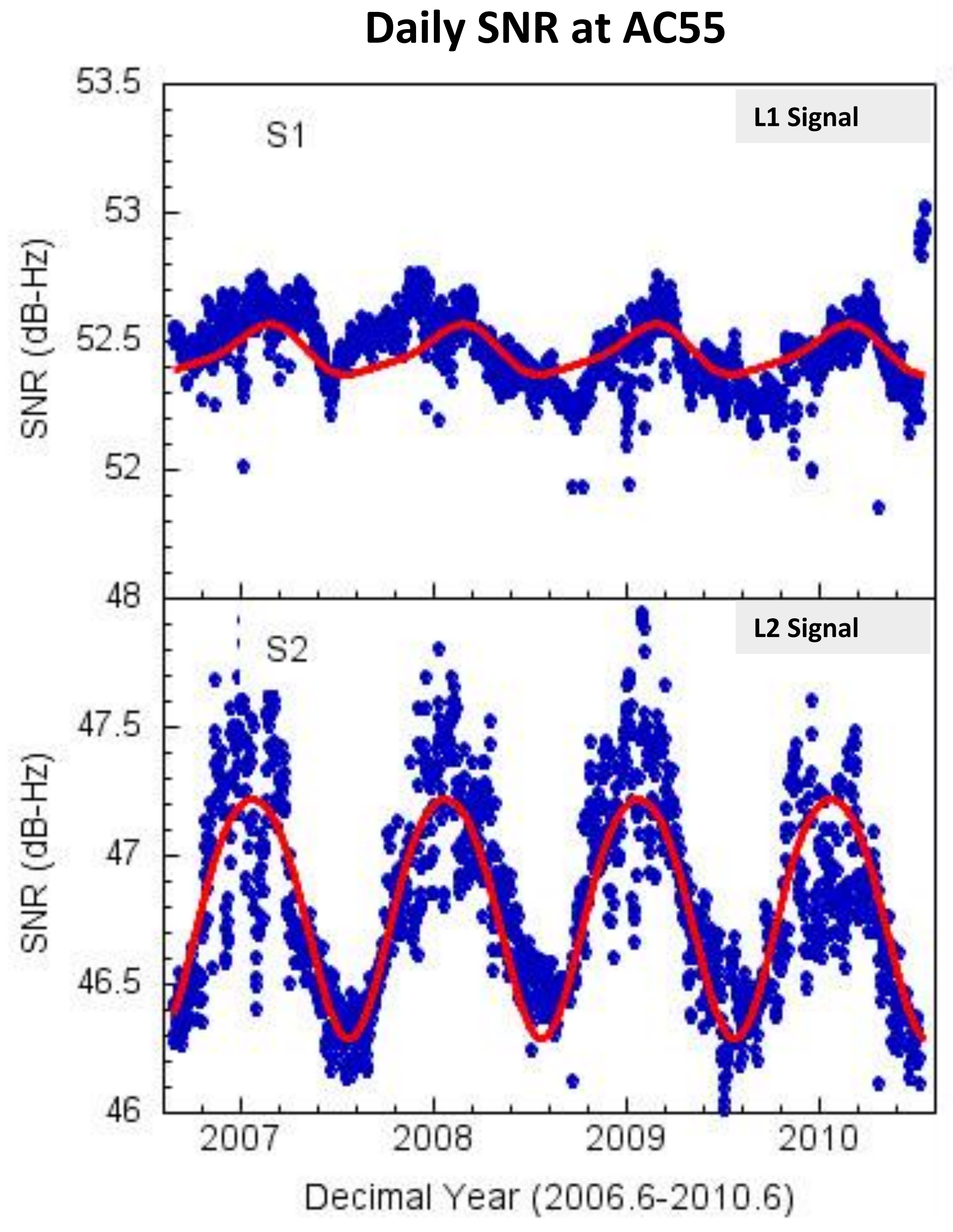

Figure 3.10: Daily Signal-Noise-Ratio (SNR: S1, S2) time series derived from GPS observations at the landslide GPS station AC55. Daily SNR is calculated with Eq**n**. (1). The sinusoid (red) is the modeled SNR with Eq**n**. (3). S1 and S2 from satellites with elevation degrees larger than 55 degrees are used in calculating the daily SNR.

The clean and consistent annual harmonics of SNR time series of AC55 (Fig. 3.9; Fig. 3.10) also suggest that this GPS antenna was not considerably affected by snow and ice. The signal also suggests that the SNR data (S2) from the satellite signal L2 are more sensitive to temperature change than the SNR data (S1) from the satellite signal L1 (Fig. 3.9; Fig. 3.10). The periodic daily SNR time series can be represented approximately by a combination of linear attenuation and harmonic cycles, which can be modeled with the following formula (Wang et al., 2015).:

$$\mathrm{SNR}(t_i) = a + bt_i + \sum_{j=1}^{k}(c_j \sin(2\pi j t_i) + d_j \cos(2\pi j t_i)) \quad \text{(Eqn. 2)}$$

Where $t_i t_i$ for i=1, 2,…, N are epochs in a unit of year. Coefficients aa and bb describe the linear changes of daily SNR, which can be obtained by a linear regression of the daily SNR time series. Coefficients $c_j c_j$ and $d_j d_j$ can be obtained by a Fourier analysis method. The coefficient kk is the number of cyclical sinusoids within the observed SNR time series. The combination of an annual sinusoid and a half-annual sinusoid fit the observed harmonics within the SNR time series very well. As a result, Equation 2 can be simplified to the following (Wang et al., 2015):

$$\mathrm{SNR}(t_i) = a + bt_i + c_1 \sin(2\pi t_i) + d_1 \cos(2\pi t_i) + c_2 \sin(4\pi t_i) + d_2 \cos(4\pi t_i)\mathrm{SNR}(t_i) = a + bt_i + c_1 \sin(2\pi t_i) + d_1 \cos(2\pi t_i) + c_2 \sin(4\pi t_i) + d_2 \cos(4\pi t_i) \quad \text{(Eqn. 3)}$$

Equation 3 is a mathematical model consisting of an annual seasonal term and a linear attenuation term defined by the model and threshold ($\mathrm{model} \pm k\sigma \mathrm{model} \pm k\sigma$). The process to detect and remove SNR outliers uses two times the standard deviations (±2σ) of the residuals between observed and modeled SNR values, which produces a seasonal dependence of SNR with temperature (Fig. 3.9; Fig. 3.10). Biased positions must be removed from the continuous landslide displacement time series as outliers. The advantage of the method described here is that no assumption of true geophysical behavior of the Earth surface is needed. This method can be applied to any cold area without consideration of site differences, such as sites located in plate interiors, near volcanoes, near plate boundaries, or on moving ice sheets. As an external validation of the mathematical model based on the GPS data, seasonal variability derived from GRACE observations is evaluated in a subsequent chapter.

3.5 GPS STATION AC55 AND THE YENTNA LANDSLIDE

GPS station AC55 was operated for four years (September 2006-July 2010) before being decommissioned (Table 2). The PBO GPS stations were supposed to be rooted on the tectonic plates that they monitored, but AC55 was installed on a creeping landslide on the east bank of the Yentna River in South Central Alaska (Fig. 3.11). The landslide site is located about 160 km north of Anchorage and 340 km southwest of Fairbanks (Fig. 1.2). The slip rate of the central segment of the Denali fault closest to the landslide area is about 10 mm/year (Freymueller et al., 2008). The distance between the landslide location and the earthquake epicenter is about 300 km.

Landslides are a significant natural hazard in mountainous regions and often triggered by external factors such as earthquakes, rainfall, permafrost thawing, and retreat of glaciers. A slow creeping landslide is characterized by the imperceptibly slow, steady, downward movement of slope-forming soil or rock where the rate of movement can be as slow as 10mm/year (USGS, 2004). Movement is caused by shear stress sufficient to produce permanent deformation, but too small to produce shear failure (USGS, 2004). There are generally three types of creep: (1) seasonal, where movement is within the depth of soil affected by seasonal changes in soil moisture and soil temperature; (2) continuous, where shear stress continuously exceeds the strength of the material; and (3) gradual progressive deformation where slope reaches the point of failure (USGS, 2004). Without conducting field measurements it would be impossible to classify the type and mechanisms of creep at AC55. The accepted contributing elements are: 70 inches of precipitation (Brabets et al., 1999) mostly in the form of snow/ice, 5-50 m deep of discontinuous permafrost (Jorgenson et al., 2001; Eberhart-Phillips et al., 2003), and a subzero mean annual air temperature of 0° to -5°C (Jorgenson et al., 2001). In addition, the slow landslide creeping could be biased by post-seismic deformation, translation and rotation of large crustal blocks or plates.

Table 3.1. Yentna_RvrAK2006 (AC55) PBO Site Details (PBO, 2014)

IGS08 Reference Frame (Ref Epoch: 2010.548)	
ECEF (m/m/m)	WGS 1984 (d/d/m)
X = -2611995.3956	Latitude: 62.384443943
Y = -1402618.8869	Longitude: -151.764587011
Z = 5629399.9854	Elevation: 1012.2720

Site Identification GNSS Monument	
Site Name	Yentna_RvrAK2006
Four Char ID	AC55
Date Installed	2006-08-25T00:00Z
Date Removed	2010-07-10T17:48Z

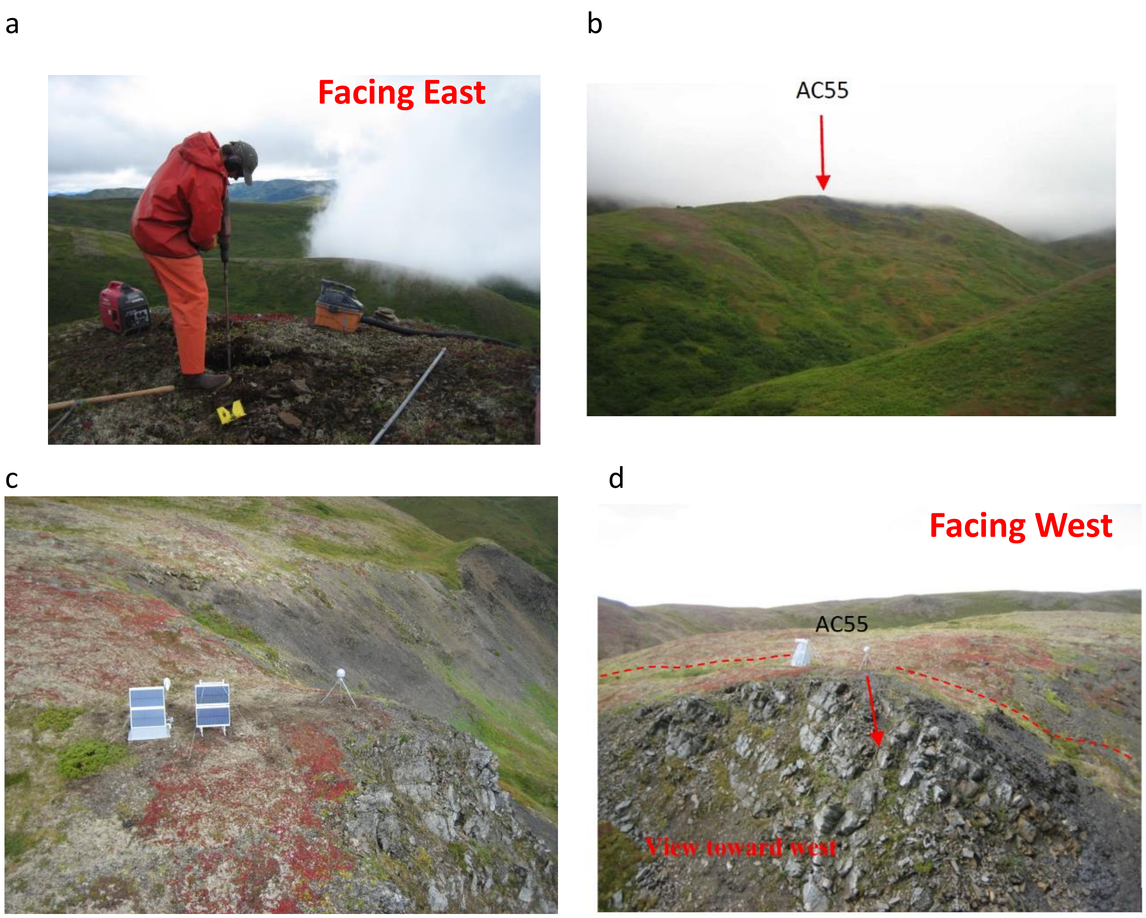

Figure 3.11: AC55 Installation Site. (A-D) Photos showing site views at the landslide site. AC55 was a permanent GPS station operated by the EarthScope PBO project, which was in operation from September 2006 to July 2010. (C) Soil ripples that are creep indicator can be seen. (D) The landslide displacement vector is estimated according to the calculated results. The red dashed line behind the GPS station illustrates the potential landslide boundary, where a heavy vegetation lineament can be seen. (Photos are provided by Mr. Chris Walls of UNAVCO).

For landslide studies, GPS data from one ground station are not sufficient alone to precisely measure “real” landslide movements. For preliminary evaluations, landslide displacement can be modeled from the GPS data by removing the modeled local seasonal motions (red line on Fig. 3.12a). This seasonal motion was calculated from the displayed three-component positional time series of three reference sites (AC51, AC46, and AB28) referring to the first local reference frame (Fig. 3.3a). It appears that the annual seasonal motions in the vertical component are particularly significant with peak-to-peak amplitudes of about 1.5 cm. The seasonal positional variation involves subsidence in winter and uplift in summer. For the central Alaska region, the snowpack accumulation often starts around the last week of September with most sites receiving a few centimeters of snow; after this week snow generally accumulates on the ground for the rest of the season. The annual snowpack in central Alaska typically reaches its maximum values at the end of March. Snow-off dates for the landslide area are normally in early May (Sousanes, 2012). Corresponding to the seasonal change of snow, local ground begins to subside in September, roughly coinciding with the beginning of substantial winter snow accumulation, and begins to uplift in April, roughly coinciding with the beginning of significant runoff from spring melt. Interannual variations are also visible in horizontal components. In fact, numerous continuous GPS sites in Alaska show a similar pattern of seasonal ground motions, which is consistent with snow loading as the principal cause (Freymueller, 2009). Similar seasonal movements were observed in northern Japan (Heki, 2003), Iceland (Grapenthin et al., 2006), and Nepal (Fu and Freymueller, 2012). The average seasonal ground motions within the landslide region can be represented by stacking the positional time series of the three local stations (AC51, AC46, AB28). The seasonal signal in the stacked positional time series can also be modeled by annual cyclical sinusoids (Wang et al., 2015):

$$\mathrm{Dis}(\mathrm{t_i}) = \mathrm{a} + \mathrm{c_1}\sin(2\pi\mathrm{t_i}) + \mathrm{d_1}\cos(2\pi\mathrm{t_i}) + \mathrm{c_2}\sin(4\pi\mathrm{t_i}) + \mathrm{d_2}\cos(4\pi\mathrm{t_i}) \qquad \text{(Eqn. 4)}$$

where $\mathrm{t_i}\mathrm{t_i}$ represents epochs of observations with a unit of year. Coefficient $\mathrm{a}\mathrm{a}$ represents the average position, $\mathrm{c_1}\mathrm{c_1}$ and $\mathrm{d_1}\mathrm{d_1}$represent the amplitudes of the annual seasonal motions, and $\mathrm{c_2}\mathrm{c_2}$ and $\mathrm{d_2}\mathrm{d_2}$ represent the amplitudes of the half-annual seasonal motions. These coefficients can be obtained through Fourier analysis. Landslide motions could be obtained by removing the modeled local seasonal motions from GPS-derived displacement time series. The following specific parameters are used in modeling the local seasonal ground motions (Wang et al., 2015):

$$Dis_{NS}(t_i) = -0.077 + 0.155\sin(2\pi t_i) + 0.046\cos(2\pi t_i) + 0.071 sin(4\pi t_i) - 0.016 cos(4\pi t_i)$$

$$\mathrm{Dis_{EW}}(\mathrm{t_i}) = \text{-}0.011 + 0.022\sin(2\pi\mathrm{t_i}) + 0.086\cos(2\pi\mathrm{t_i}) + 0.021\sin(4\pi\mathrm{t_i})\text{-}0.021\cos(4\pi\mathrm{t_i})\mathrm{Dis_{EW}}(\mathrm{t_i}) = \text{-}0.011 + 0.022\sin(2\pi\mathrm{t_i}) + 0.086\cos(2\pi\mathrm{t_i}) + 0.021\sin(4\pi\mathrm{t_i})\text{-}0.021\cos(4\pi\mathrm{t_i})$$

$$Dis_{UD}(t_i) = 0.092 + 0.164\sin(2\pi t_i) - 0.582\cos(2\pi t_i) + 0.046 sin(4\pi t_i) - 0.014 cos(4\pi t_i) \qquad \text{(Eqn. 5)}$$

After calculating the seasonal signal (Fig. 3.12a), the detrended landslide displacement is derived (blue marks in Fig. 3.12b). It is evident that AC55 has a greater displacement that the other stations, particularly in the Northing and Easting components. Figure 3.12c examines AC55 independently. The three-component positions are the detrended landslide displacement time series after removing the modeled common local seasonal motions (Eqn. 5) therefore leaving only the seasonal motion independent to AC55. There are considerable periodical motions within the landslide displacement time series (red line), particularly in the EW direction with peak to peak amplitudes of 1.5 cm. Figure 3.12c shows similar annual patterns with the local seasonal ground motions (Fig. 3.12a), which suggests that snow loading and unloading (melting) may also dominant the seasonal landslide movements. This landslide may have been moving for a long period. A potential weak landslide boundary has been created perpendicular to the slide direction (red dashed line in Fig. 3.11d). In fact, a heavy vegetation lineament can be seen behind the GPS station (AC55) as shown in the site photo (Fig. 3.11b), which may indicate a fissure (or weak boundary) caused by the landslide. Meltwater would be able to flow into the fissure and amplify the local seasonal ground motions, particularly horizontal motions. The EW direction is largely perpendicularly to the strike of the fissure (Fig. 3.11d). As a result, extension and contraction forces associated with snow loading and melting can exert a larger impact on the landslide movements (peak to peak amplitude 1.5 cm) in this direction. The impact in vertical and NS directions was minor (peak to peak amplitudes < 1 cm). It should be noted that the cyclical motions within the landslide displacement time series (Fig. 3.11b) include minor unmodeled periodical errors and biases associated with PPP processing. Many researchers within the geodetic community have been heavily investigating minor errors and biases in the PPP processing (Zumberge et al., 1997;

Kouba and Heroux, 2001, Ge et al., 2008, Wang 2013). The GPS antenna (AC55) was set-up over a rod metallic tripod (Fig. 3.11c). The dilatation of the tripod may also slightly contribute to the seasonal motions.

The landslide seasonal movements can be modeled with cyclical sinusoids as described in Eqn. 4. The red lines in Figure 3.12b represent the modeled cyclical component of the landslide displacements. This model reflects both the seasonal ground motion as well as the It appears that the seasonal signal is not a purely sinusoidal form, featuring a narrow sharp peak in winter (January, February, and March) and a broad peak in summer (June, July, August, and September). The principal cause of seasonal ground motion is snow loading (Freymueller, 2009) and the amount of snow mass in the landslide region may vary year to year. The snow melting and accumulation seasons are not equal every year (Fig. 3.12b). According to snowpack monitoring in Central Alaska (Sousanes, 2012), the landslide area had above normal snowpack during the winter of 2008-2009. As a result, a larger seasonal signal was observed during the winter of 2008-2009 (Fig. 3.12b; Fig. 3.12c). The peak-to-peak amplitudes of landslide displacements (Fig. 3.12c) between the summer of 2008 and the winter of 2008-2009 achieved 1.0 cm (NS), 2.0 cm (EW), and 2.0 cm (UD), which doubled the peak-to-peak amplitudes compared to three other winters.

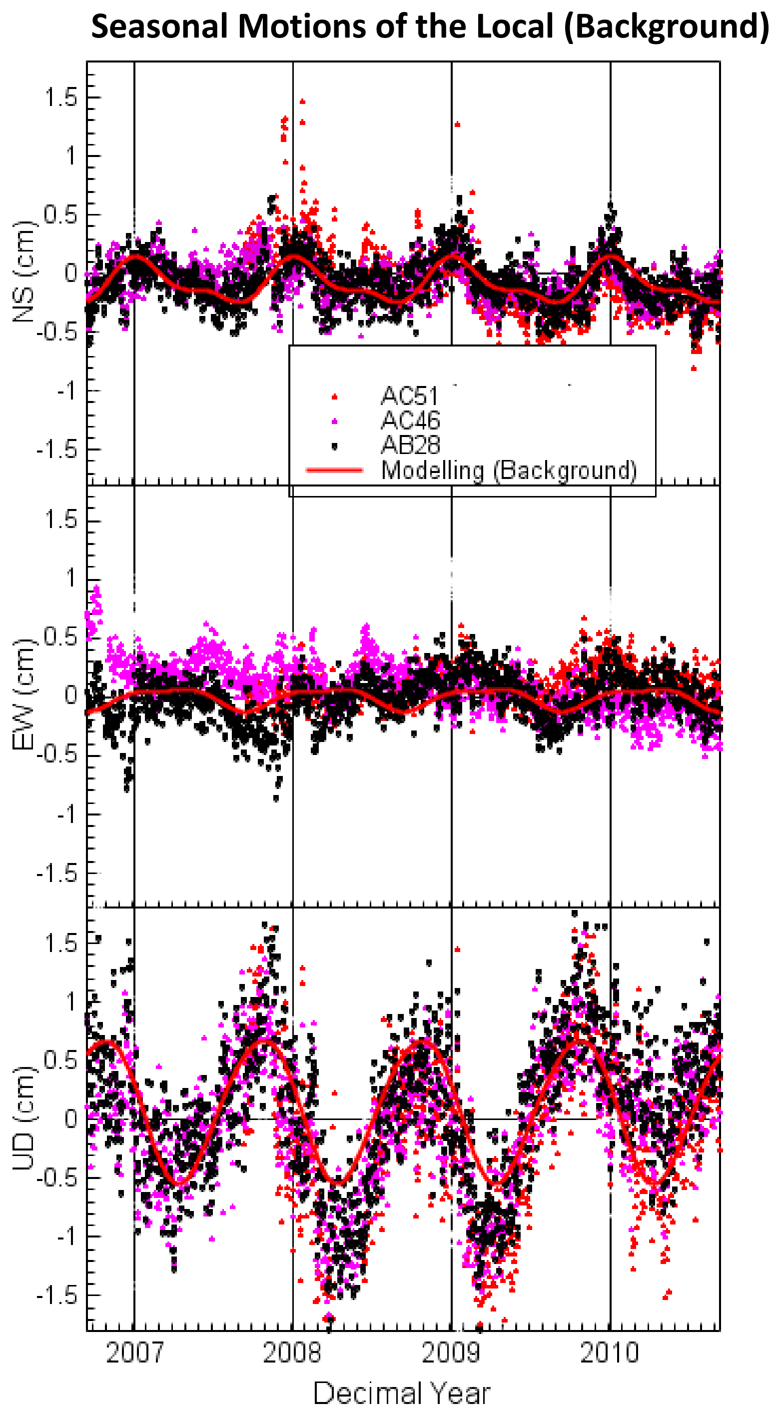

Figure 3.12a: Shows three-component (NS, EW, UD) positional time series for the seasonal motion of the background observed at three reference sites (AC51, AC46, and AB28) during the four-year study period. Positions are referred to the local reference frame realized by five reference stations (Fig. 3.3a). The red lines represent the modeled seasonal motions (Eqn.5). Principal cause of seasonal ground motions is snow loading (Freymueller, 2009). The horizontal (NS, EW) components represents interannual variations and the vertical component represents annual seasonal motions. (North =positive NS, South= negative NS, East= positive EW, West= negative EW, rebound =positive UD, subsidence= negative UD).

Seasonal Motions of the Local (Background)

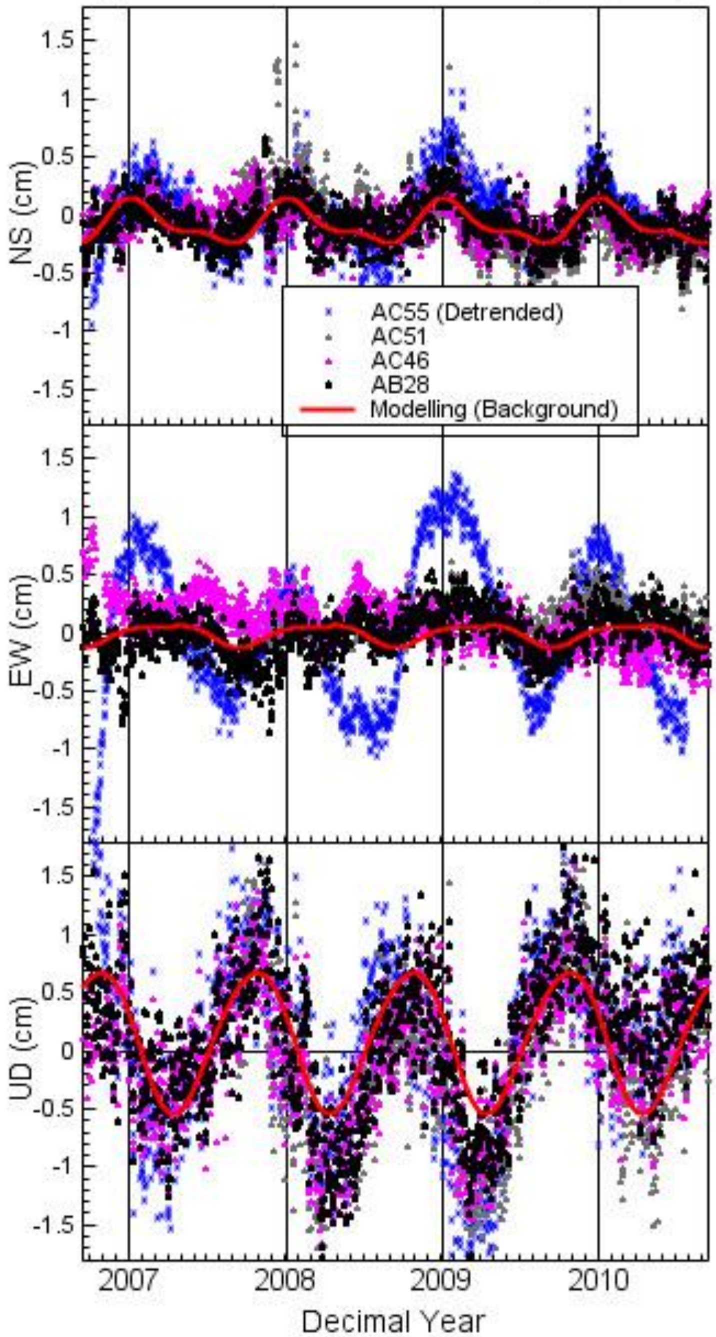

Figure 3.12b: Shows three-component (NS, EW, UD) positional time series for the seasonal motion of the background observed at three reference sites (AC51, AC46, and AB28) including the derived detrended landslide displacement at AC55 (blue marks; Fig. 3.12c). It is evident that AC55 has a greater displacement that the other stations, particularly in the Northing and Easting components. (North =positive NS, South= negative NS, East= positive EW, West= negative EW, rebound =positive UD, subsidence= negative UD).

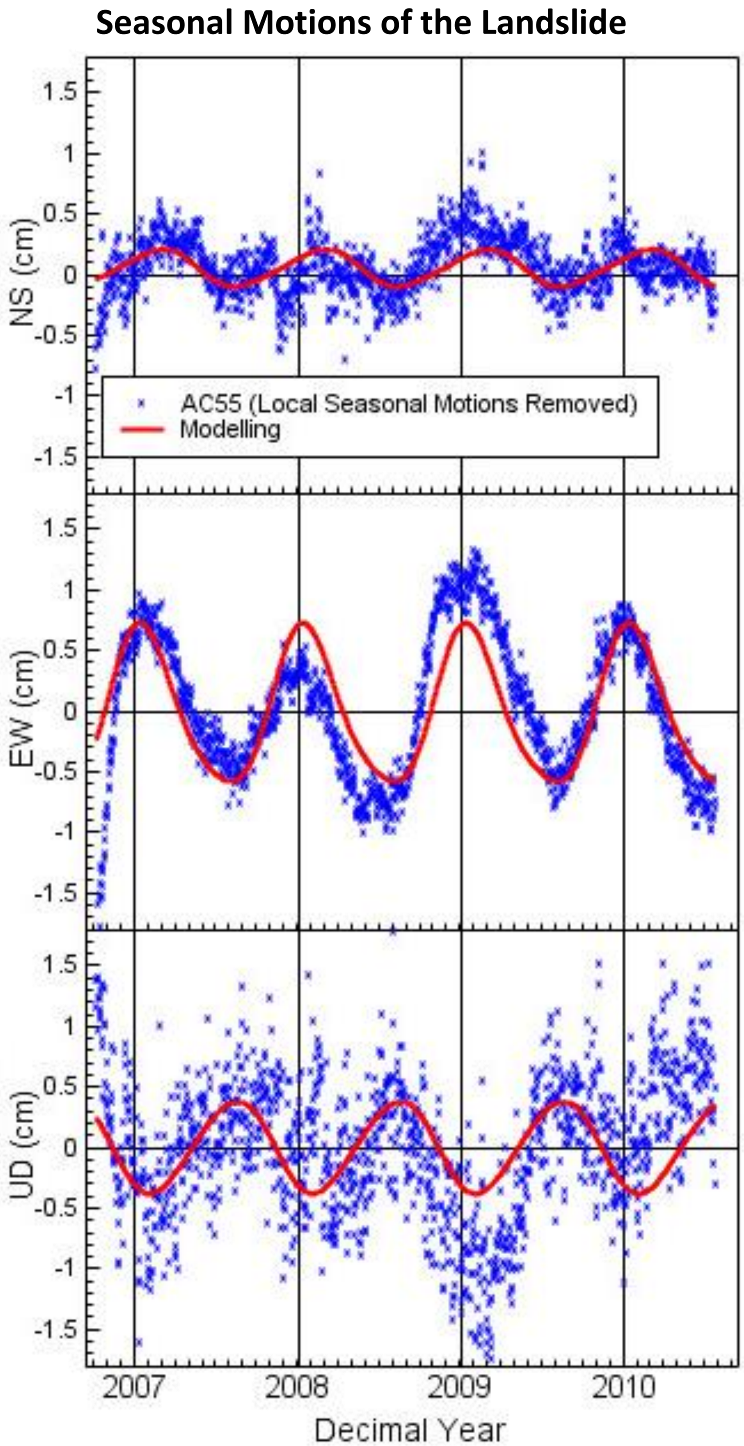

Figure 3.12c: Shows three-component (NS, EW, UD) positional time series for the independent seasonal motion of the landslide. This shows seasonal motions of the landslide (AC55) after removing the modeled local seasonal motions from the Local Reference Frame. The red lines represent the modeled seasonal motions (Eqn.5). (North =positive NS, South= negative NS, East= positive EW, West= negative EW, rebound =positive UD, subsidence= negative UD).

3.6 RESULTS

This landslide moves toward N 75° E with a steady velocity of 5.5 cm/year horizontally and a steady subsidence rate of 2.6 cm/year (Fig. 3.13) relative to the local stable reference frame (Fig. 3.5; Fig. 3.6). The local reference frame is able to provide an accuracy of ±1.5 mm/year for local ground deformation studies. There was a strong correlation between annual snow loading and melting cycles and seasonal variations in ground motion. GPS position data shows this seasonal variation from year to year with an average peak-to-peak amplitude of 1.5 cm in the horizontal (0.5 cm (NS); 1.5 (EW)) and 1.0 cm in vertical directions. Although the GPS position data for AC55 shows seasonal variation in ground motion (Fig. 3.12a-c) this is common to entire the reference frame. Therefore no seasonal signal is observed in the landslide motion (Fig. 3.13) producing a steady non-cyclical motion.

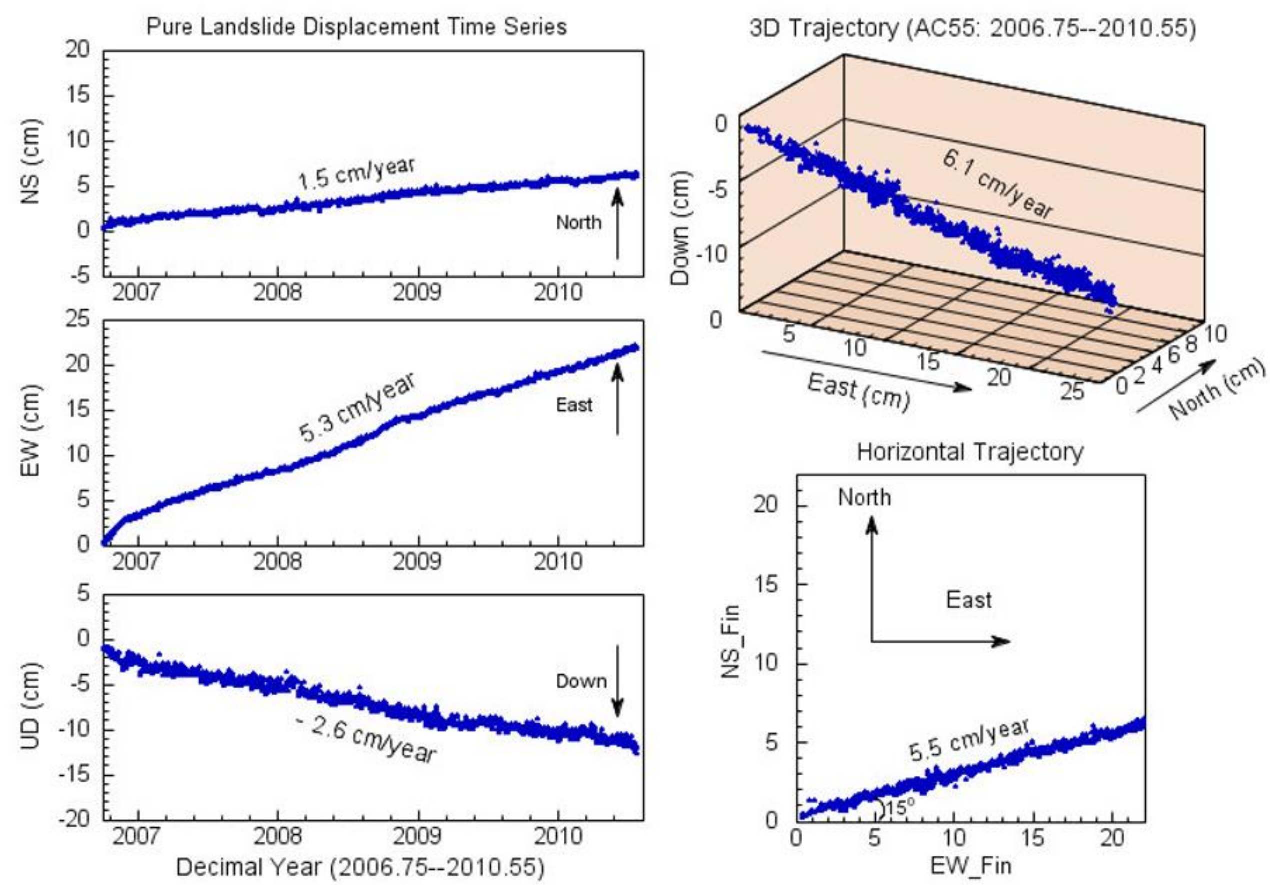

Figure 3.13: (a-b) Three-component landslide displacement time series (the left column) and the positional trajectories in three-dimensional space and horizontal plane (the right column). The local seasonal ground motions (Fig. 3.12b) and the cyclical motions of the landslide (Fig. 3.12c) have been removed from the GPS-derived antenna positional time series (Fig. 3.10). (North =positive NS, South= negative NS, East= positive EW, West= negative EW, rebound =positive UD, subsidence= negative UD).

4 REMOTE SENSING OBSERVATIONS

4.1 GRACE

Geodetic observations using Gravity Recovery and Climate Experiment (GRACE) provide extremely accurate intersatellite range-rate measurements to study the kinematics and dynamics of the solid Earth, cryosphere, and hydrosphere. It provides a remote sensing technique for measuring changes in total water storage (ice, snow, surface waters, soil moisture, groundwater) over continental areas, GRACE-based Total Water Storage (TWS) variations shows that the snow component has a more significant impact at high latitudes than TWS (Frappart et al., 2011c). The interannual seasonal variability was calculated over the regional extent of the study area (Fig. 4.1).

To better understand the seasonal variability on the vertical displacement GPS data, the seasonal hydrological mass signal was derived from GRACE observations. Seasonal displacements are significant and GPS-observed and GRACE-modeled seasonal displacements are highly correlated as seen in Figure 4.2 (Fu, 2012). This consistency demonstrates that the seasonal position oscillations in southern Alaska are mainly caused by long-wavelength hydrological mass loading (Fu and Freymueller, 2012). This seasonal signal has a large long-term mass loss of -5.74 cm/yr. as illustrated in Figure 4.1 (Arendt et al., 2002, Chen et al., 2006, Larsen et al., 2007; Fu and Freymueller, 2012).

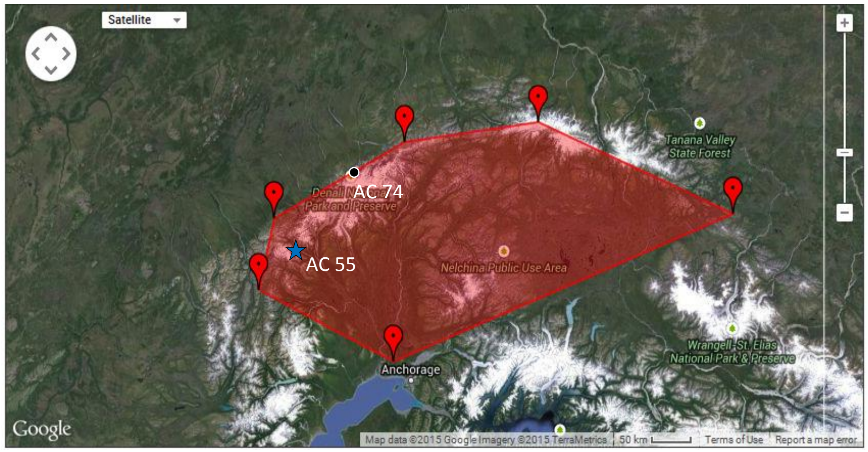

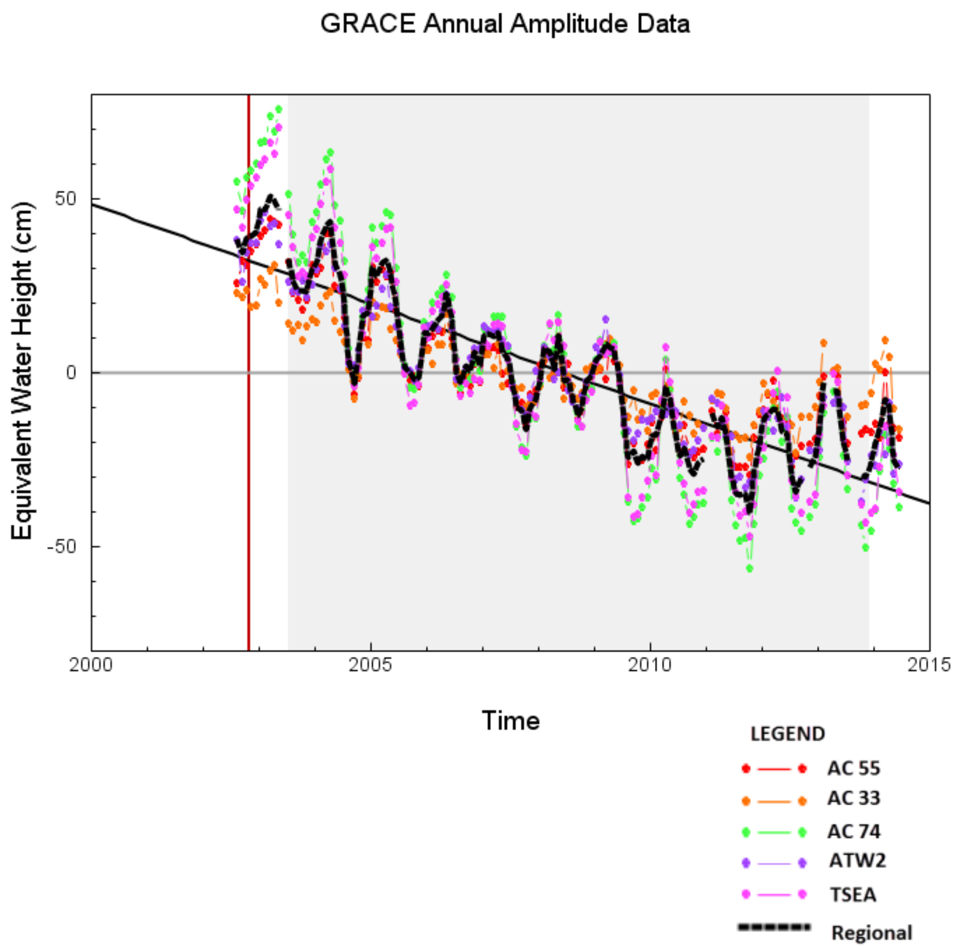

Figure 4.1: Seasonal Hydrological Signal. Regional GRACE Data extent (surrounding the study GPS stations) used to extract a seasonal signal at the top. GPS Stations AC55 and AC74 are highlighted in this figure and are discussed again in Figure 4.2. The bottom is a plot of the derived GRACE Satellite Water Equivalent time series. This figure represents seasonal GRACE data over the entire region (black) as well as at individual GPS station locations. Over the period from November 2002 until November 2013 there is a linear trend of -5.74 cm/ year hydrological mass loss.

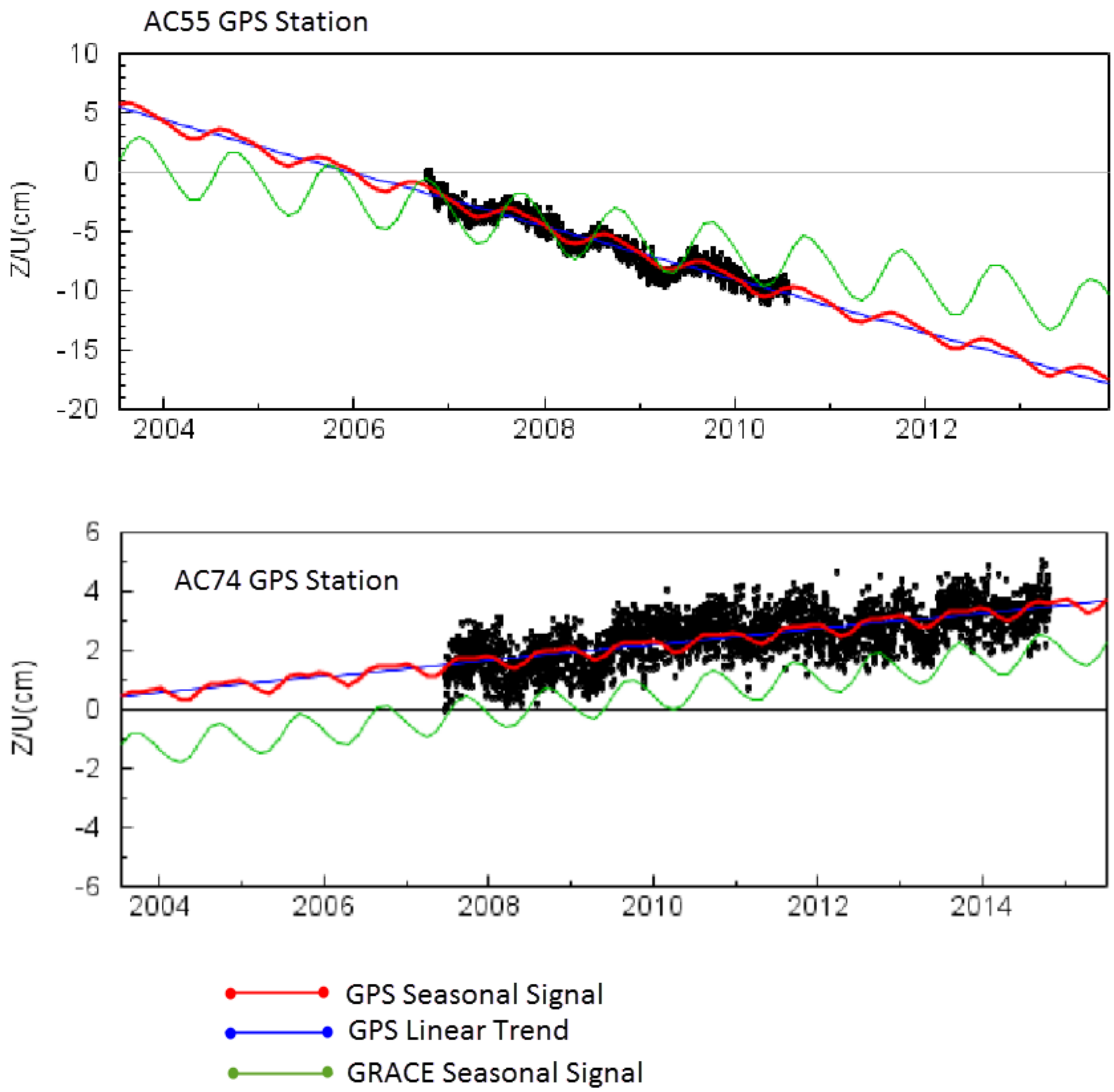

Figure 4.2: Seasonal Signal Correlation of GPS-observed data and regional GRACE seasonal signal for AC55) and AC74. The plot is of the derived Water Equivalent Height [Z/U(cm)] over time. The correlation is more consist at AC74 due to the landslide motion at AC55.

4.2 SATELLITE IMAGERY

In recent years, the use of digital remote sensing data in landslide assessments has become prevalent. As mentioned earlier, landslides are a significant natural hazard in mountainous regions and heavily scarred slopes in vegetated regions are indicators of landslides (Vohora and Donoghue, 2015). It is difficult to detect ongoing slope failure remotely but after identifying landslide events; satellite imagery can be a great tool to delineate features, calculate extent and possibly measure velocity of surface motion.

In order to validate the GPS-derived landslide model, satellite imagery tools were utilized. Due to poor spatial resolution and temporal resolution, using remote sensing raster imagery to quantify features associated with the slow creeping (~ 5 cm/year) landslide was challenging. Trying to resolve that would require a large temporal scale (decades' worth of data acquisition) or high spatial resolution tool, such as LIDAR.

Given that the study area is in a remote area exhibiting minimal hazard, there was limited access to good quality repeated aerial or satellite data acquisitions. This study utilizes DEM (Interferometric Synthetic Aperture Radar GeoSAR Digital Elevation Model with a 5 meter resolution, acquisition obtained in July 2010) and Landsat data from 1983 to 2010. Nonetheless, more recent digital elevation models (DEM) were able to identify some parameters (Fig. 4.3; Fig. 4.4). The lack of high resolution data hinders the calculation of the changing landslide dimensions. However there are detectable features of the landslide as seen in the Landsat images (Fig. 4.6; Fig. 4.7). Rough estimates of the area range from 11,000 m^2 to 15,000 m^2, varying greatly on the lateral extent of the landslide.

Most earth observation satellites record in several spectral bands meaning the satellite records a number of small wavelength intervals within the electromagnetic spectrum (visible light, near and short wave infrared). Using Landsat MSS and TM/ETM+ spectral bands (Table 4-1), it is possible to create composite images by combining wavelength bands (Fig. 4.5). This method is often preferred because specific combinations highlight different features such as land/water interface or soil/ vegetation boundary (Appendix D).

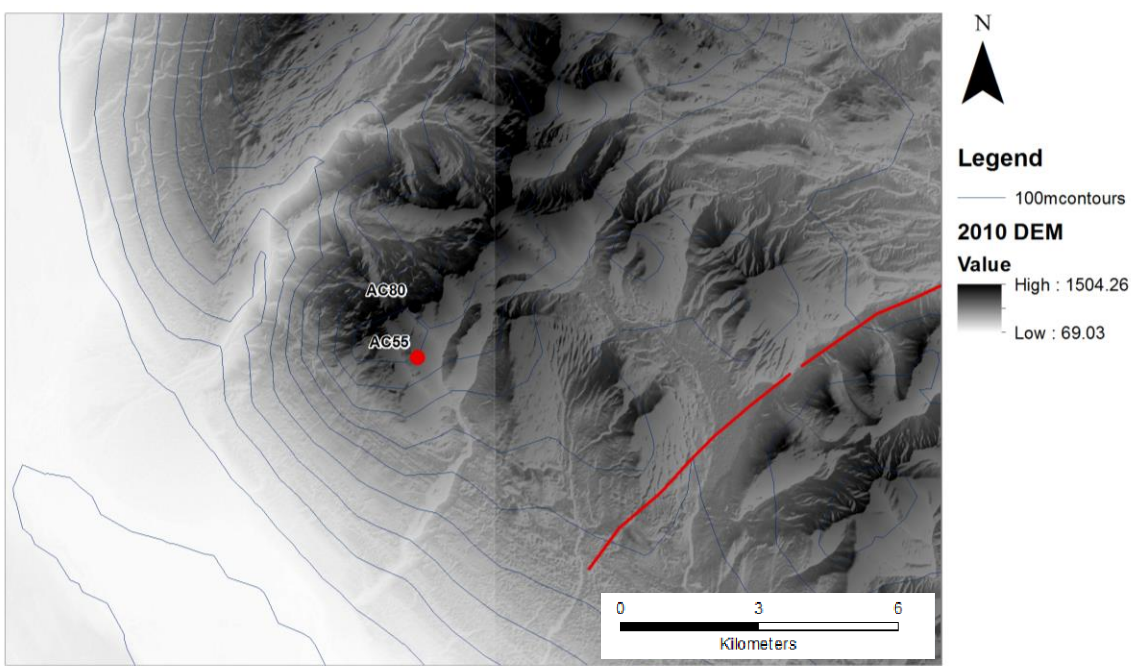

Figure 4.3: Digital Elevation Model Images of AC55, with a spatial resolution of 5 meters. The elevation at AC55 is 1,035 m above sea level and the landslide orientation is NW to SE. The red line is the inactive Pass Creek fault.

Slope

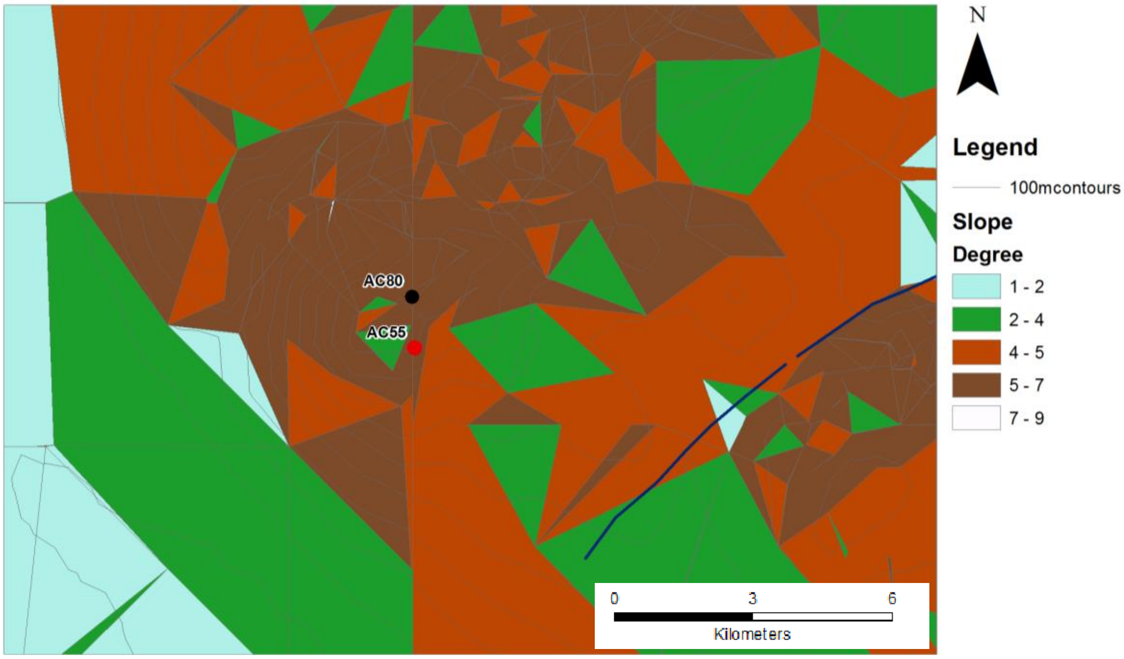

Aspect

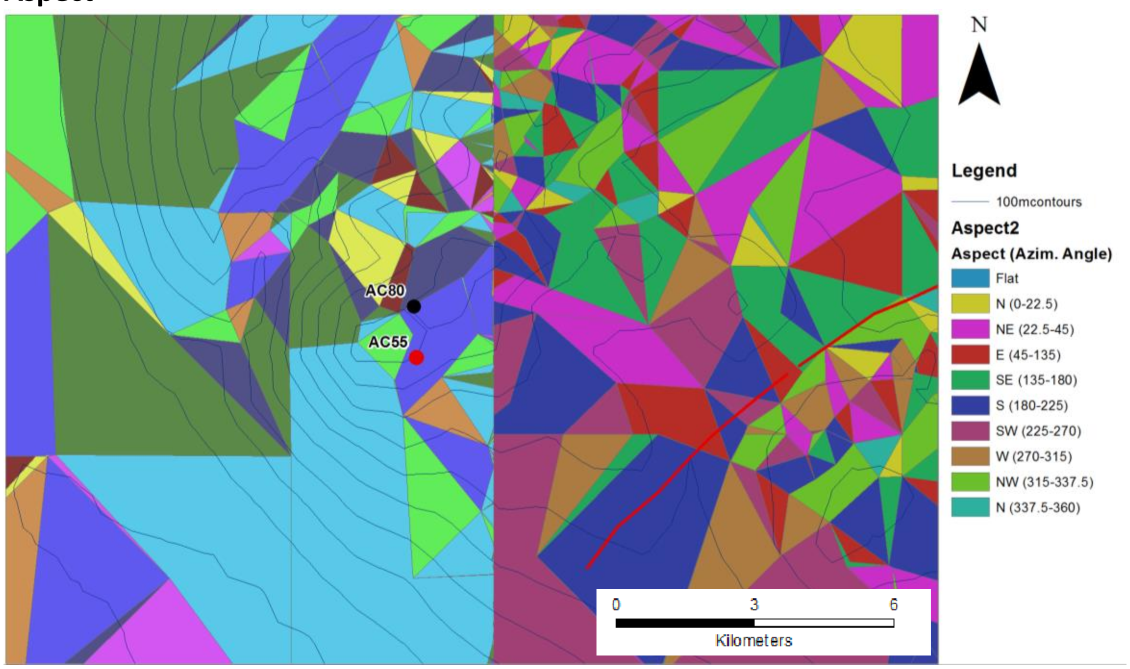

Figure 4.4: Based on the 5 meter DEM a Triangulated Irregular Network was created to calculate slope and aspect. Mean slope is a gentle 5-8°. The aspect direction is South Easterly at ~ 150° azimuth. Aspect is a valuable tool in mountainous regions because it calculates the solar illumination for each segment of the elevation data. Southerly slopes in a mountainous region are well identified location where snow is likely to melt first and produce runoff (Burrough and McDonnell, 1998).

Considering that vegetation health is a dominant factor in landslides, satellite observations are heavily influenced by the spectral indices of vegetation in the near-infrared and visible (red) wave bands, and are widely selected to measure green vegetation density (Jensen, 2006). Healthy vegetation reflects strongly in the near-infrared region of the electromagnetic spectrum (Fig. 4.5), whereas burnt, dying, or diseased vegetation has a decreased reflectance in this region (Fraser et. al., 2000; Vohora and Donoghue, 2004). Vegetation indices (VI's) are mainly derived from reflectance data from discrete red (R) and near-infrared (NIR) bands (Vohora and Donoghue, 2015). LANDSAT data, which uses near and mid-infrared is therefore useful to establishing vegetation indices that distinguish burned areas, and to classifying these into damage classes (Siegert and Hoffman, 2000; Rogan and Yool, 2001). One of these vegetation indices, NDVI normalized difference vegetation index, was used in this study (Vohora and Donoghue, 2015; Bannari et. al., 1995). The equations for producing NDVI using LANDSAT bands are:

Landsat TM or ETM Plus: $$\mathrm{NDVI} = \frac{(\mathrm{TM4}-\mathrm{TM3})}{(\mathrm{TM4}+\mathrm{TM3})} \quad \text{(Eqn. 6)}$$

Landsat MSS: $$\mathrm{NDVI} = \frac{(\mathrm{B7}-\mathrm{B5})}{(\mathrm{B7}+\mathrm{B5})}\ * \quad \text{(Eqn. 7)}$$

*the band designation changes during the Landsat 3 and Landsat 4 mission. In the MSS bands B7 is equivalent to TM 4 and B5 is equivalent to TM2 (0.6-0.7 micrometers). Refer to Table 4.1 for Landsat Spectral Band information (wavelengths and resolution).

NDVI spectral index is represented as a ratio of the reflected over the incoming radiation in each spectral band individually, and produces an index that varies between -1.0 and +1.0 The NDVI composite raster highlights the health or stress of the vegetation. Healthy vegetation shows higher values, where the bare earth surface show low values, close to zero (-0.1 to 0.1).

Table 4.1. Landsat Spectral Bands/ Wavelengths (micrometers)

Landsat MSS			Landsat TM and ETM+		
Spectral Band	**Wavelength**	**Resolution**	**Spectral Band**	**Wavelength**	**Resolution**
Band 1: Green	0.5-0.6	79 m	Band 1: Blue	0.45-0.52	30 m
Band 2: Red	0.7- 0.7	79 m	Band 2: Green	0.52-0.61	30 m
Band 3: Near IR	0.7- 0.8	79 m	Band 3: Red	0.63-0.69	30 m
Band 4: Near IR	0.8- 1.1	79 m	Band 4: Near IR	0.76-0.90	30 m
Band 5: Thermal IR	10.4-12.6	240 m	Band 5: Near IR	1.55-1.75	30 m
			Band 6: Thermal IR	10.40-12.50	120 m
			Band 7: Far IR	2.08-2.35	30 m
			Band 8: Pan *	0.52-0.90	15 m
http://landsat.usgs.gov/			* Panchromatic band available in Landsat 7		

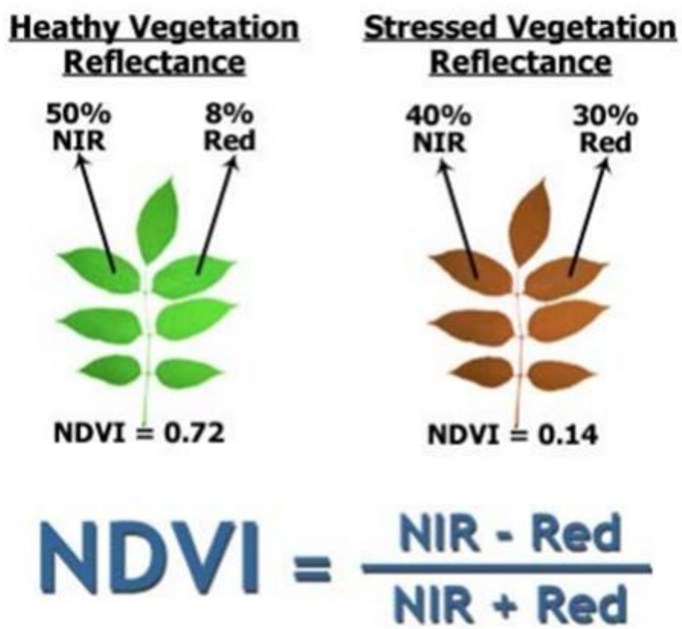

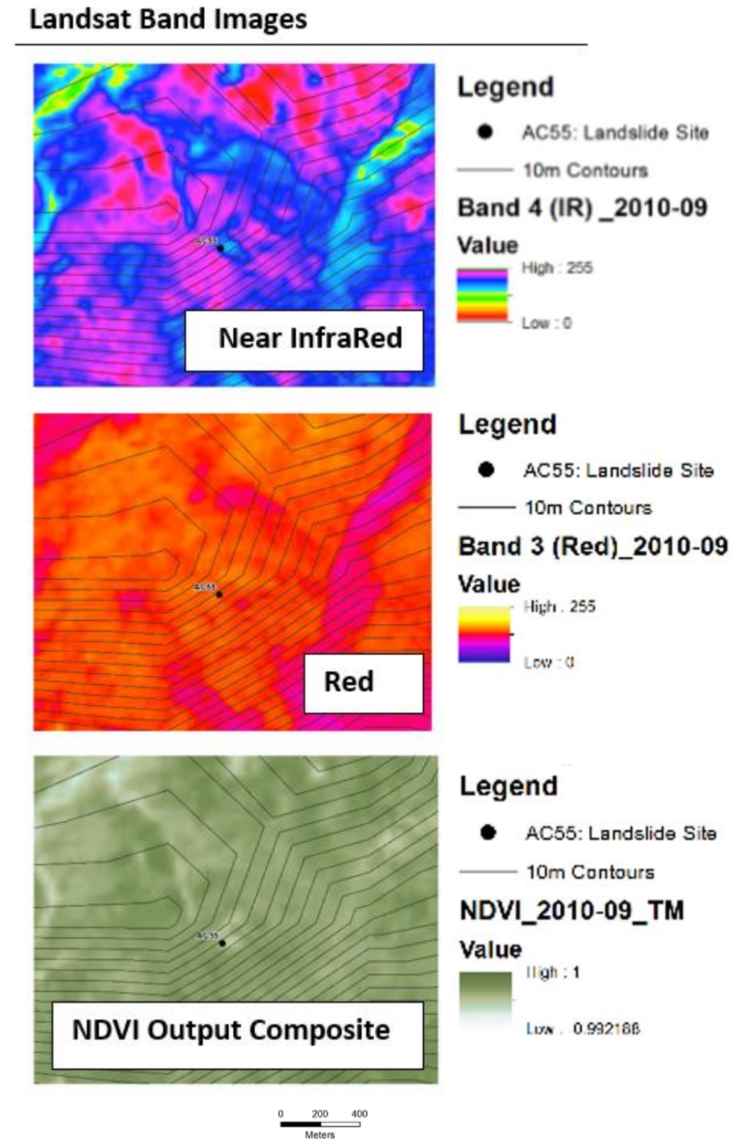

Figure 4.5: NDVI calculation produces a composite raster that highlights the health or stress of the vegetation. Healthy vegetation shows higher values, whereas the bare earth has low values (Fig. 4.6). NDVI is used to monitor crop growth, warn of impending drought, generate biomass maps for carbon trading and characterize the seasonal photosynthetic activity.

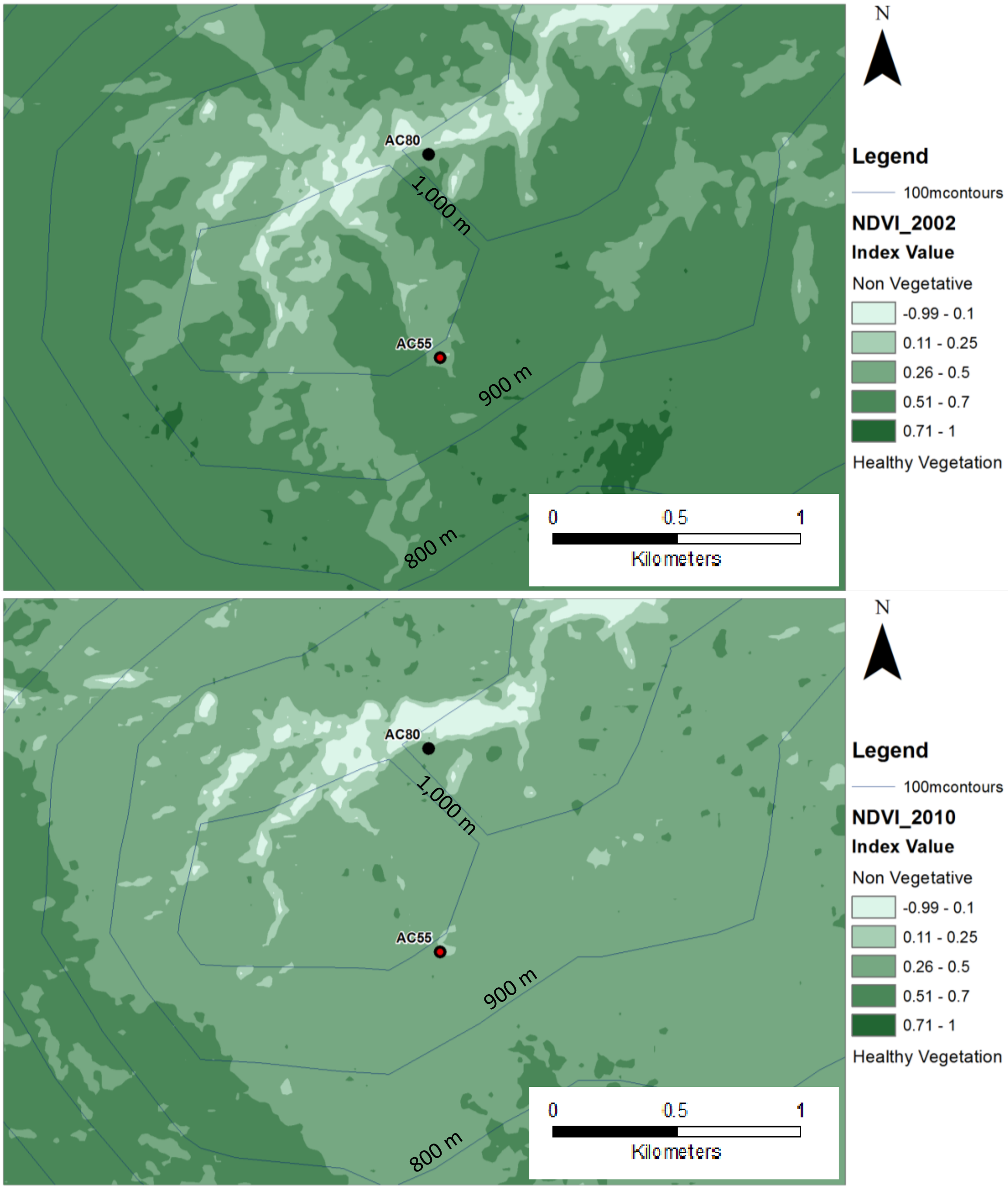

Figure 4.6: Landsat images of AC55 from May 2002 (top) and September 2010 (bottom). NDVI composite images highlighting the health of the vegetation. Light colors are bare earth indicative of surface deformation such as landslides. The composites were calculated using Landsat TM/ETM+ images that have a 30 m resolution. The extent of the landslide is difficult to measure but there is a curved bare earth surface around AC55 that has some variability over time. NDVI Image is displayed using Bilinear Interpolation for continuous data and using a standard deviation of 2.5.

Using NDVI Landsat imagery, it is evident that although there are common areas of non-vegetation but overall the entire hillside can be classified stressed vegetation (Fig. 4.6). In the 2010 image the light colored shaped at AC55 (Fig. 4.7) could be comprised of two independent trends. The trend along the red arrow is the stressed vegetation along the landslide horizontal displacement, and the other along the red dashed line is along the potentially weak landslide boundary has been created perpendicular to the slide direction.

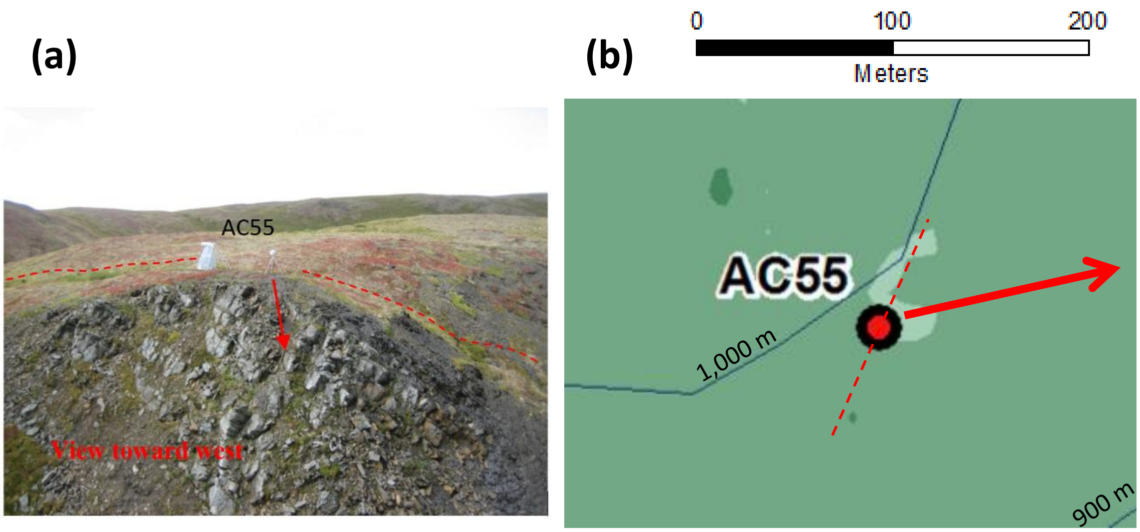

Figure 4.7: NDVI Summary. (a) The landslide displacement vector is estimated according to the results showing in Figure 3.13. The red dashed line behind the GPS station illustrates the potential landslide boundary, where a heavy vegetation lineament can be seen (from Fig. 3.11). (b) Enlarged view of the 2010 NDVI Composite raster (from Fig. 4.6), with the horizontal component of motion in red and a perpendicular potential weak boundary zone.

5 DISCUSSION

5.1 AC55 LANDSLIDE SUMMARY

This study demonstrates a procedure for deriving landslide movements from continuous GPS observations in Alaska, a tectonically active and cold region. The techniques outlined in this study have identified and filtered the daily positions biased by snow and ice accumulated on GPS antennas within the study area; tested and adopted a stable local reference frame; excluded common local seasonal ground motions observed in all the stations within the Local Reference Frame; and recovered the independent displacement time series and cyclical component of the landslide movements (Fig. 3.12c).

This landslide moves toward N 75° E with a steady velocity of 5.5 cm/year horizontally and a steady subsidence rate of 2.6 cm/year (Fig. 3-13) relative to the local stable reference frame (Fig. 3.3a; Fig. 3.5). The local reference frame is able to provide an accuracy of ±1.5 mm/year for local ground deformation studies. Although the GPS position data contains many outliers to the modeled seasonal signal for the ground motion at AC55 (Fig. 3.12b; Fig. 3.12c), particularly after the heavy snowfall in 2008-2009; that seasonal signal does not contribute to the landslide motion (Fig. 3.13).

5.2 LANDSLIDE COMPARISION

5.2.1 ANALOG METHODOLOGY

A similar GPS processing method was conducted in a two-year GPS landslide monitoring project (Wang 2012; Wang and Soler 2012; Wang 2013b) conducted in Puerto Rico for two active landslides. In order to conduct a high-accuracy GPS landslide-monitoring project, a stable Puerto Rico Virgin Island Reference Frame (SPRVIRF) was established. The root mean square (RMS) of the PPP solution within this reference is about 2 mm in the horizontal and 6 mm in the vertical, which produce an uncertainty below 0.5 mm/year.

One landslide is located in Ponce, Puerto Rico, in an urban environment that caused property damage. For this landslide, a rover GPS station was installed on the sliding mass and a reference station was installed outside the sliding mass, with a baseline length between the reference and rover set to 130 m. This short baseline provides sub-millimeter accuracy for daily solutions derived from double difference processing (Wang 2013). As a result of this high accuracy, the differential results can be regarded as the real position of the landslide motion and is termed “truth” (Fig. 5.1).

The other is located in a remote heavy rainforest of the El Yunque National Rainforest Park in northeast Puerto Rico. El Yunque landslide monitoring project installed one reference station and two rover stations. The daily displacement time series of the two GPS sites on the El Yunque landslide are relative to SPRVIRF local reference frame (Fig. 5.2). The daily displacement time series were derived from the PPP solutions. The PPP processing does not need any ground reference data. The local reference frame makes it possible to get high-accuracy GPS monitoring in the remote area without installing any reference stations and without employing complex post-data processing (Wang et al., 2014).

In both of these landslides there is a long pre-failure stage with a slow steady displacement, until the slope fails and is followed by the post failure stage. El Yunque landslide has two failure events due to the increased precipitation in the rainforest. This displacement trend is not representative of the landslide motion at AC55.

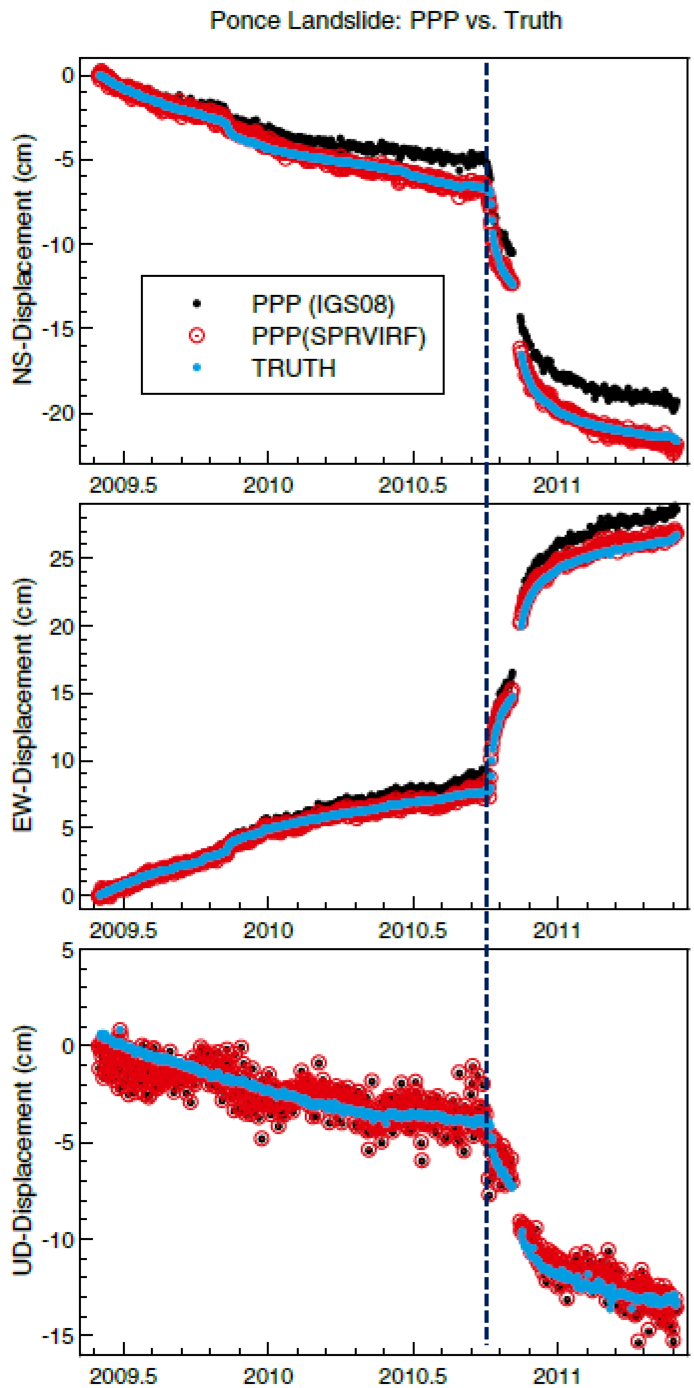

Figure 5.1: Three-component displacement time series of the Ponce landslide derived from the double difference solutions ("truth") and the PPP solutions. The PPP solutions are relative to IGS08 (black) and SPRVIRF (red). The double difference solutions (blue) are relative to a fixed reference station 130 m away from the landslide site (Wang et al., 2011; Wang et al., 2012; Wang et al., 2013; Wang et al., 2014). The relative motion is to the South (negative NS values), East (positive EW values) and vertical subsidence (negative UD values). The dashed blue line indicates the point of slope failure.

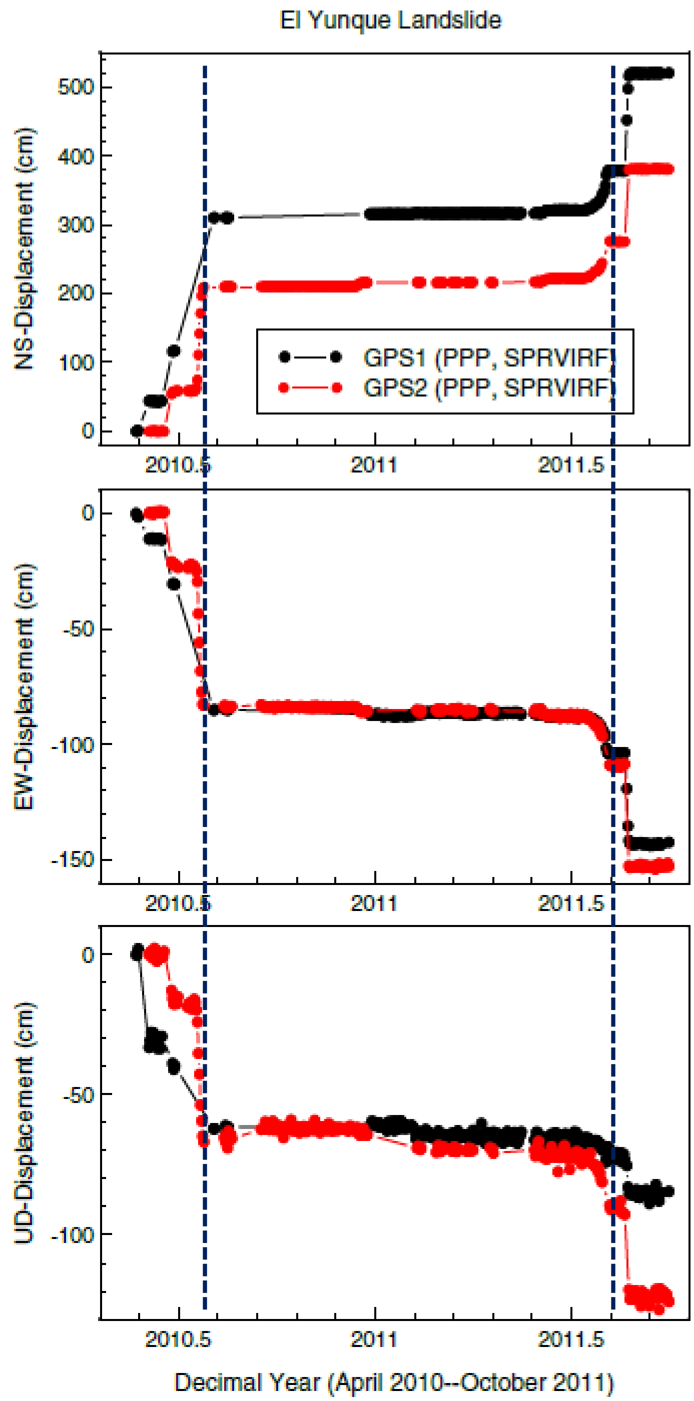

Figure 5.2: Three-component displacement time series of two GPS stations installed on the El Yunque National Rainforest Park landslide. The displacement time series are derived from the PPP solutions and transformed to the local reference frame (SPRVIRF) (Wang et al., 2011; Wang et al., 2012; Wang et al., 2013; Wang et al., 2014). The relative motion is to the North (positive NS values), West (negative EW values) and vertical subsidence (negative UD values). The dashed blue line indicates the point of slope failure.

5.2.2 ANALOG TECTONICALLY

The Slumgullion landslide, located in the San Juan Mountains of south-western Colorado (Lake City, CO), is one of the most famous slope movements in North America (Gomberg et al., 1995; Coe et al., 2003). The parallel ridges of the Slumgullion strike-slip fault bind this landslide. Gomberg et al. (1995) installed creepmeters to conduct a long-term analysis of the landslide and determined that it moves with a steady rate of ~ 15mm/ day. The data (Fig. 5.3) shows some seasonal variability and Gomberg et al. (1995) concluded that this maybe a result of fault rheology or perhaps seasonal pore-pressure variations.

Although this landslide is orders of magnitude larger than the landslide at AC55, there are some common features. The displacement trend (Fig. 5.3a) of Slumguillion land mass is similar to the landslide motion at AC55. Both are in alpine regions and are heavily influenced by tectonics that can produce rapid displacement (Fig. 5.3b). The cause of the steady displacement at Slumguillion is spring snowmelt (Gomberg et al., 1995; Coe et al., 2003). The cause of the steady displacement velocity at AC55 is not fully understood. As previously mentioned landslides in permafrost regions have thermal complexities and requires geotechnical site investigation (borehole drilling, exploratory audits, and seismic refraction) and monitoring activities (ground surface and deep displacements, pore pressures, thermal modeling) in order to understand the kinematics of the landslide motion.

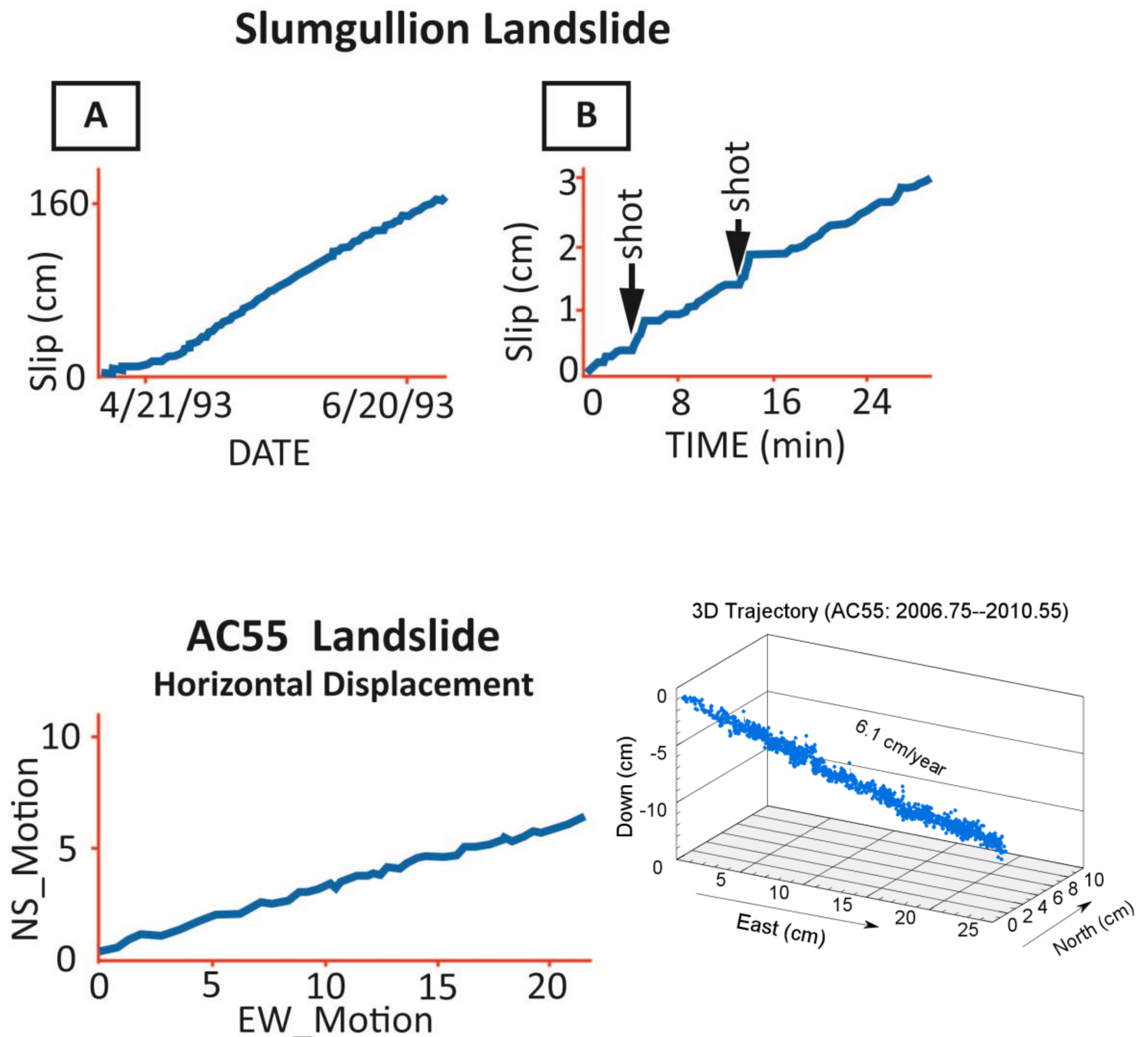

Figure 5.3: Slumgullion-AC55 Landslide Comparison. (Top) Creep measured across slide-bounding strike- slip fault on Slumgullion landslide (A) Change in slope in both cases probably is due to increased climatic moisture, i.e. snow melt on Slumgullion landslide (W. Savage and R. W. Fleming, unpublished). (B) Creep events measured after explosions (shots) near Slumgullion landslide (Gomberg et al., 1995). (Bottom) Pure Landslide Horizontal Displacement Time Series and 3D Trajectory for AC55.

6 CONCLUSION

The landslide at AC55 moves with a constant velocity of 5.5 cm/year horizontally (towards N 75° E) and a steady subsidence rate of 2.6 cm/year relative to the local stable reference frame, to an accuracy of ±1.5 mm/year.

In addition to the climatic seasonal variation the modeled background surface motion also removes common post-seismic deformation. Although there are some residual seasonal contributions from the winter of 2008, which are outliers from the modeled seasonal background motion (Fig. 3.12c), the seasonal signal is not contributing to the landslide motion (Fig. 3.13).

The cause of the steady displacement velocity at AC55 is not fully understood. As previously mentioned landslides in permafrost regions have thermal complexities and requires geotechnical field investigation and long-term monitoring activities in order to discern the cause and the kinematics of the landslide motion.

The wider implications of this study is that this new process can be applied to landslide studies in other tectonically active and/or cold regions. These publicly available long-history (> 5 years) GPS stations will allow researchers to establish stable local-scale reference frames for studying local ground deformations in many regions, which make it possible to conduct precise landslide monitoring with a "stand-alone" GPS station using the PPP processing. This approach will significantly reduce costs and logistics for conducting long-term landslide monitoring using GPS. Therefore, it is an attractive alternative to the conventional landslide survey techniques.

7 REFERENCES

Alaska Earthquake Information Center (2014). M7.9 Denali Fault Earthquake of November 3, 2002. Seismological Society of America. Retrieved 10 8, 2014, from http://www.aeic.alaska.edu/Denali_Fault_2002/

American Geophysical Union, AGU (2015). The Landslide Blog. Retrieved on April 20, 2015, from http://blogs.agu.org/landslideblog/2009/11/30/slumps-caused-by-thawing-ground-on-mars-and-earth/

Arendt, A., Eschelmeyer, K., Harrison, W., Lingle, C., Zirnheld, S., Valentine, V., Ritchie, B., Druckenmiller, M. (2006). Updated estimates of glacier volume changes in the western Chugach Mountains, Alaska, and a comparison of regional extrapolation methods. Journal of Geophysical Research 111, pp. 2156-2202

Bannari, A., Morin, D., Bonn, F., Huete, A. R. (1995). A review of vegetation indices. Remote Sensing Reviews, 13, pp. 95-120.

Barclay, D.J., Wiles, G.C., Calkin, P.E. (2009). Tree-ring crossdates for a first millennium AD advance of Tebenk of Glacier, southern Alaska. Quaternary Research 71, pp. 22–26.

Bawden, G. W., Johnson, M. R., Kasmarek, M. C., Brandt, J., and Middleton, C. S. (2012). Investigation of Land Subsidence in the Houston-Galveston Region of Texas by Using the Global Positioning System and Interferometric Synthetic Aperture Radar, 1993–2000. Denver, CO: U.S. Geological Survey Scientific Investigations Report 2012–5211.

Bemis, S., Carver, G., Koehler, R. (2012). The Quaternary thrust system of the northern Alaska Range. Geosphere 8 (1), pp. 196-205.

Bertiger, W., Desai, S. D., Haines, B., Harvey, N., Moore, A. W., Owen, S., and Weiss, J. P. (2010). Single receiver phase ambiguity resolution with GPS data. Journal of Geodesy, 84(5), pp. 327-337.

Bevis, M., Alsdorf, D., Kendrick, E., Fortes, L.P., Forsberg, B., Smalley Jr., R., and Becker, J. (2005). Seasonal fluctuations in the mass of the Amazon River system and Earth's elastic response. Geophysical Research Letters 32, pp. 471-475.

Blewitt, G. (1989). Carrier phase ambiguity resolution for the Global Positioning System applied to geodetic baselines up to 2000 km, Journal of Geophysical Research: Solid Earth (1978–2012), 94(B8), pp. 10187-10203.

Blewitt, G., Heflin, M.B., Webb, F.H., Lindqwister, U.J., Malla, R.P. (1992). Global coordinates with centimeter accuracy in the International Terrestrial Reference Frame using GPS. Geophysical Research Letters, 19(9), pp. 853-856.

Blewitt, G., Lavalle´e, D., Clarke, P., Nurutdinov, K. (2001). A new global mode of Earth deformation: seasonal cycle detected. Science 294, pp. 2342–2345.

Brabets, T. P., Nelson, G. L., Dorava, J. M., and Milner, A. M. (1999). Water-Quality Assessment of the Cook Inlet Basin, Alaska — Environmental Setting Basin, Alaska — Environmental Setting. U.S. Geological Survey, Report 99-4025.

Burrough, P. A., and McDonell, R. A. (1998). Principles of Geographical Information Systems. Oxford University Press, New York,190 p.

Chen, J.L., Wilson, C.R. and Tapley, B.D. (2006). Satellite gravity measurements confirm accelerated melting of Greenland Ice Sheet, Science, 313, pp. 1958-1960.

Coe, J.A., Ellis, W.L., Godt, J.W., Savage, W.Z., Savage, J.E., Michael, J.A., Kibler, J.D., Powers, P.S., Lidke, D.J., Debray, S. (2003). Seasonal movement of the Slumgullion landslide determined from Global Positioning System surveys and field instrumentation, July 1998 – March 2002. Engineering Geology, 68, pp. 67-101.

Cohen, S. C., & Freymueller, J. T. (1997). Deformation of the Kenai Peninsula, Alaska. Journal of Geophysical Research: Solid Earth (1978–2012), 102, pp. 20479-20487

Cohen, S.C., Freymueller, J.T. (2004). Crustal deformation in Southcentral Alaska: The 1964 Prince William Sound earthquake subduction zone. Advanced Geophysical 47, pp. 1–63.

Dach, R., Hugentobler, U., Fridez, P. and Meindl, M. (2007) Bernese GPS Software Version 5.0, Astronomical Institute, University of Bern, Bern, 612 p.

Dai, F.C., Lee, C.F., Ngai, Y.Y (2002). Landslide risk assessment and management: an overview. Engineering Geology 64, pp. 65–87.

Darrow, M.M., Bray, M.T., Huang, S.L. (2012) Analysis of a deep-seated landslide in permafrost, Richardson Highway, south-central Alaska. Environmental & Engineering Geoscience, 18(3), pp. 261-280.

Dawson, J., and Woods, A. (2010). ITRF to GDA94 Coordinate Transformations. Journal of Applied Geodesy, 4, pp. 189-199.

Dong, D., Dickey, J.O., Chao, Y., Cheng, M.K. (1997). Geocenter variations caused by atmosphere, ocean, and surface ground water. Geophysical Research Letters 24, pp. 1867– 1870.

Dong, D., Fang. P., Bock, Y., Cheng, M.K., Miyazaki, S. (2002). Anatomy of apparent seasonal variations from GPS-derived site position time series. Journal of Geophysical Research 107, ETG9-1/18.

Dow, J.M., Neilan, R.E., Rizos, C. (2009). The International GNSS Service in a changing landscape of Global Navigation Satellite Systems. Journal of Geodesy 83, pp. 191-198.

EarthScope (2014). The National Science Foundation (NSF) funded project. Retrieved 04 18, 2013, from http://www.earthscope.org

Eberhart-Phillips D., Haeussler, P.J., Freymueller, J.T., Frankel, A.D., Rubin, C.M., Craw, P., Ratchkovski, N.A., Carver, G.A., Crone, A.J., Dawson, T.E., Fletcher, H., Hansen, R., Harp, E.L., Harris, R.A., Hill, D.P., Hreinsdóttir, S., Jibson, R.W., Jones, L.M., Kayen, R., Keefer D.K., Larsen, C.F., Moran, S.C., Personius, S.F., Plafker, G., Sherrod, B., Sieh, K., Sitar, N., Wallace, W.K. (2003). The 2002 Denali Fault Earthquake, Alaska: A large magnitude, slip-partitioned event. Science 300(5622), pp. 1113-1118.

Firuzabad , D., and King, R. W. (2012). GPS precision as a function of session duration and reference frame using multi-point software. GPS Solutions 16(2), pp 191–196.

Freymueller, J.T., Woodard, H., Cohen, S., Cross, R., Elliott, J., Larsen, C., Hreinsdottir, S., Zweck, C. (2008). Active deformation processes in Alaska, based on 15 years of GPS measurements. Active tectonics and seismic potential of Alaska. AGU Geophysical Monogram Series 179, pp. 1-42.

Freymueller, J. T. (2009). Seasonal position variations and regional reference frame realization. In Geodetic Reference Frames. Springer Berlin Heidelberg, pp. 191-196.

Frappart, F., Papa, F., Güntner, A., Werth, S., Santos da Silva, J., Seyler, F., Prigent, C., Rossow, W.B., Calmant, S., and Bonnet, M-P. (2011c). Satellite-based estimates of groundwater storage variations in large drainage basins with extensive floodplains. Remote Sensing of Environment, 115(6), pp. 1588-1594.

Fraser, R. H., Li, Z., Landry, R. (2000). SPOT VEGETATION for characterizing boreal forest fires, International Journal of Remote Sensing, 21, pp. 3525-3532.

Fu, Y., and Freymueller, J. T. (2012). Seasonal and long ‐ term vertical deformation in the Nepal Himalaya constrained by GPS and GRACE measurements. Journal of Geophysical Research: Solid Earth (1978‐2012), pp. 117-131.

Fuis, G.S. and Wald, L.A. (2003). Rupture in South-Central Alaska- The Denali Fault Earthquake of 2002. USGS Open-File Report 014-03. (http://pubs.usgs.gov/fs/2003/fs014-03/)

Gao, Y., and Chen, K. (2004). Performance analysis of precise point positioning using real-time orbit and clock products. Journal of Global Positioning System. 3(1-2), pp. 95-100.

Ge, M., Gendt, G., Rothacher, M., Shi, C., & Liu, J. (2008). Resolution of GPS carrier-phase ambiguities in precise point positioning (PPP) with daily observations. Journal of Geodesy 82(7), pp. 389-399.

Geirsson, H., Arnadottir, T., Volksen, C., Jiang, W., Sturkell, E., Villemin, T., Einarsson, P., Sigmundsson, F., and Stefansson, R. (2006) Current plate movements across the Mid-Atlantic Ridge determined from 5 years of continuous GPS measurements in Iceland. Journal of Geophysical Research 111, B09407.

Gruber, S., & Haeberli, W. (2007). Permafrost in steep bedrock slopes and its temperature ‐ related destabilization following climate change. Journal of Geophysical Research: Earth Surface (2003‐2012), 112 p.

Gomberg, J., Bodin, P., Savage, W.Z., Jackson, M.E. (1995). Land- slide faults and tectonic faults, analogs: the Slumgullion earth- flow, Colorado. Geology 23 (1), pp. 41–44.

Grapenthin, R., Sigmundsson, F., Geirsson, H., Arnadóttir, T., & Pinel, V. (2006). Icelandic rhythmics: Annual modulation of land elevation and plate spreading by snow load. Geophysical Research Letters 33(24), L24305.

Gurtner, W. (1994) RINEX: The receiver-independent exchange format, GPS World 5(7), pp. 48–52.

Haeberli, W., Muller, P., Alean, J., and Bösch, H. (1990). Glacier changes following the Little Ice Age. A survey of the international data base and its perspectives. D. Reidel Publishing Company, Dordrecht, Netherlands, pp. 77-101.

Haeussler, P. J., Bruhn, R. L. and Pratt, T. L. (2000). Potential seismic hazards and tectonics of upper Cook Inlet basin, Alaska, based on analysis of Pliocene and younger deformation, Geological Society of America Bulletin, 112, pp. 1414-1429.

Haeussler, P. J., & Saltus, R. W. (2004). 26 km of offset on the Lake Clark fault since Late Eocene time. US Geological Survey, pp. 5–8.

Harris, C., Davies, M.C.R. and Etzelmüller, B. (2001). The assessment of potential geotechnical hazards associated with mountain permafrost in a warming global climate. Permafrost and Periglacial Processes 12, pp. 145-156.

Heki, K. (2001). Seasonal modulation of interseismic strain build-up in northeastern Japan driven by snow loads. Science 293(5527), pp. 89-92.

Jadamec, M. A., Billen, M. I., and Roeske, S. M. (2013). Three-dimensional numerical models of flat slab subduction and the Denali fault driving deformation in south-central Alaska. Earth and Planetary Science Letters, 376, pp. 29–42.

Jaldehag, K.R.T., Johansson, J.M., Davis, J.L., and Elosegui, P. (1996). Geodesy using the Swedish permanent GPS network: effects of snow accumulation on estimates of site positions. Geophysical Research Letters 23(13), pp. 1601–1604.

Jensen, J. R. (2006). Remote Sensing of the Environment: An Earth Resource Perspective (2nd edition): Prentice-Hall, Inc., New Jersey.

Jorgenson, M.T., Shur, Y., and Osterkamp, T.E. (2008a). Thermokarst in Alaska. 9th International Conference on Permafrost, Univ. Alaska Fairbanks, pp. 869-876.

Kalbas, J. L., Freed, A. M. and Ridgway, K. D. (2008). Contemporary fault mechanics in southern Alaska, AGU, Washington, D. C., pp. 321–336.

Kouba, J., and Springer, T. (2001). New IGS station and satellite clock combination. GPS Solution 4(4), pp. 31–36.

Kouba, J., and Heroux, P. (2001). GPS precise point positioning using IGS Orbit products, GPS Solutions 5(2), pp. 12-28.

Lantuit, H., Fritz, M., Krautblatter, M., Angelopoulos, M. and Pollard, W. H. (2013), What triggers retrogressive thaw slumps in the Arctic coastal zone? , 9th Arctic Net Annual Scientific Meeting (ASM2013), Halifax, Canada, 9 December 2013 - 13 December 2013.

Larsen, C. F., Motyka, R. J., Arendt, A. A., Echelmeyer, K. A., and Geissler, P. E. (2007). Glacier changes in southeast Alaska and northwest British Columbia and contribution to sea level rise. Journal of Geophysical Research: Earth Surface, pp. 112

Larson, K.M. (2013). A methodology to eliminate snow- and ice-contaminated solutions from GPS coordinate time series. Journal of Geophysical Research: Solid Earth 118, pp. 1–8.

Lipovsky, P. (2015). Permafrost-related landslides in south and central Yukon. Yukon Geological Survey. Retrieved 04 20, 2015, from http://www.usask.ca/ip3/download/ws3/presentations/13d_lipovsky.pdf

Lisowski, M., Dzurisin, D., Denlinger, R., Iwatsubo, E. (2008). Analysis of GPS-measured deformation associated with the 2004–2006 dome building eruption of Mount St. Helens, Washington, U.S. Geological Survey professional paper, 1750, pp. 301–333.

Matmon, A., Schwartz, D.P., Haeussler, P.J., Finkel, R., Lienkaemper, J.J., Stenner, H.D. and Dawson, T.E. (2006). Denali fault slip rates and Holocene-late Pleistocene kinematics of central Alaska, Geology, 34, pp. 645-648.

Matsuzaka, S. (2014). Geodesy and Geodetics. Retrieved 08 18, 2014, from http://ggim.un.org/docs/meetings/Hangzhou%20Forum/session%203/Geodesy%20and%20Geodetic%20reference%20system.pdf

McRoberts, E. C. (1978). Slope stability in cold regions. Geotechnical Engineering for Cold Regions. New York, NY: McGraw-Hill, pp. 363-404

McRoberts, E. C. and Morgenstern, N. R. (1974a). Stability of slopes in frozen soil, Mackenzie Valley, N.W.T. Canadian Geotechnical Journal 11(4), pp. 554–573.

McRoberts, E. C. and Morgenstern, N. R. (1974b) The stability of thawing slopes. Canadian Geotechnical Journal 11(4), pp. 447–469.

Misra, P. and Enge, P. (2006). Global Positioning System: Signals, Measurements, and Performance, Ganga-Jamuna Press, Lincoln, Mass.

National Geodetic Survey (2014). NOAA's National Ocean Service. Retrieved 09 12, 2014. From http://www.ngs.noaa.gov

NSIDC (2015). National Snow & Ice Data Center. Retrieved 05 02, 2015. From https://nsidc.org/cryosphere/glossary ww.ngs.noaa.gov

The Nevada Geodetic Laboratory (2014). GPS Network Map. Retrieved 2, 1, 2014. From http://geodesy.unr.edu/

Pearson, C., McCaffrey, R., Elliott, J. L., and Snay, R. (2010). HTDP 3.0: Software for Coping with the Coordinate Changes Associated with Crustal Motion. Journal of Surveying Engineering, 136(2), pp. 80-90.

Plate Boundary Observatory (2014).UNAVCO PBO site. Retrieved 10 8, 2014, from http://pbo.unavco.org/

Plafker, G. (1969). Tectonics of the March 27, 1964, Alaska earthquake, U.S. Geological Survey professional paper 543-I, 74 p.

Plafker, G., Kachadoorian, R. Eckel, E. B. and Mayo L. R. (1969), Effects of the earthquake of March 27, 1964 on various communities, U.S. Geological Survey professional paper 542-G, pp. 1–50.

Plafker, G., Hudson, T., Bruns, T., and Rubin, M. (1978). Late Quaternary offsets along the Fairweather fault and crustal plate interactions in southern Alaska. Canadian Journal of Earth Sciences 15, pp. 805–816.

Plafker, G., Gilpin, L. M. and Lahr, J. C. (1994). Geology of the southern Alaska margin, The Geology of North America, Vol. G-1, Geological Society of America, Boulder, Colorado, pp. 389 –449.

Reed B.L., and Lanphere, M.A. (1973). Alaska-Aleutian Range batholith; geochronology, chemistry, and relation to circum-Pacific plutonism, Geological Society of America Bulletin 84, pp. 2593-2609.

Richter, D. H., & Matson, N. A. (1971). Quaternary faulting in the eastern Alaska Range, Geological Society of America Bulletin, 82(6), pp. 1529–1539.

Rogan, J. and Yool S. R. (2001). Mapping fire-induced vegetation depletion in the Peloncillo Mountains, Arizona and New Mexico. International Journal of Remote Sensing 22, pp. 3101-3121.

Sauber, J. M., & Molnia, B. F. (2004). Glacier ice mass fluctuations and fault instability in tectonically active Southern Alaska. Global and Planetary Change 42(1-4), pp. 279–293.

Siegert, F. and Hoffman, A. A. (2000). The 1998 forest fires in East Kalimantan (Indonesia): A quantitative evaluation using high resolution, multitemporal ERS-2 SAR images and NOAAAVHRR hotspot data, Remote Sensing Environment 72, pp. 64-67.

Silberling, N.J., Jones, D.L., Monger, J.W.H., Coney, P.J., Berg, H.C., and Plafker, G. (1994). Lithotectonic terrane map of Alaska and adjacent parts of Canada, the Geology of North America: The Geological Society of America, plate 3, 1 sheet, scale 1:7,500.000.

Snay, R.A. (1999). Using HTDP software to transform spatial coordinates across time and between reference frames. Surveying and Land Information Science 59(1), pp. 15-25.

Sousanes, P.J. (2012). Snowpack monitoring, 2008-2009 annual summary: Central Alaska Network. Natural Resource Data Series NPS/CAKN/NRDS—2012/253. National Park Service, Fort Collins, Colorado.

Soler, T., Johnson, R. E., Thormahlen, L. F., and Foote, R. H. (2001). APPLICATION CHALLENGE-Parting the Waters-An international survey team combined real-time and static differential GPS data to map coastal boundaries between the United States and Mexico. Four. GPS World 12(5), pp. 28-31.

Soler, T., and Marshall, J. (2003). A Note on frame transformations with applications to geodetic datums. GPS Solutions 7(1), pp. 23-32.

Soler, T., and Snay, R. A. (2004). Transforming positions and velocities between the International Terrestrial Reference Frame of 2000 and North American Datum of 1983. Journal of Surveying Engineering 130(2), pp. 49-55.

State of Alaska (2014). Alaska Earthquake Hazard Safety Division Earthquake Risk in Alaska. Division of Geological and Geophysical Surveys. Retrieved on 10 15, 2014, from http://www.dggs.dnr.state.ak.us/seismic_hazards_earthquake_risk.htm#AlaskaEarthquakeStats

Suito, H., and Freymueller, J.T. (2009). A viscoelastic and afterslip postseismic deformation model for the 1964 Alaska earthquake. Journal of Geophysical Research 114, B11404

Teferle F.N., Orliac E.J., and Bingley R.M. (2007). An assessment of Bernese GPS software precise point positioning using IGS final products for global site velocities, GPS Solution 11, pp. 205–213.

Trop, J. M., and Ridgway, K. D. (2007). Mesozoic and Cenozoic tectonic growth of southern Alaska: A sedimentary basin perspective. Geological Society of America Special Papers, 431, pp. 55-94.

U.S. Geological Survey (2014). The 2002 Denali Fault earthquake. Retrieved 09 30,2014, from http://earthquake.usgs.gov/earthquakes/eqinthenews/2002/uslbbl/

U.S. Geological Survey (2004). Landslide types and Processes. Retrieved on 03 18, 2015, from http://pubs.usgs.gov/fs/2004/3072/fs-2004-3072.html

Van Dam, T. M., Wahr, J., Milly, P.C.D., Shmakin, A.B., Blewitt, G., Lavallee, D., Larson, K.M. (2001). Crustal displacements due to continental water loading. Geophysical Research Letters 28, pp. 651– 654.

Vohora, V.K. and Donoghue, S.L. (2004) Application of remote sensing data to landslide mapping in Hong Kong. Proceedings of the XXth ISPRS Congress, Istanbul, Turkey. Retreived on 3 20, 2015, from http://www.isprs.org/istanbul2004/comm4/papers/398.pdf

Wang, G., Soler, T. (2012). OPUS for horizontal subcentimeter-accuracy landslide monitoring: case study in the Puerto Rico and Virgin Islands region. J Surv Eng 133(3), pp. 143-153.

Wang, G. Q. (2013). Millimeter-accuracy GPS landslide monitoring using Precise Point Positioning with Single Receiver Phase Ambiguity (PPP-SRPA) resolution: a case study in Puerto Rico. Journal of Geodetic Science 3(1), pp. 22-31.

Wang, G., Yu, J., Ortega, J., Saenz, G., Burrough, T., and Neill, R. (2013b). A Stable Reference Frame for Ground 601 Deformation Study in the Houston Metropolitan Area, Texas. Journal of Geodetic Science 3(3), pp. 188-202.

Wang, G., Kearns, T.J., Yu, J., and Saenz, G. (2014). A stable reference frame for landslide monitoring using GPS in the Puerto Rico and Virgin Islands region. Landslides 11(1), pp. 119-129.

Wang, G., Bao, Y., Cuddus, Y., Jia, X., Serna Jr, J., & Jing, Q. (2015). A methodology to derive precise landslide displacement time series from continuous GPS observations in tectonically active and cold regions: a case study in Alaska. Natural Hazards, pp. 1-23

Watson, K.M., Bock, Y., Sandwell, D.T. (2002). Satellite interferometric observations of displacements associated with seasonal groundwater in the Los Angeles Basin. Journal of Geophysical Research 107(B4), pp. 2074.

Webb, F.H., Bursik, M., Dixon, T., Farina, F., Marshall, G., Stein, R.S. (1995). Inflation of Long Valley Caldera from one year of continuous GPS observations. Geophysical Research Letters 22(3), pp. 195–198.

Webb, F. H., & Zumberge, J. F. (1997). An Introduction to GIPSY/OASIS. JPL Publication D-11088. Jet Propulsion Laboratory, Pasadena, CA.

West, M. E., Haeussler, P. J., Ruppert, N. A., and Freymueller, J. T. (2014). Why the 1964 Great Alaska Earthquake Matters 50 Years Later. Seismological Research Letters 85(2), pp. 245-251.

Zumberge, J.F., Heflin, M.B., Jefferson, D.C., Watkins, M.M., and Webb, F.H. (1997). Precise point positioning for the efficient and robust analysis of GPS data from large networks. Journal of Geophysical Research 102, pp. 5005–5018.

Zweck, C., and Freymueller, J.T., Cohen, S.C. (2002). Elastic dislocation modeling of the postseismic response to the 1964 Alaska Earthquake. Journal of Geophysical Research 107(B4), pp. 2064

Zweck, C., and Freymueller, J.T., Cohen, S.C. (2002). Elastic dislocation modeling of the postseismic response to the 1964 Alaska Earthquake. Journal of Geophysical Research 107(B4), pp. 2064

APPENDIXES A- SOUTH-CENTRAL ALASKA TECTONIC MAPS

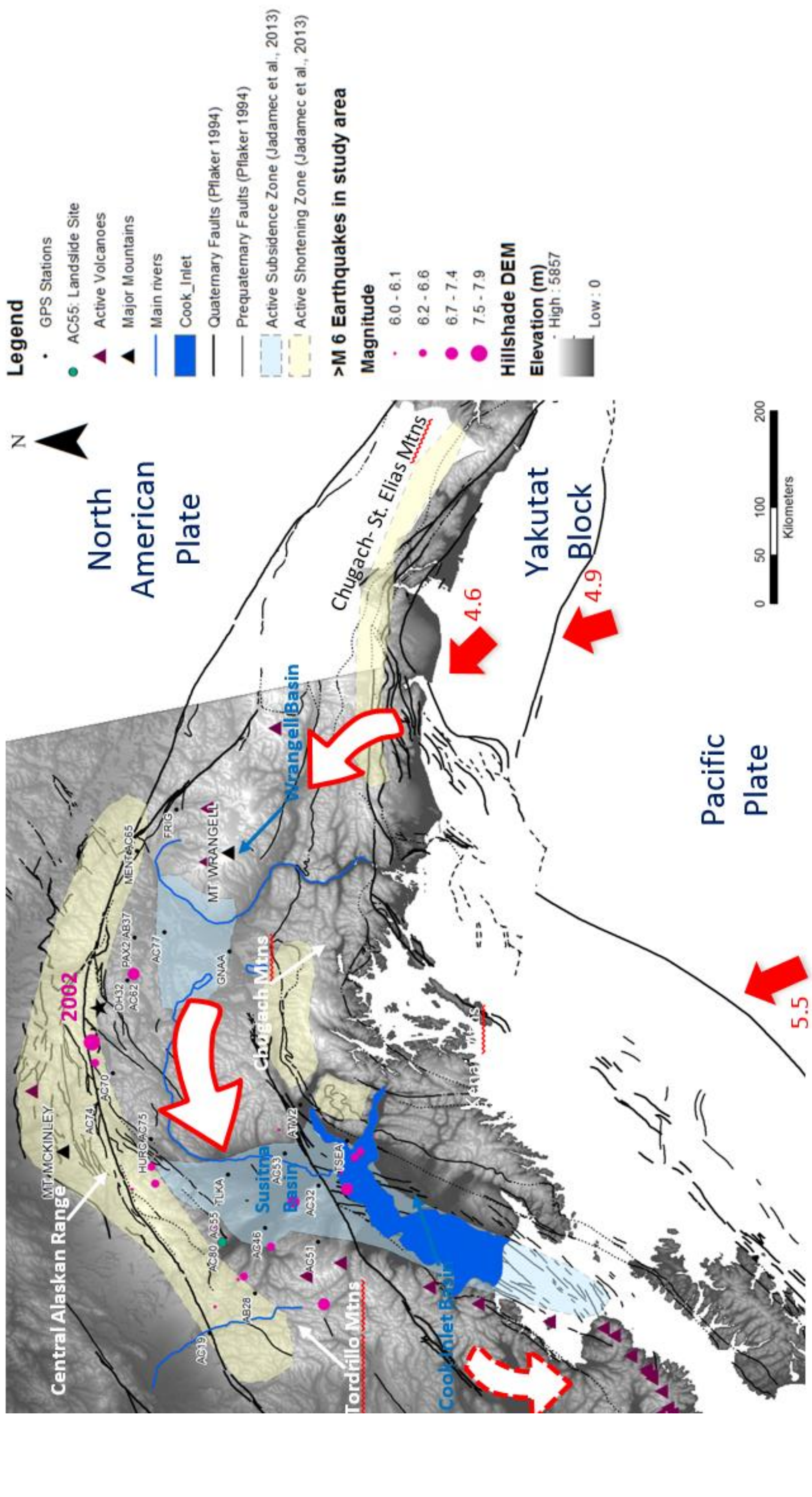

Appendix A.1: Current Tectonic Setting. Locations of active uplift and subsidence in south-central Alaska. The plate motion and rates (cm/year) are indicated by filled red arrows, hollow red arrow show lateral movement of the broad Wrangell block motion as a result of the Denali fault (modified from Jadamec et al., 2013). The black star is at the M7.9 Denali earthquake epicenter.

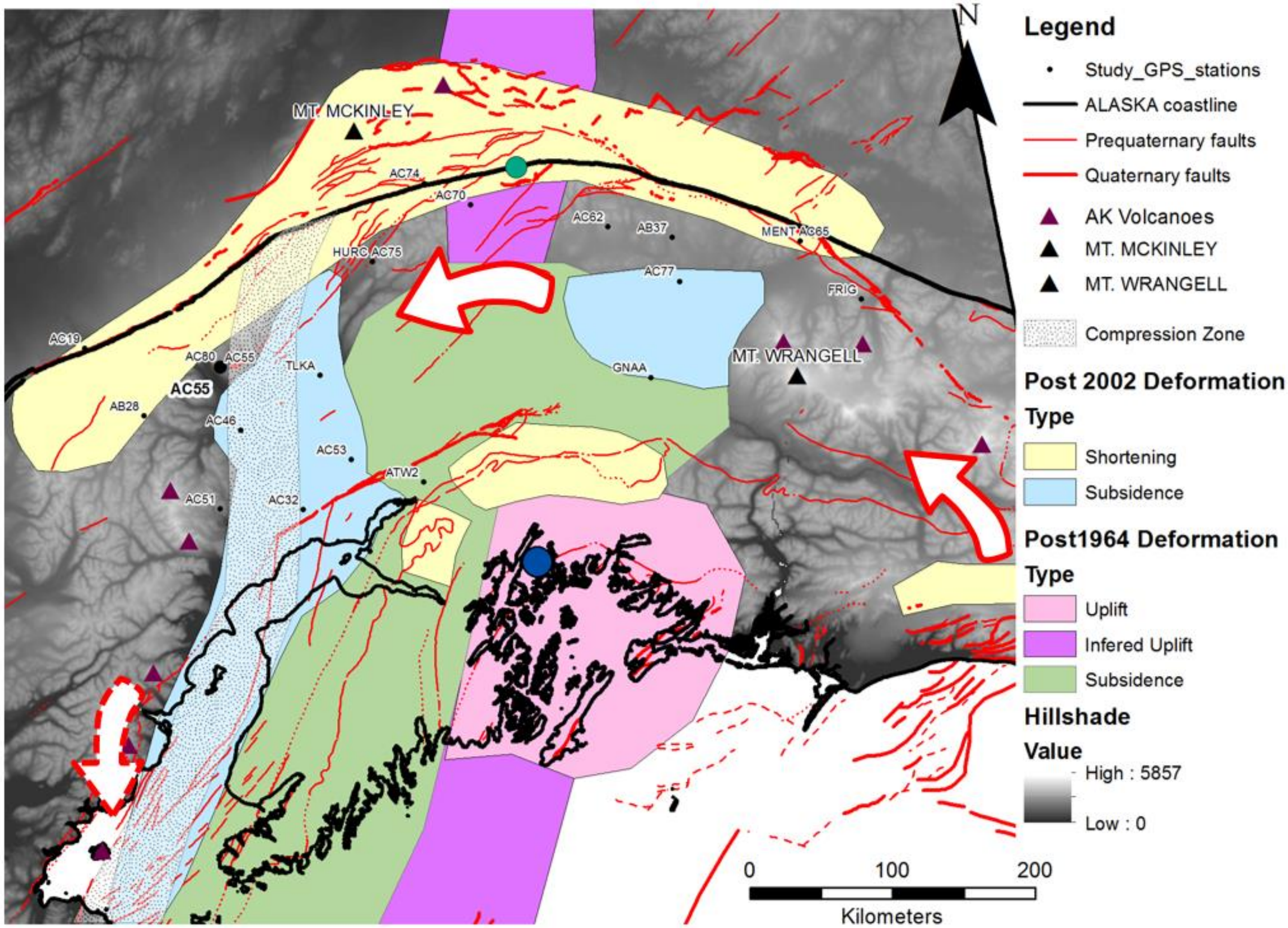

Appendix A.2: Tectonic uplift and subsidence in south-central Alaska after the 1964 earthquake (modified from Pflaker, 1964) and the 2002 Denali Earthquake (modified from Jadamec et al., 2013). Red arrow show lateral movement of the broad Wrangell block. Green dot represent the M7.9 Denali earthquake epicenter and the blue dot is the M9.2 Great Alaskan earthquake epicenter. The black dotted ribbon represents a zone of compression that is created between the Wrangell Subplate and the North American Plate. The postseismic deformation from both events show a subsidence concentration in the south central basin.

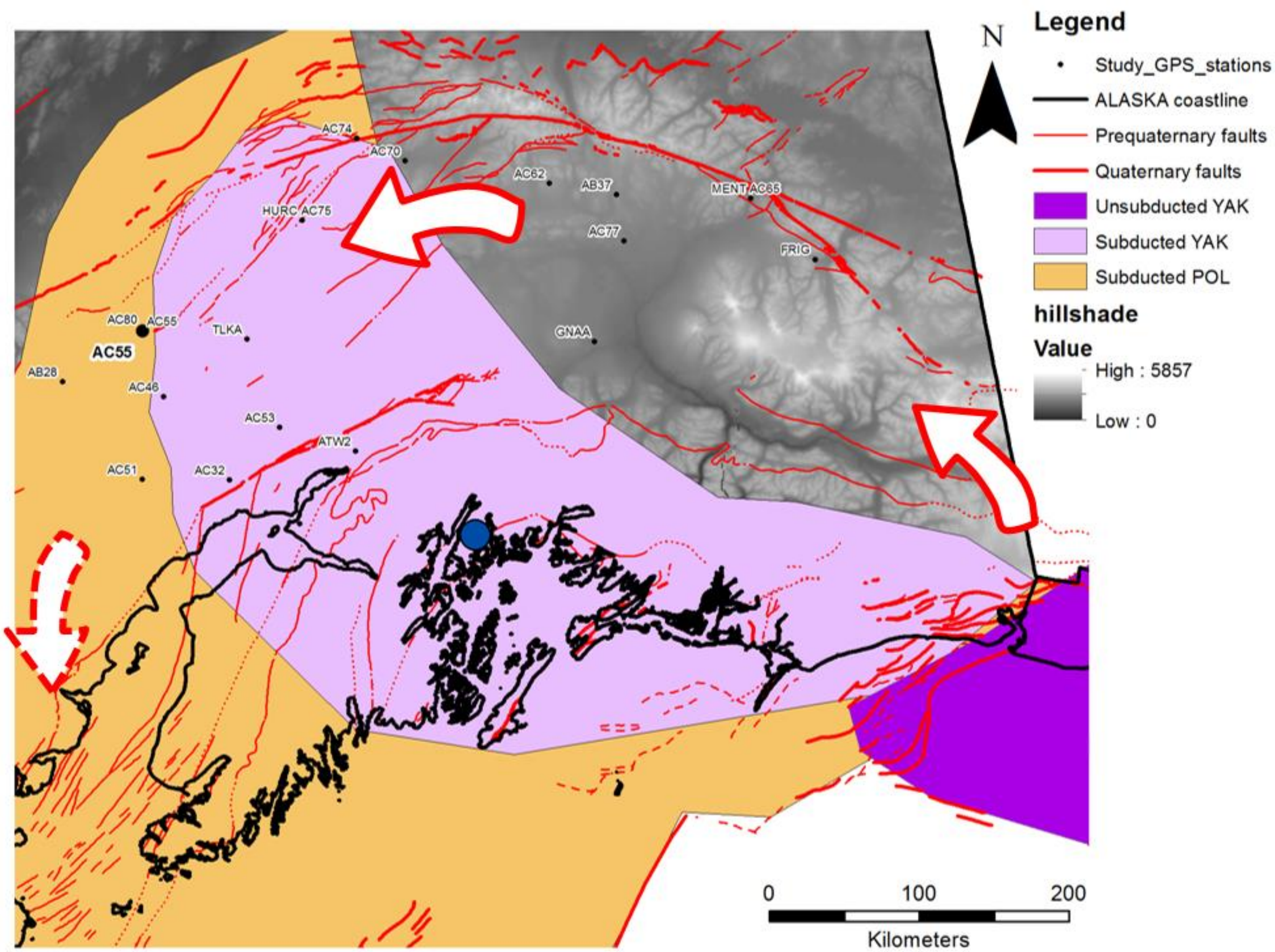

Appendix A.3: Tectonic map of southern Alaska. Examines the dominant factor in the subsidence and uplift zones, which is the long term trends of the Yakutat terrane (Fuis et al., 2008). Colors—subducted (lighter) and unsubducted (darker) plates and/or terranes. Yellow- POL, Pacific oceanic lithosphere. Blue dot—epicenter of M 9.2 1964 earthquake, faults digitized from Pflaker, 1994. The rate and orientation of tectonic stress and strain is primarily due to subduction of the Pacific plate and collision of the Yakutat terrane with interior Alaska (Sauber et al., 2004) (Modified from Fuis et al., 2008).

APPENDIXES B- GPS POSITIONAL TIME SERIES

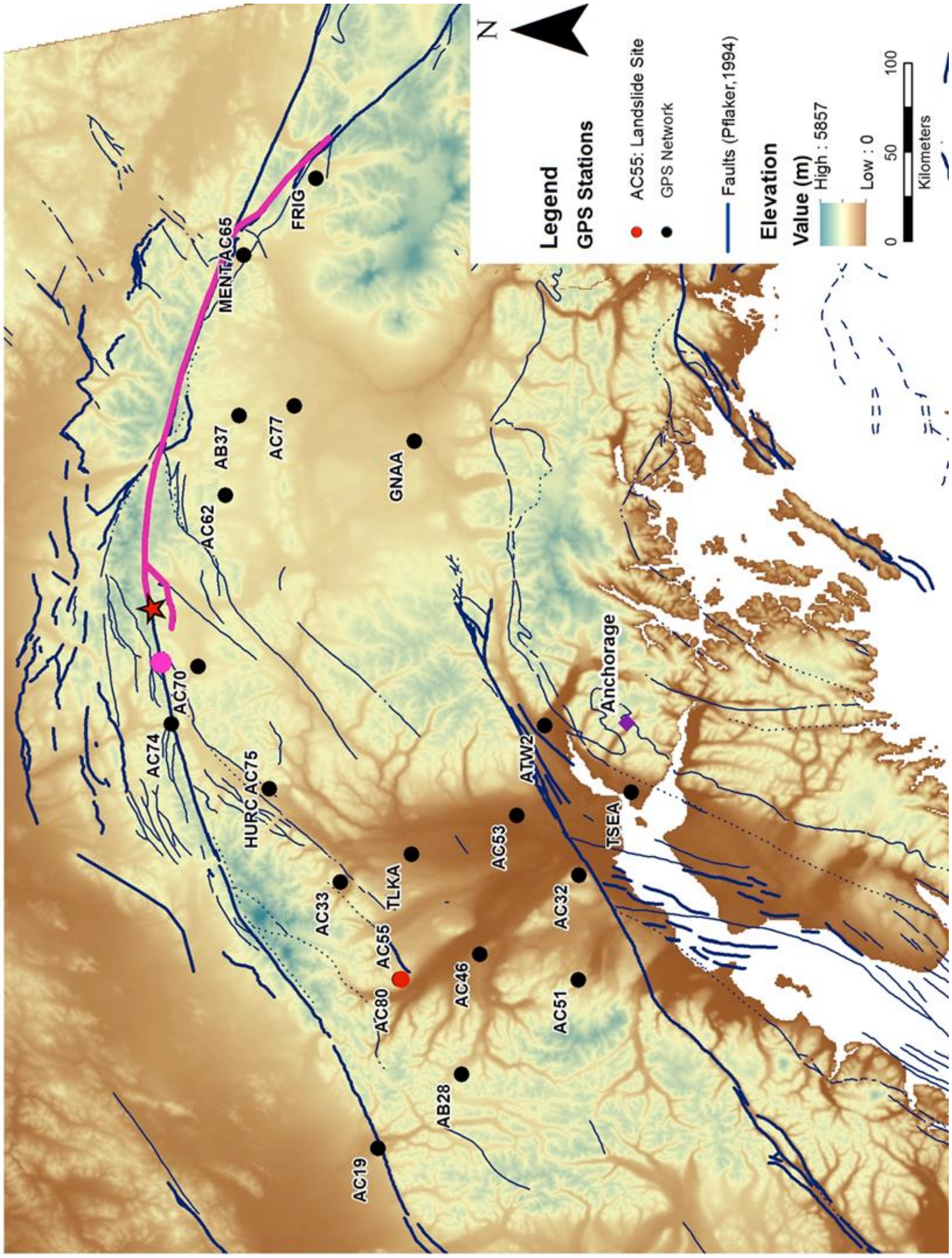

Locator Map. Shows the location of the landslide site (red dot, AC55) and all GPS stations in the study

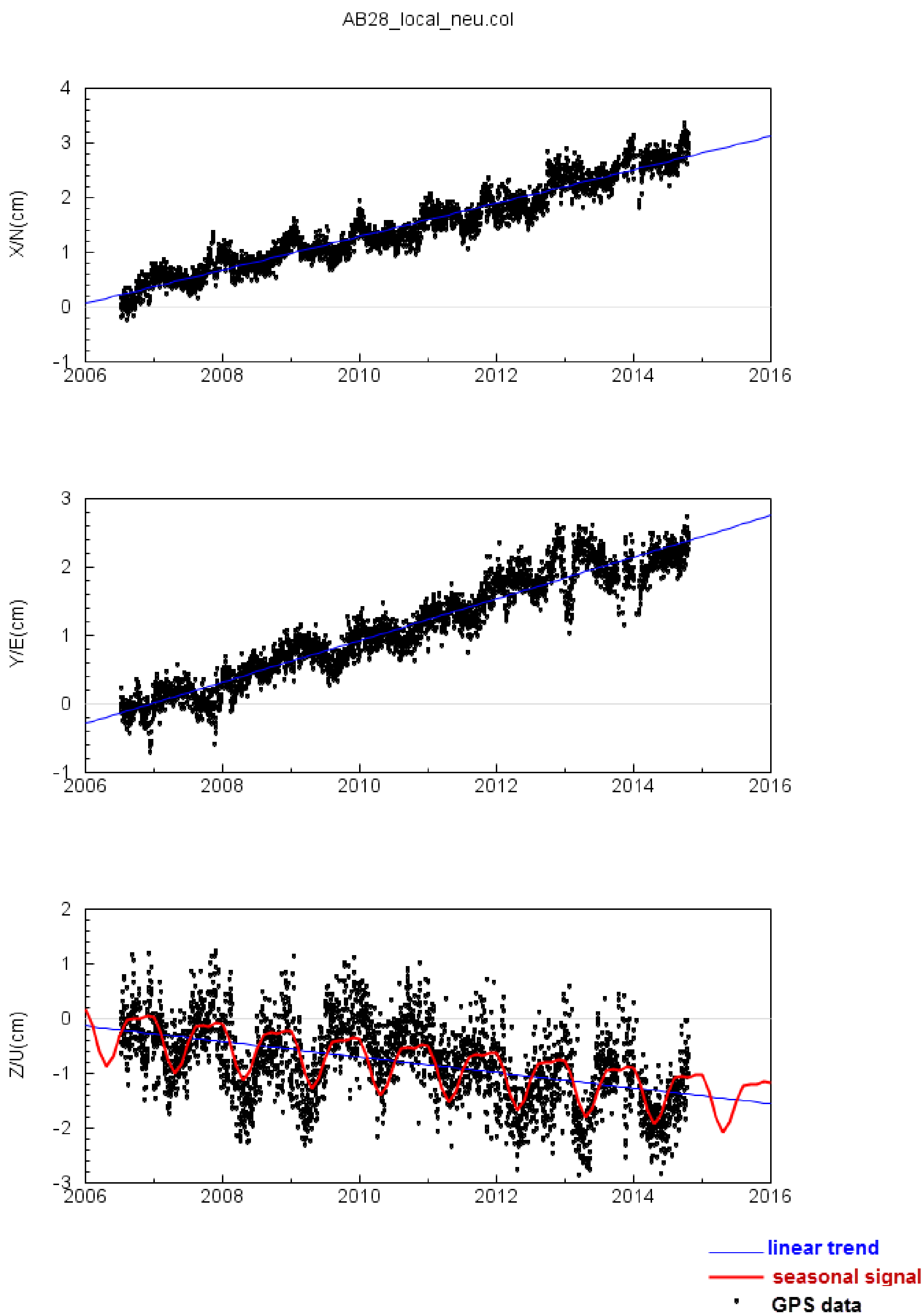

GPS three-component (X/N, Y/E, Z/U) positional time series. Raw GPS data that has been transformed to the local reference frame. No outliers have been removed. (North =positive X/N, South= negative X/N, East= positive Y/E, West= negative Y/E, rebound =positive Z/U, subsidence= negative Z/U).

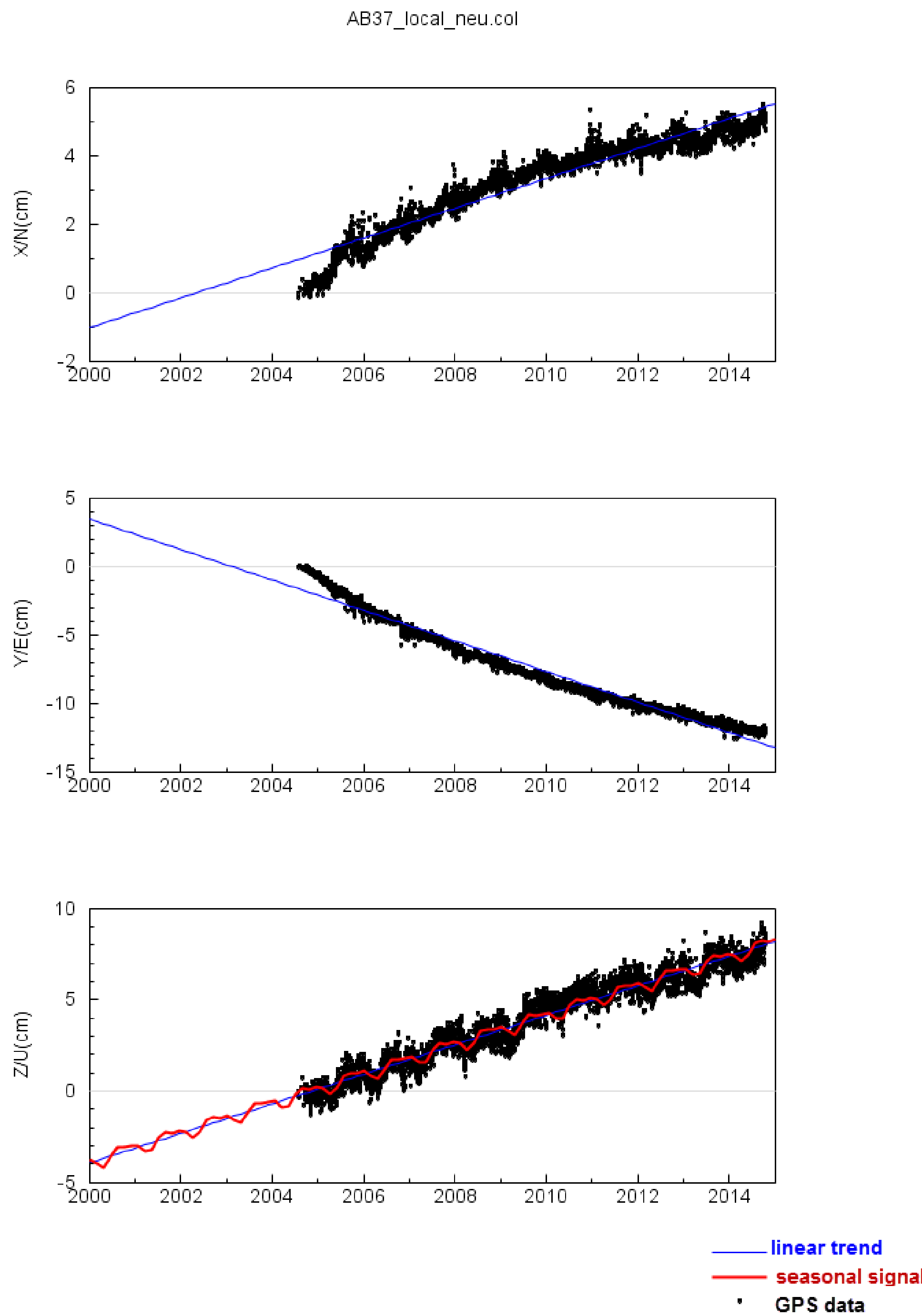

GPS three-component (X/N, Y/E, Z/U) positional time series. Raw GPS data that has been transformed to the local reference frame. No outliers have been removed. (North =positive X/N, South= negative X/N, East= positive Y/E, West= negative Y/E, rebound =positive Z/U, subsidence= negative Z/U).

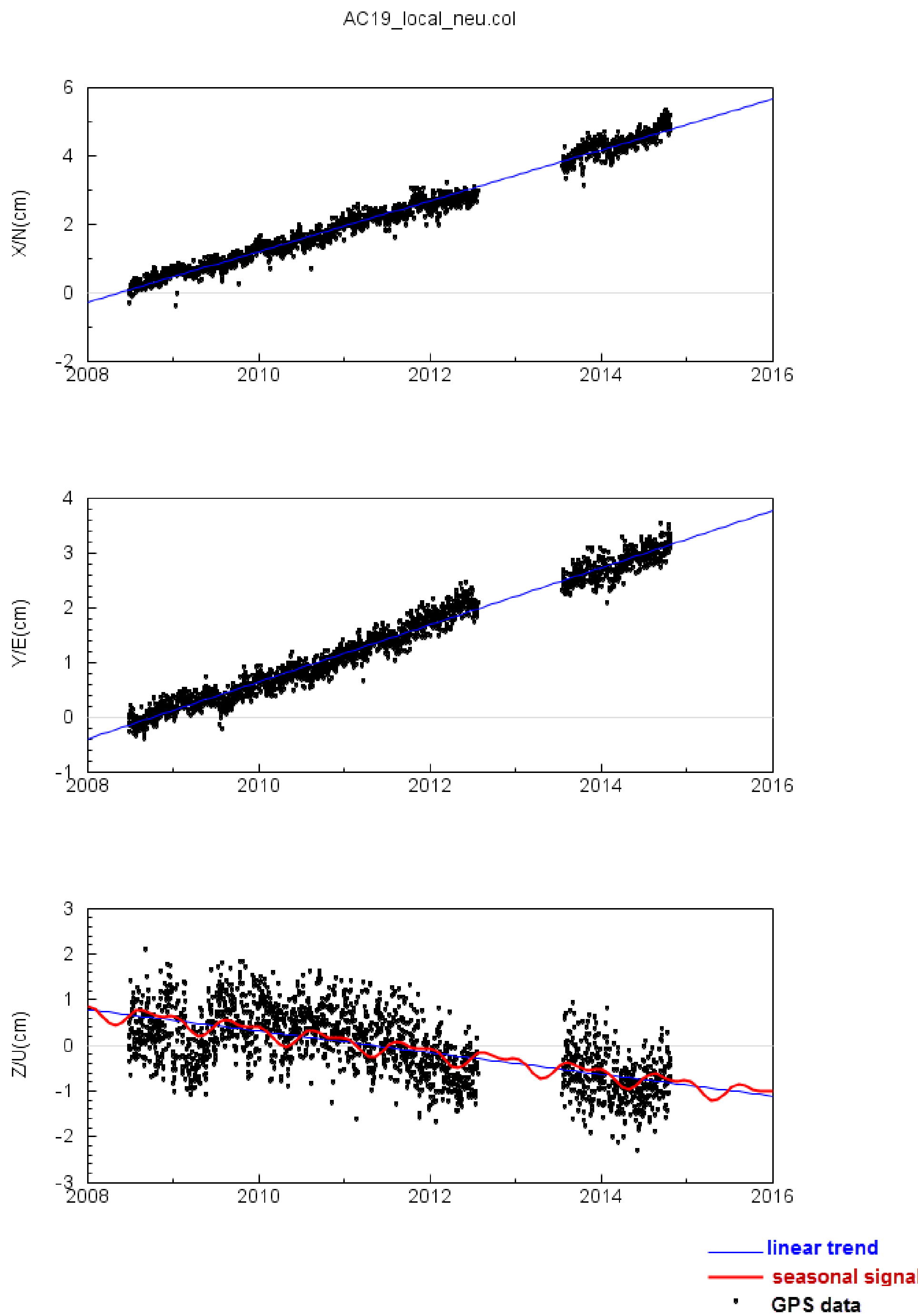

GPS three-component (X/N, Y/E, Z/U) positional time series. Raw GPS data that has been transformed to the local reference frame. No outliers have been removed. (North =positive X/N, South= negative X/N, East= positive Y/E, West= negative Y/E, rebound =positive Z/U, subsidence= negative Z/U).

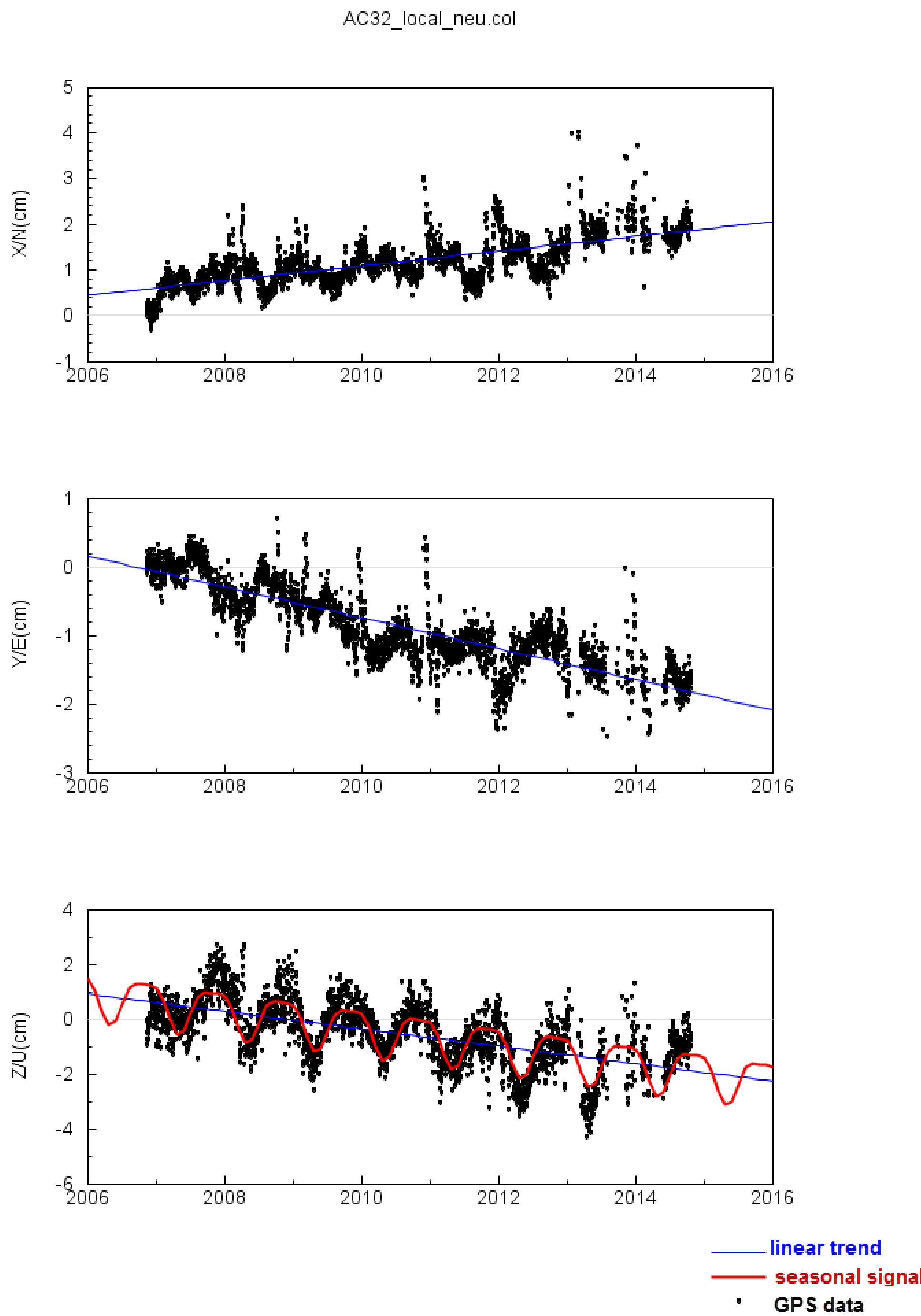

GPS three-component (X/N, Y/E, Z/U) positional time series. Raw GPS data that has been transformed to the local reference frame. No outliers have been removed. (North =positive X/N, South= negative X/N, East= positive Y/E, West= negative Y/E, rebound =positive Z/U, subsidence= negative Z/U).

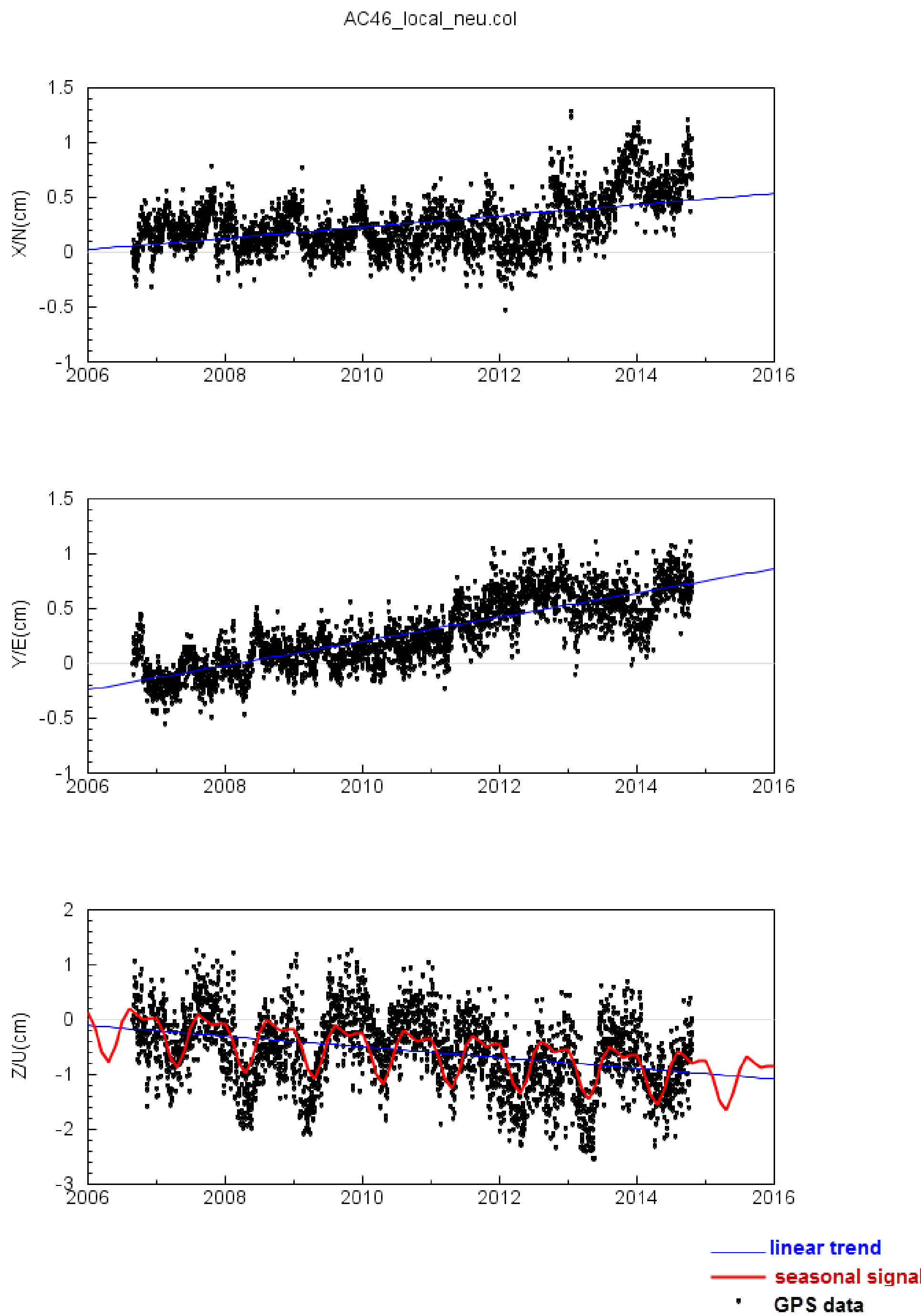

GPS three-component (X/N, Y/E, Z/U) positional time series. Raw GPS data that has been transformed to the local reference frame. No outliers have been removed. (North =positive X/N, South= negative X/N, East= positive Y/E, West= negative Y/E, rebound =positive Z/U, subsidence= negative Z/U).

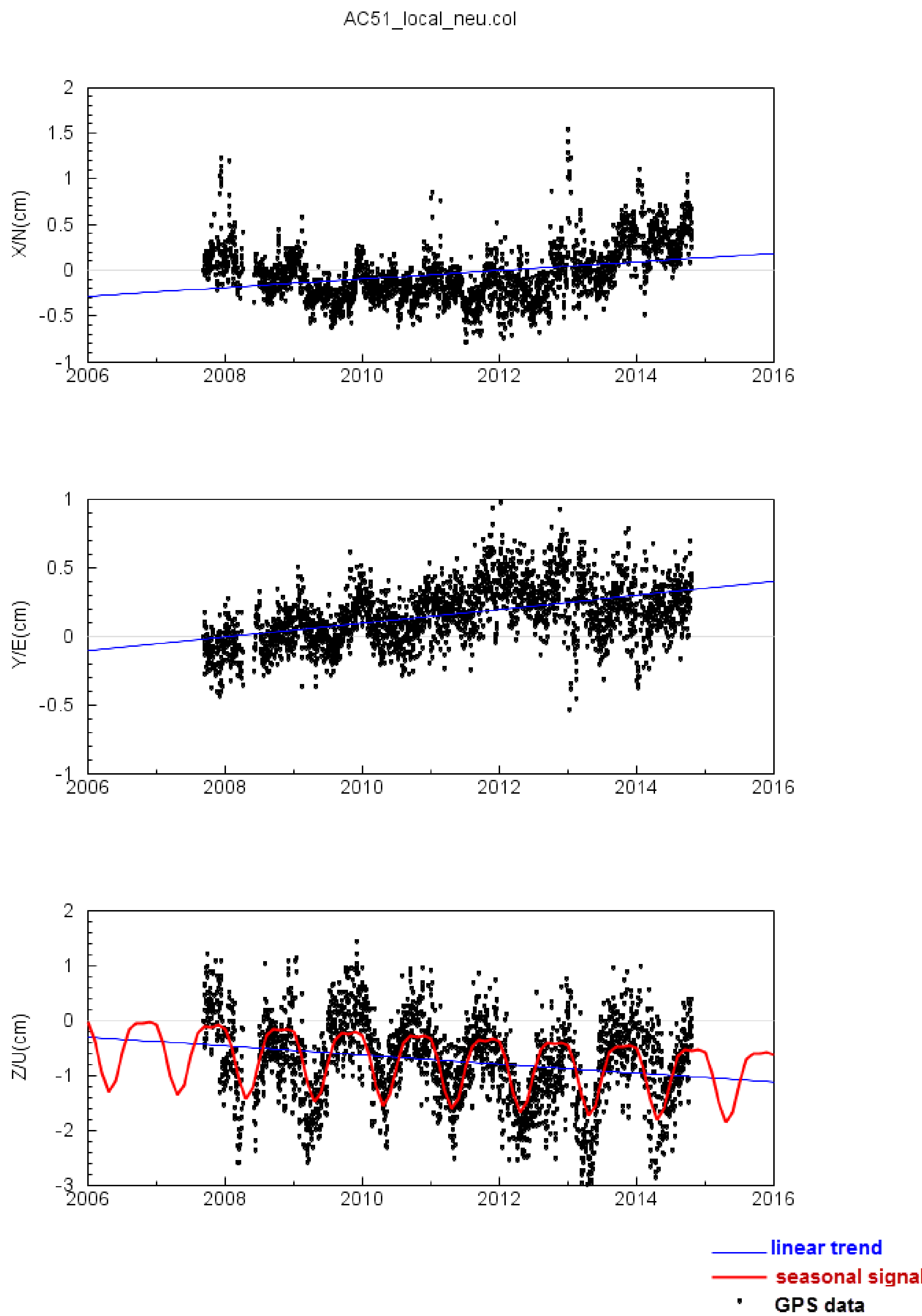

GPS three-component (X/N, Y/E, Z/U) positional time series. Raw GPS data that has been transformed to the local reference frame. No outliers have been removed. (North =positive X/N, South= negative X/N, East= positive Y/E, West= negative Y/E, rebound =positive Z/U, subsidence= negative Z/U).

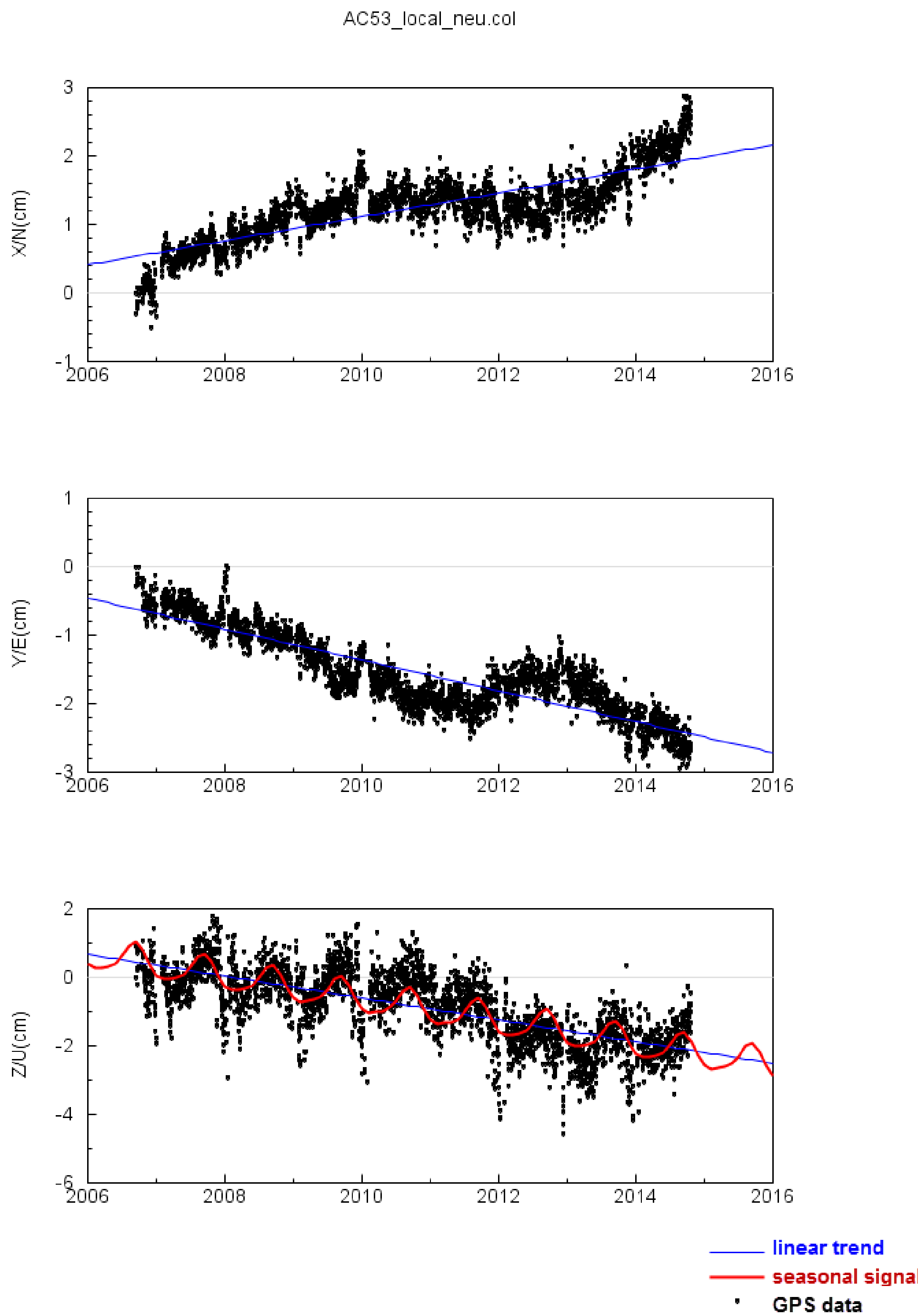

GPS three-component (X/N, Y/E, Z/U) positional time series. Raw GPS data that has been transformed to the local reference frame. No outliers have been removed. (North =positive X/N, South= negative X/N, East= positive Y/E, West= negative Y/E, rebound =positive Z/U, subsidence= negative Z/U).

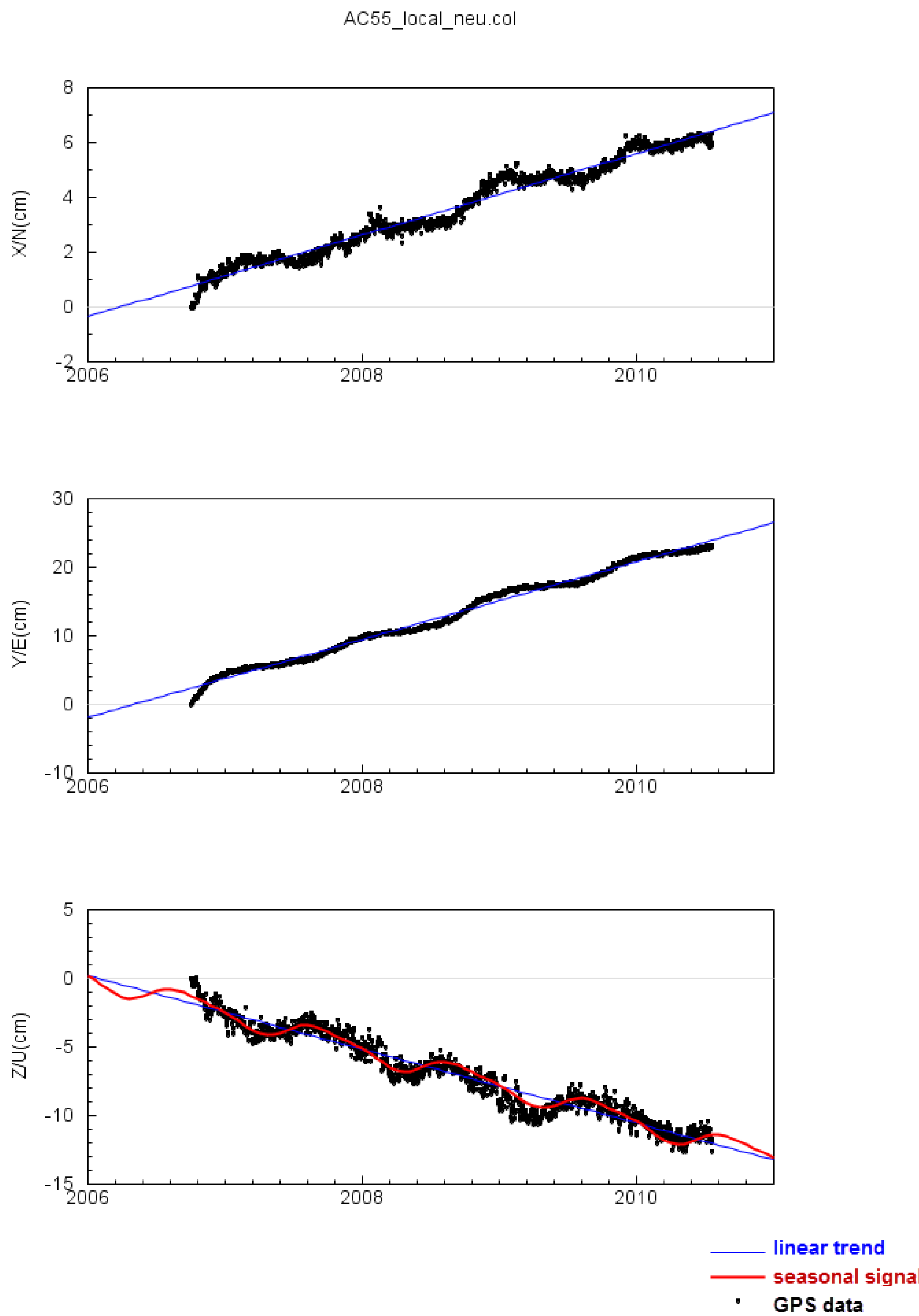

GPS three-component (X/N, Y/E, Z/U) positional time series. Raw GPS data that has been transformed to the local reference frame. No outliers have been removed. (North =positive X/N, South= negative X/N, East= positive Y/E, West= negative Y/E, rebound =positive Z/U, subsidence= negative Z/U).

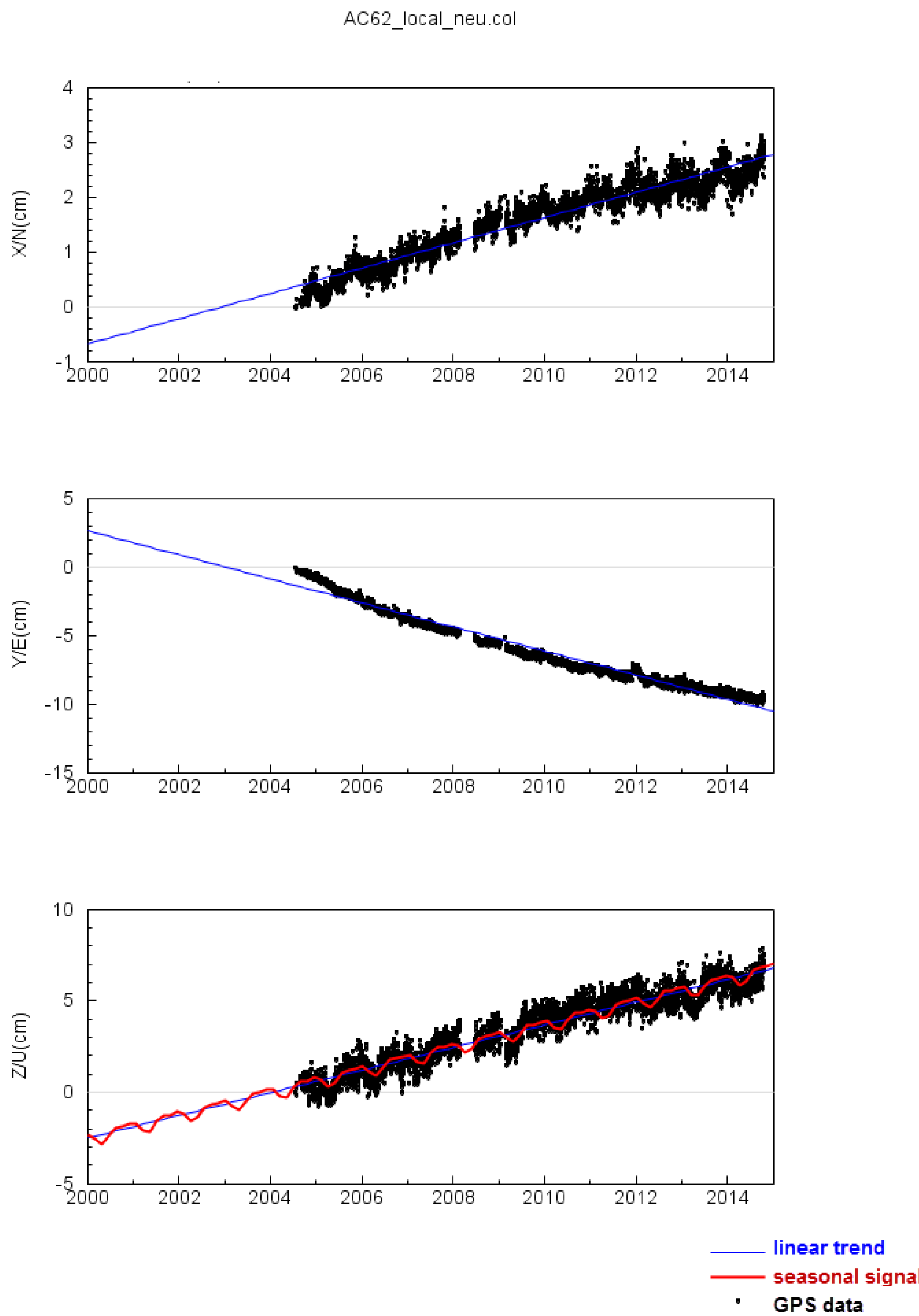

GPS three-component (X/N, Y/E, Z/U) positional time series. Raw GPS data that has been transformed to the local reference frame. No outliers have been removed. (North =positive X/N, South= negative X/N, East= positive Y/E, West= negative Y/E, rebound =positive Z/U, subsidence= negative Z/U).

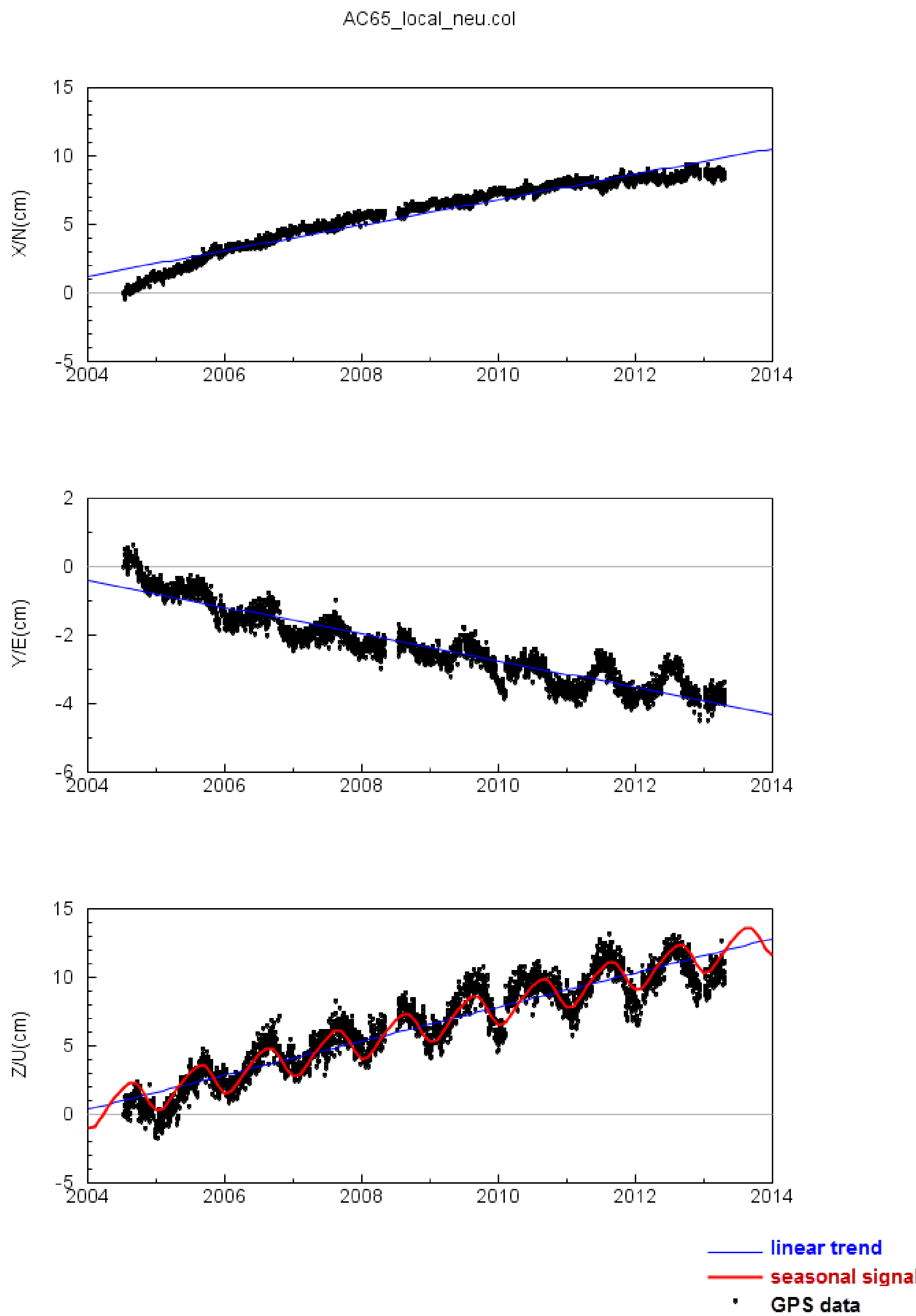

GPS three-component (X/N, Y/E, Z/U) positional time series. Raw GPS data that has been transformed to the local reference frame. No outliers have been removed. (North =positive X/N, South= negative X/N, East= positive Y/E, West= negative Y/E, rebound =positive Z/U, subsidence= negative Z/U).

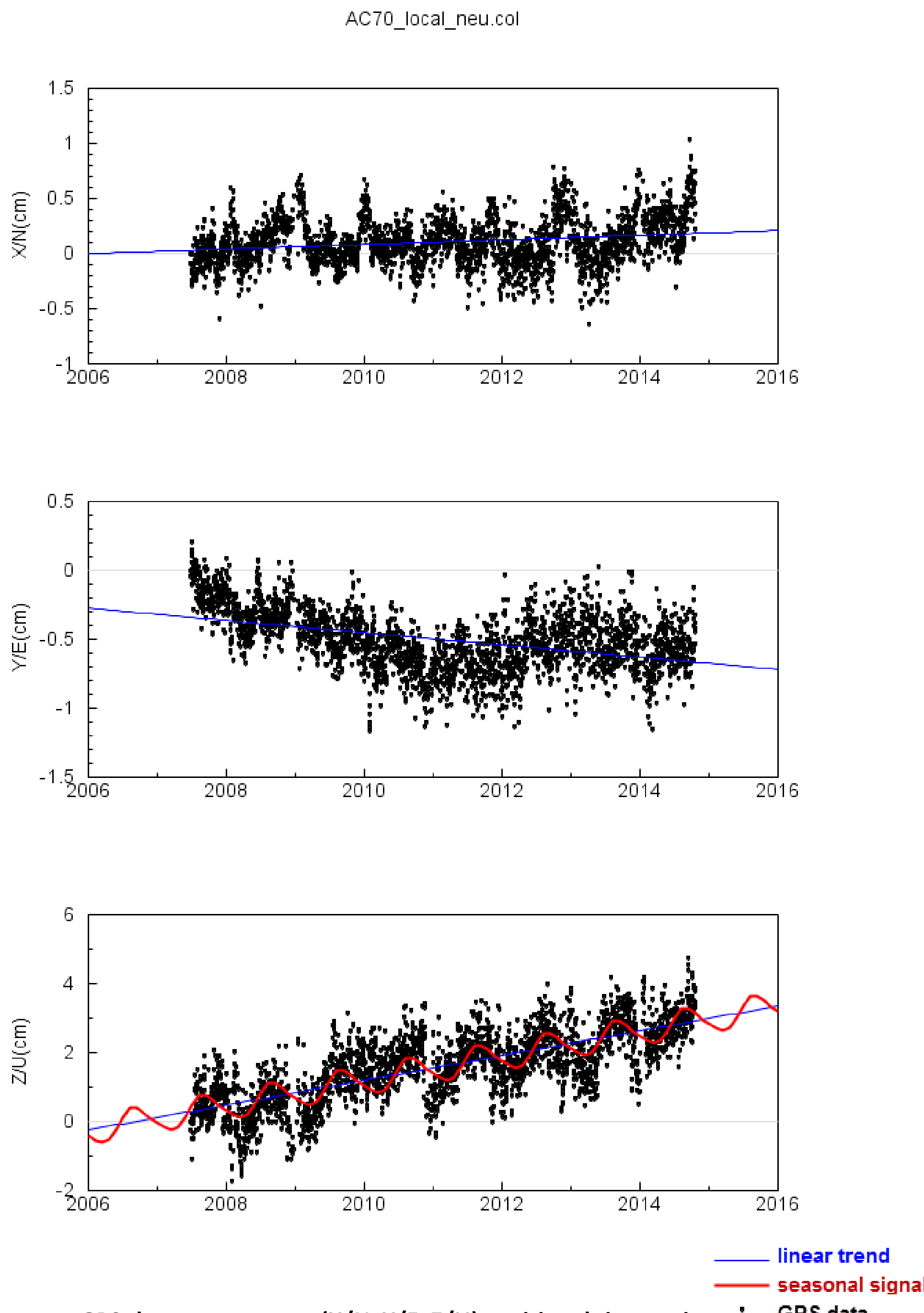

GPS three-component (X/N, Y/E, Z/U) positional time series. Raw GPS data that has been transformed to the local reference frame. No outliers have been removed. (North =positive X/N, South= negative X/N, East= positive Y/E, West= negative Y/E, rebound =positive Z/U, subsidence= negative Z/U).

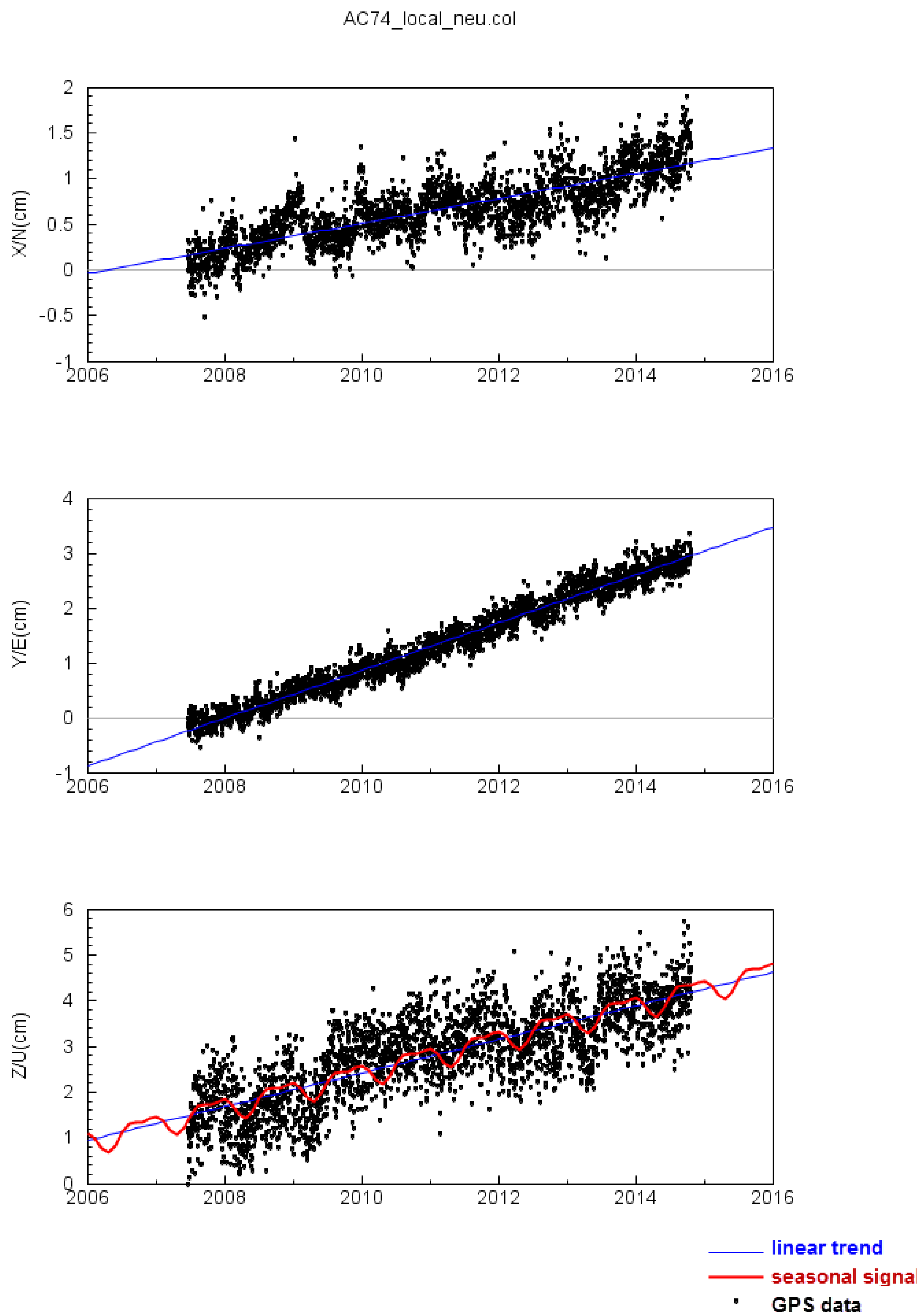

GPS three-component (X/N, Y/E, Z/U) positional time series. Raw GPS data that has been transformed to the local reference frame. No outliers have been removed. (North =positive X/N, South= negative X/N, East= positive Y/E, West= negative Y/E, rebound =positive Z/U, subsidence= negative Z/U).

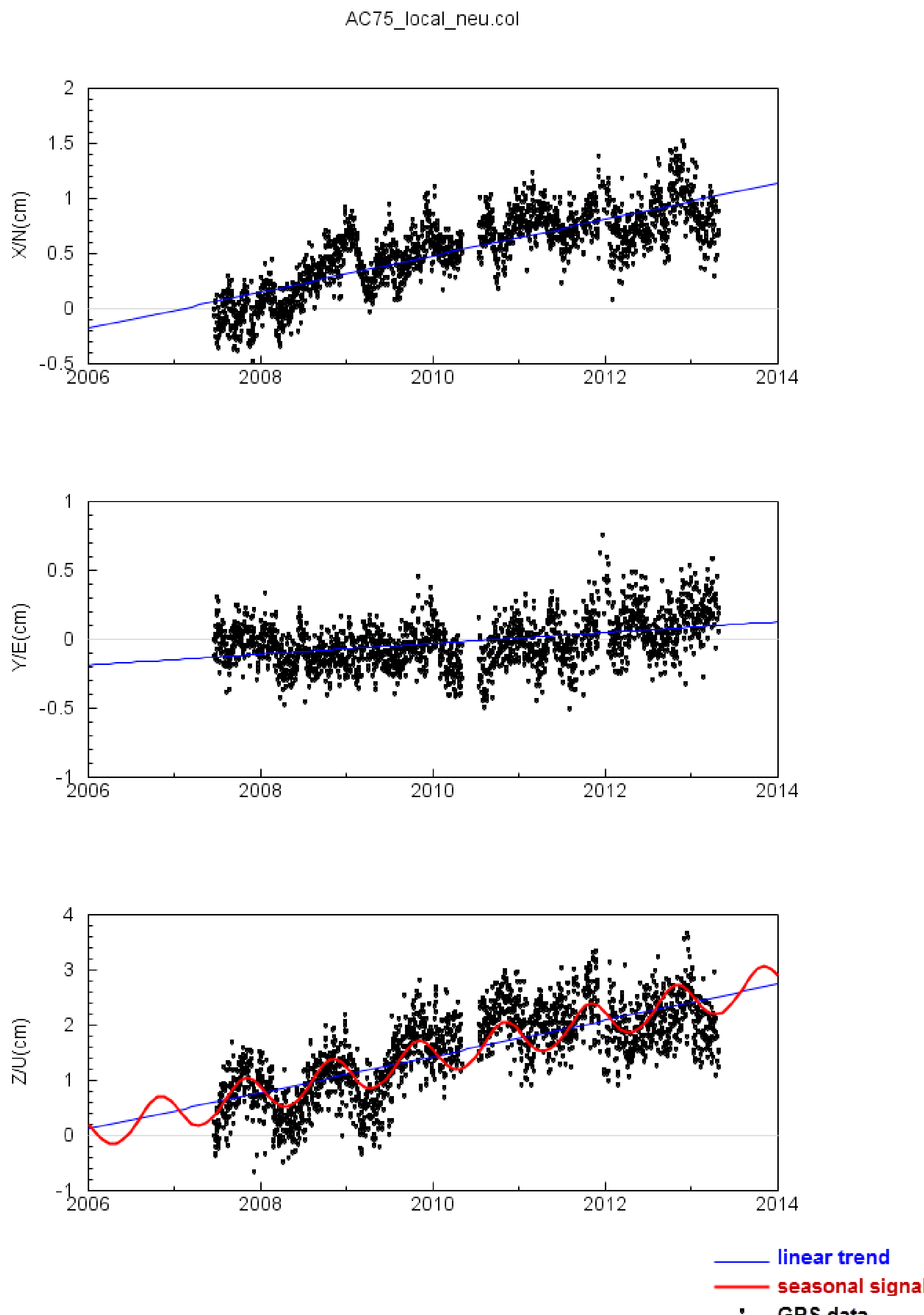

GPS three-component (X/N, Y/E, Z/U) positional time series. Raw GPS data that has been transformed to the local reference frame. No outliers have been removed. (North =positive X/N, South= negative X/N, East= positive Y/E, West= negative Y/E, rebound =positive Z/U, subsidence= negative Z/U).

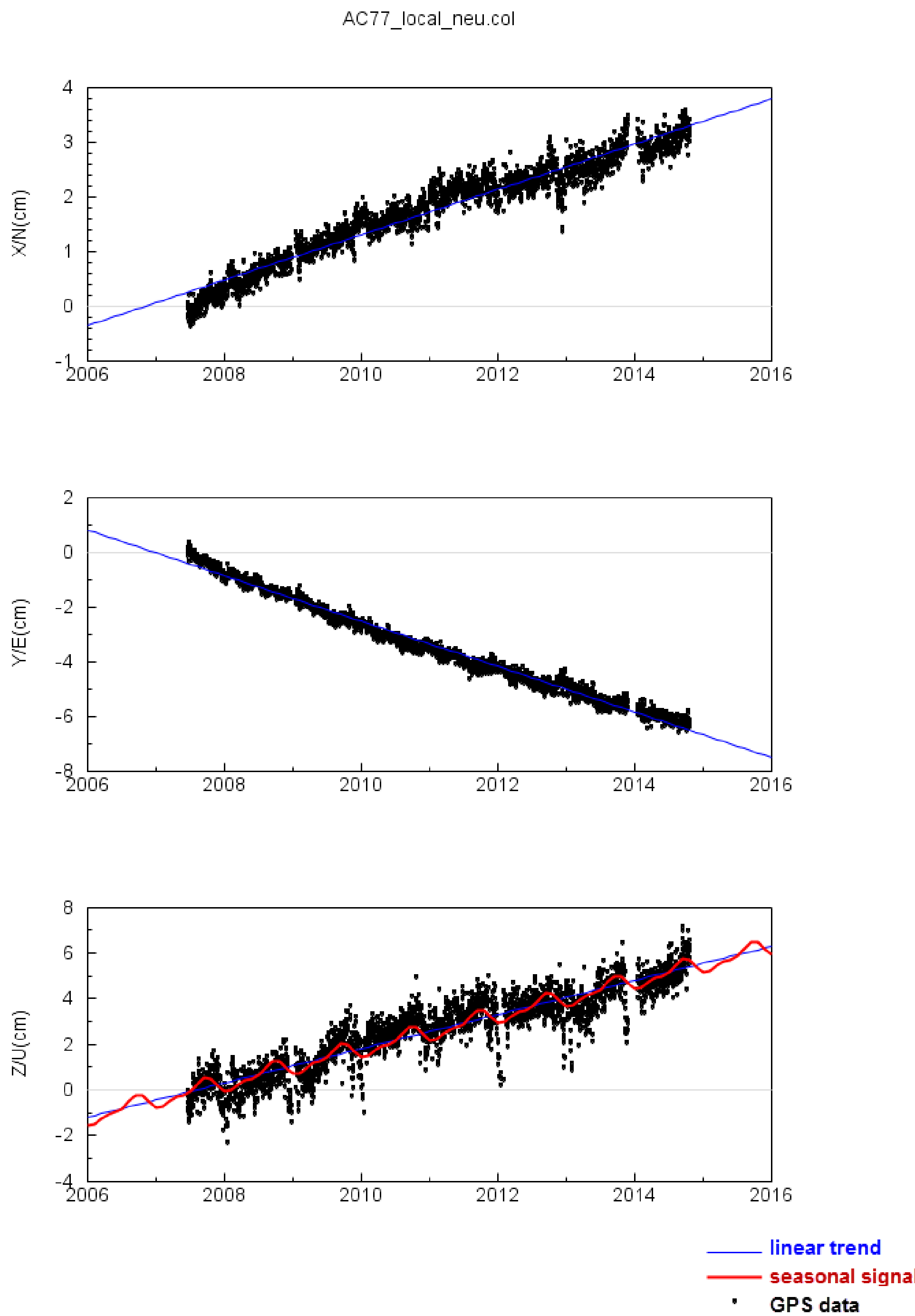

GPS three-component (X/N, Y/E, Z/U) positional time series. Raw GPS data that has been transformed to the local reference frame. No outliers have been removed. (North =positive X/N, South= negative X/N, East= positive Y/E, West= negative Y/E, rebound =positive Z/U, subsidence= negative Z/U).

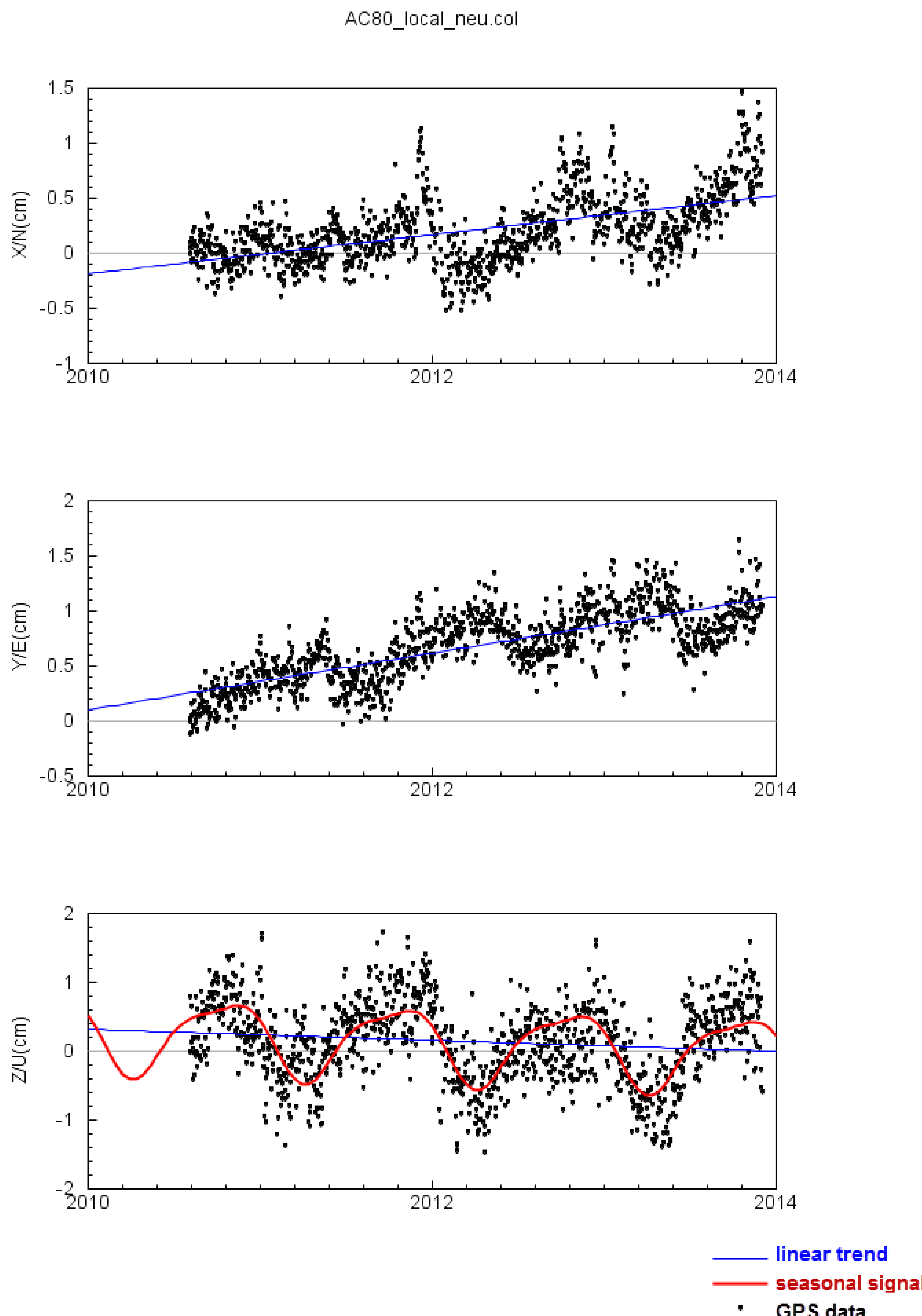

GPS three-component (X/N, Y/E, Z/U) positional time series. Raw GPS data that has been transformed to the local reference frame. No outliers have been removed. (North =positive X/N, South= negative X/N, East= positive Y/E, West= negative Y/E, rebound =positive Z/U, subsidence= negative Z/U).

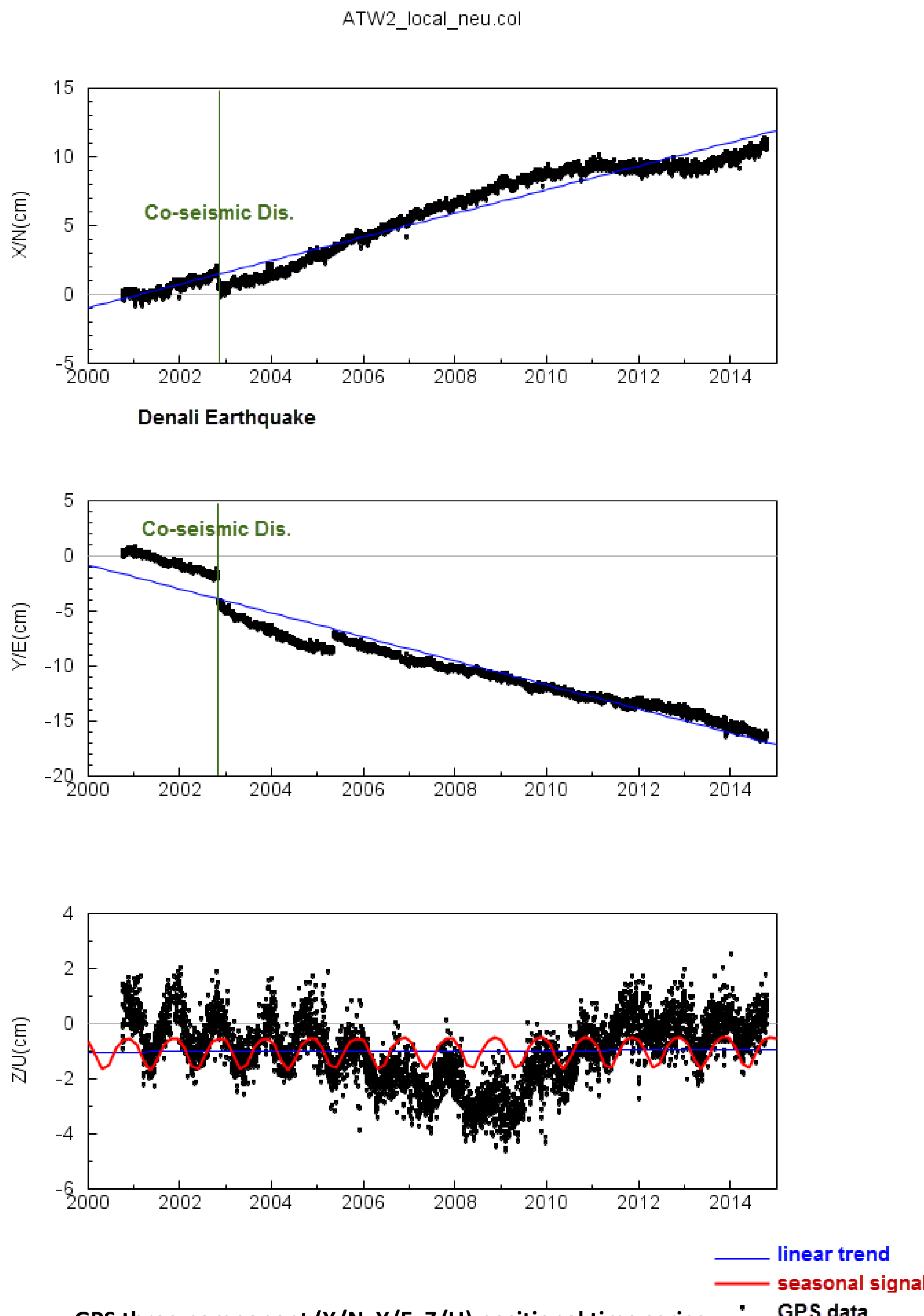

GPS three-component (X/N, Y/E, Z/U) positional time series. Raw GPS data that has been transformed to the local reference frame. No outliers have been removed. (North =positive X/N, South= negative X/N, East= positive Y/E, West= negative Y/E, rebound =positive Z/U, subsidence= negative Z/U). Green line represents 2002 Denali Earthquake and the co-seismic displacement.

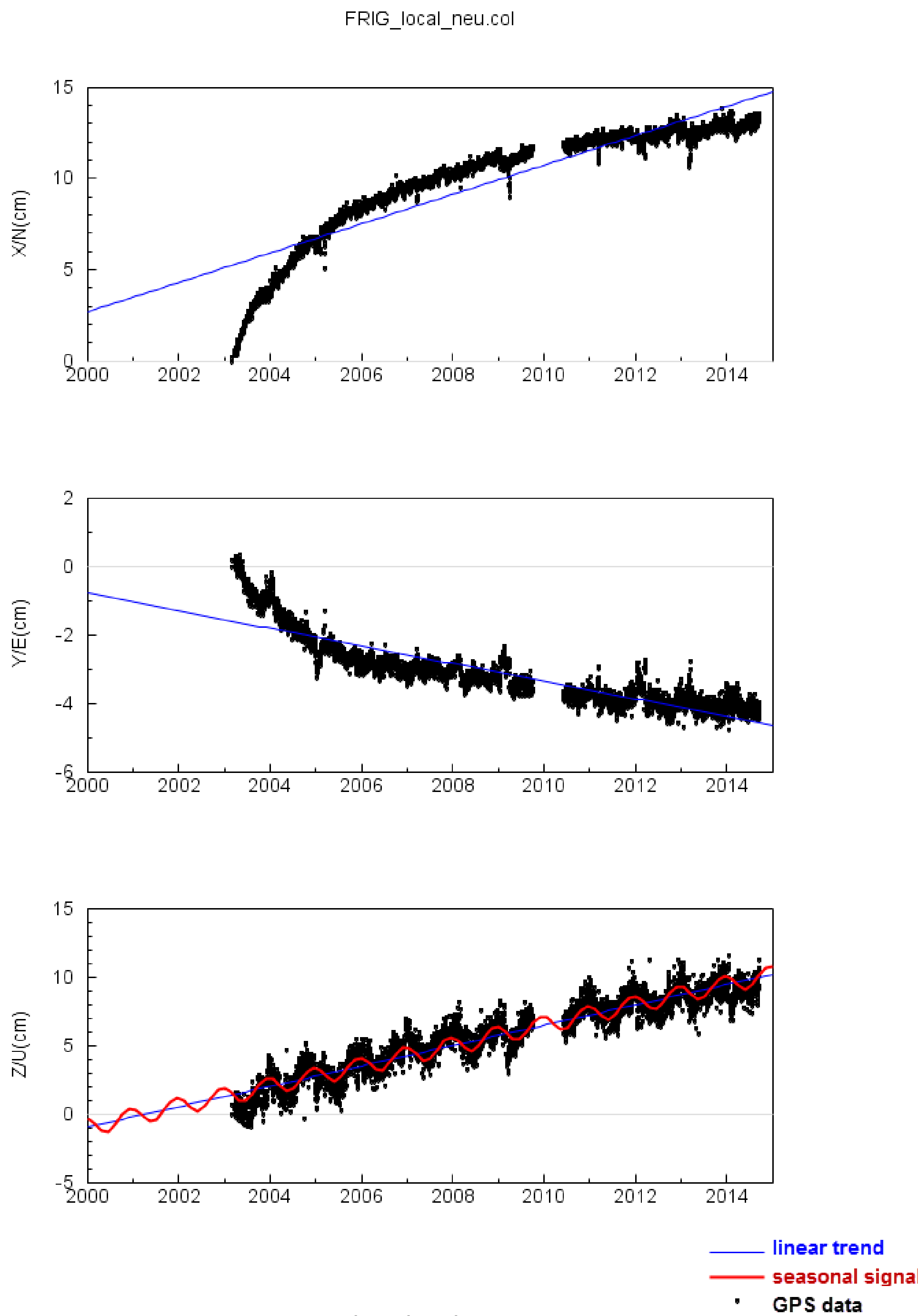

GPS three-component (X/N, Y/E, Z/U) positional time series. Raw GPS data that has been transformed to the local reference frame. No outliers have been removed. (North =positive X/N, South= negative X/N, East= positive Y/E, West= negative Y/E, rebound =positive Z/U, subsidence= negative Z/U).

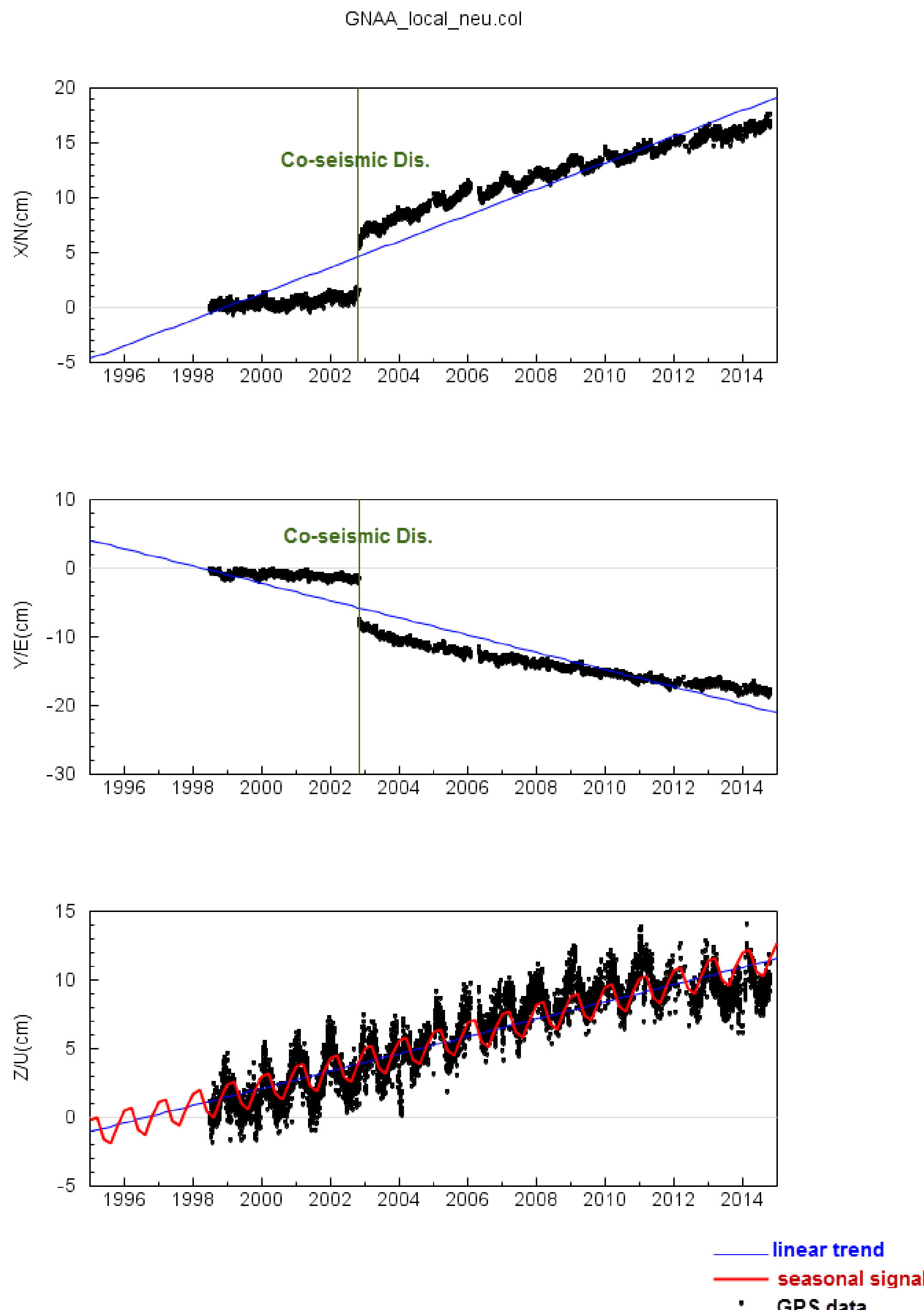

GPS three-component (X/N, Y/E, Z/U) positional time series. Raw GPS data that has been transformed to the local reference frame. No outliers have been removed. (North =positive X/N, South= negative X/N, East= positive Y/E, West= negative Y/E, rebound =positive Z/U, subsidence= negative Z/U). Green line represents 2002 Denali Earthquake and the co-seismic displacement.

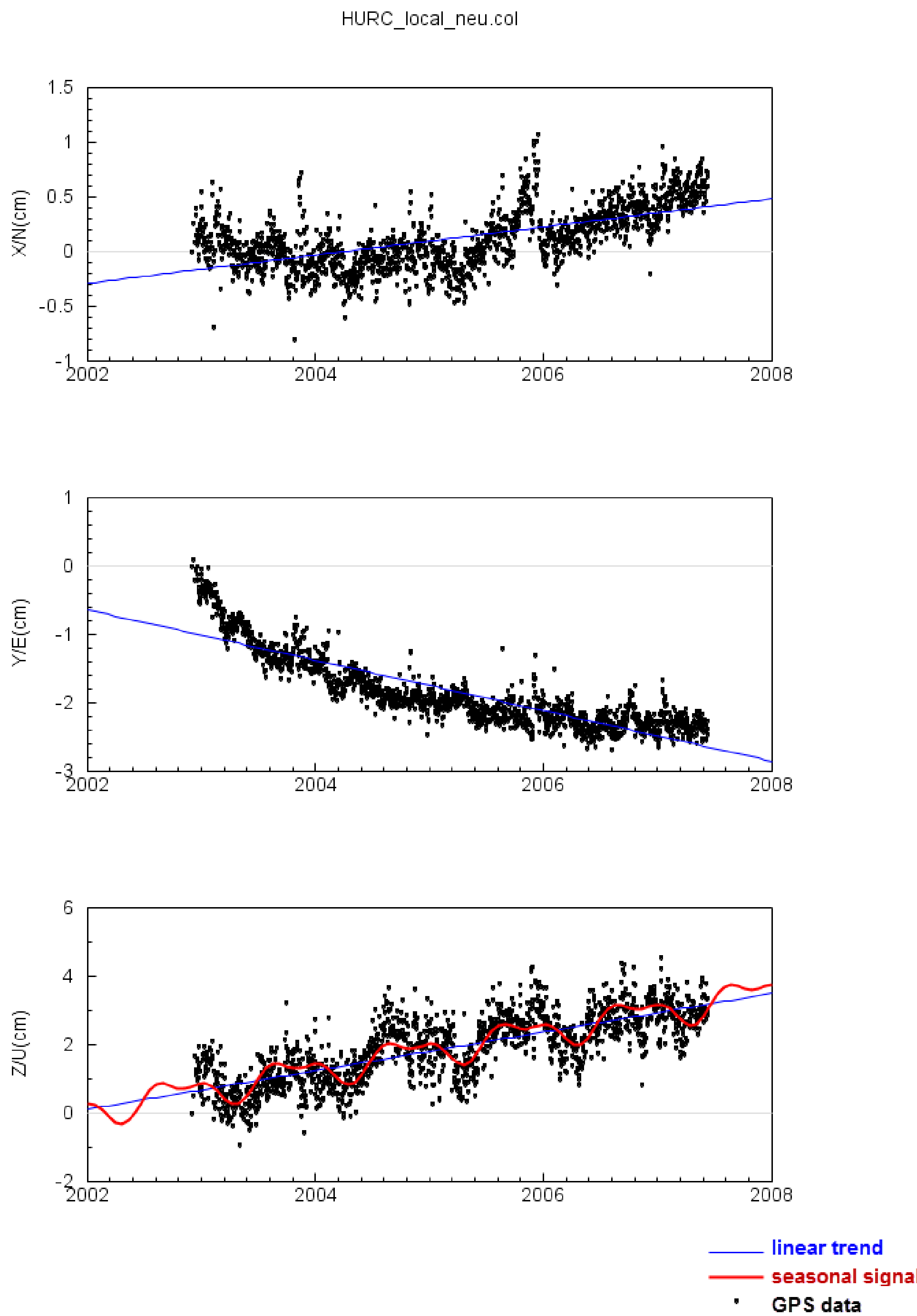

GPS three-component (X/N, Y/E, Z/U) positional time series. Raw GPS data that has been transformed to the local reference frame. No outliers have been removed. (North =positive X/N, South= negative X/N, East= positive Y/E, West= negative Y/E, rebound =positive Z/U, subsidence= negative Z/U).

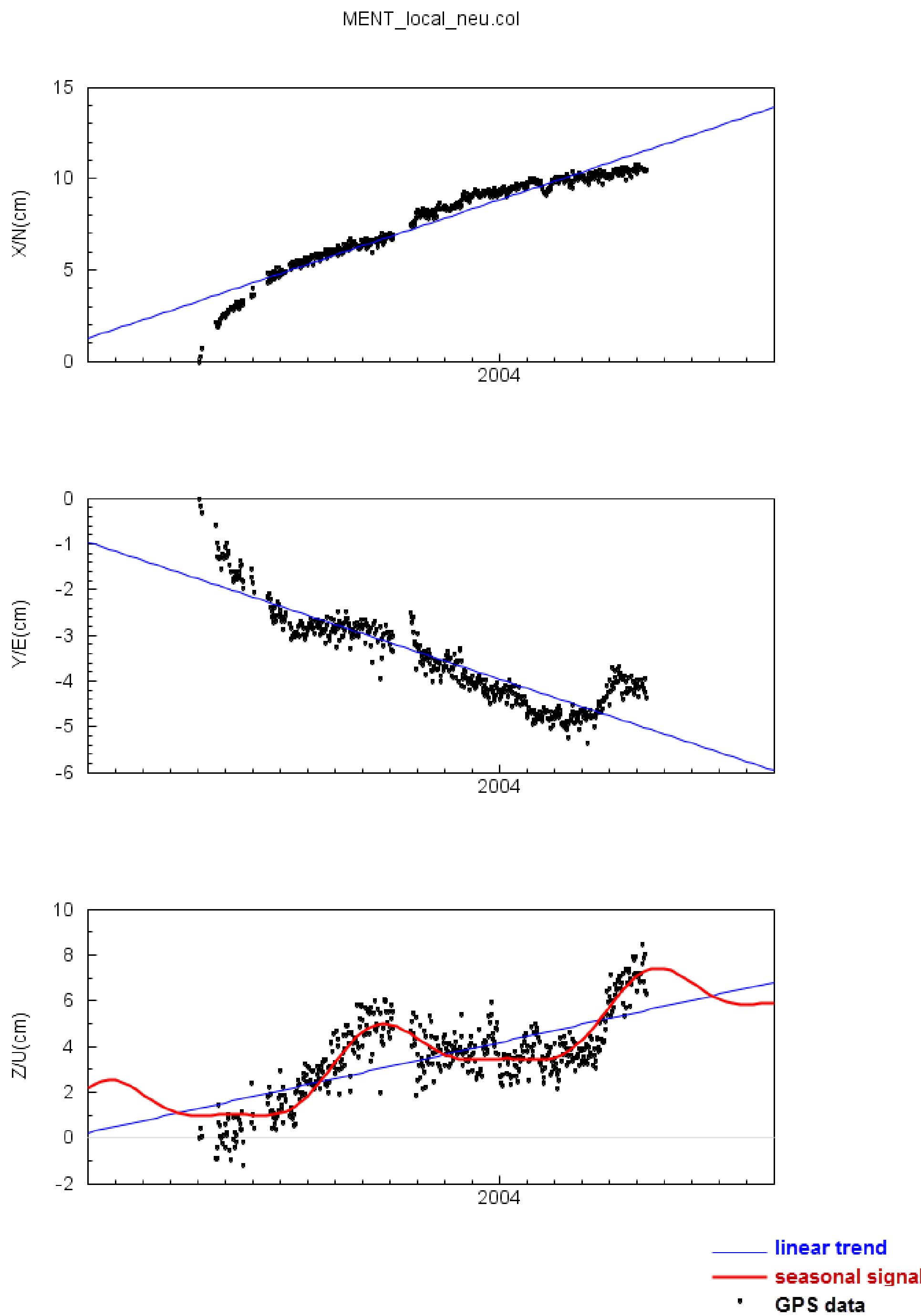

GPS three-component (X/N, Y/E, Z/U) positional time series. Raw GPS data that has been transformed to the local reference frame. No outliers have been removed. (North =positive X/N, South= negative X/N, East= positive Y/E, West= negative Y/E, rebound =positive Z/U, subsidence= negative Z/U).

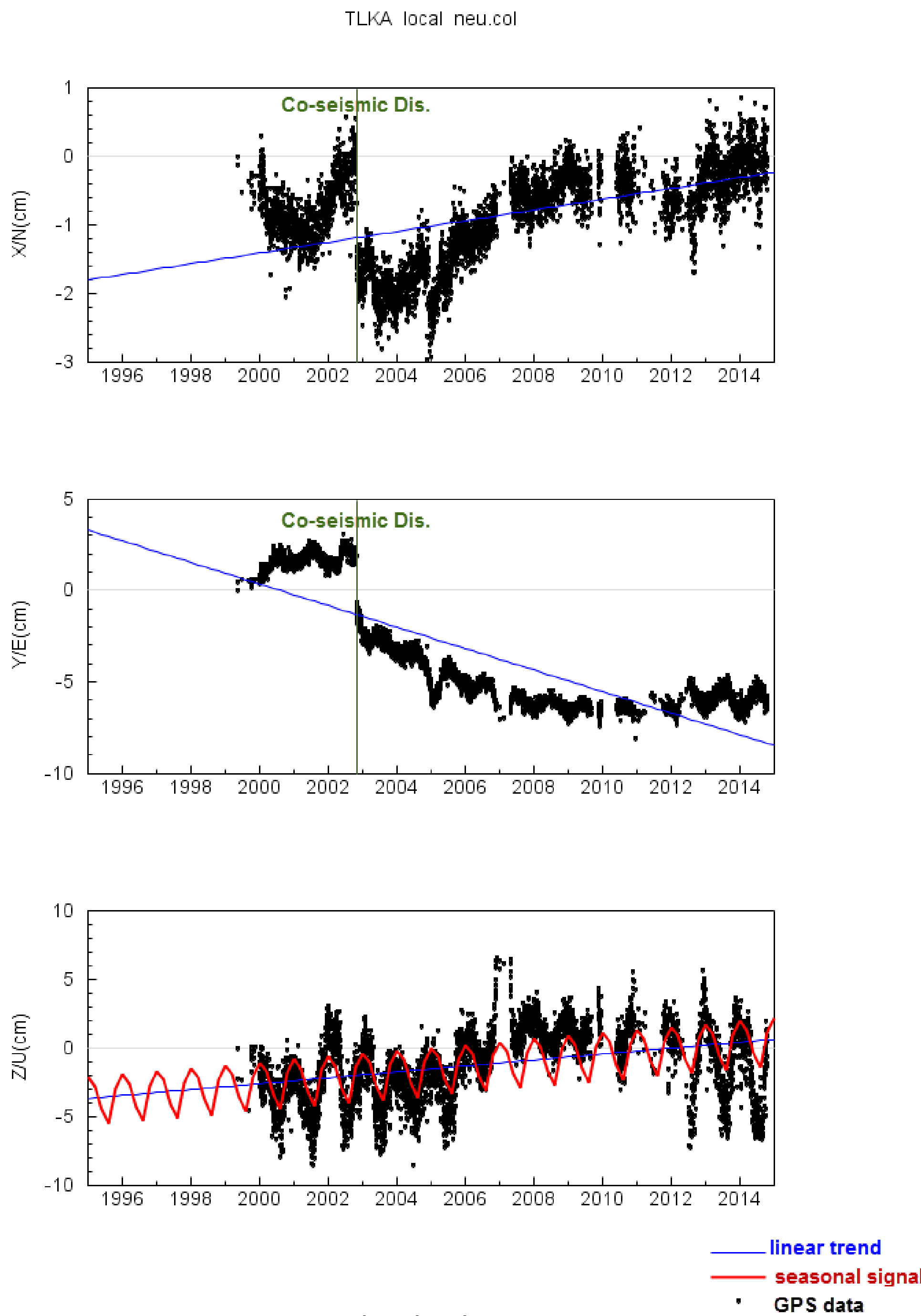

GPS three-component (X/N, Y/E, Z/U) positional time series. Raw GPS data that has been transformed to the local reference frame. No outliers have been removed. (North =positive X/N, South= negative X/N, East= positive Y/E, West= negative Y/E, rebound =positive Z/U, subsidence= negative Z/U). Green line represents 2002 Denali Earthquake and the co-seismic displacement.

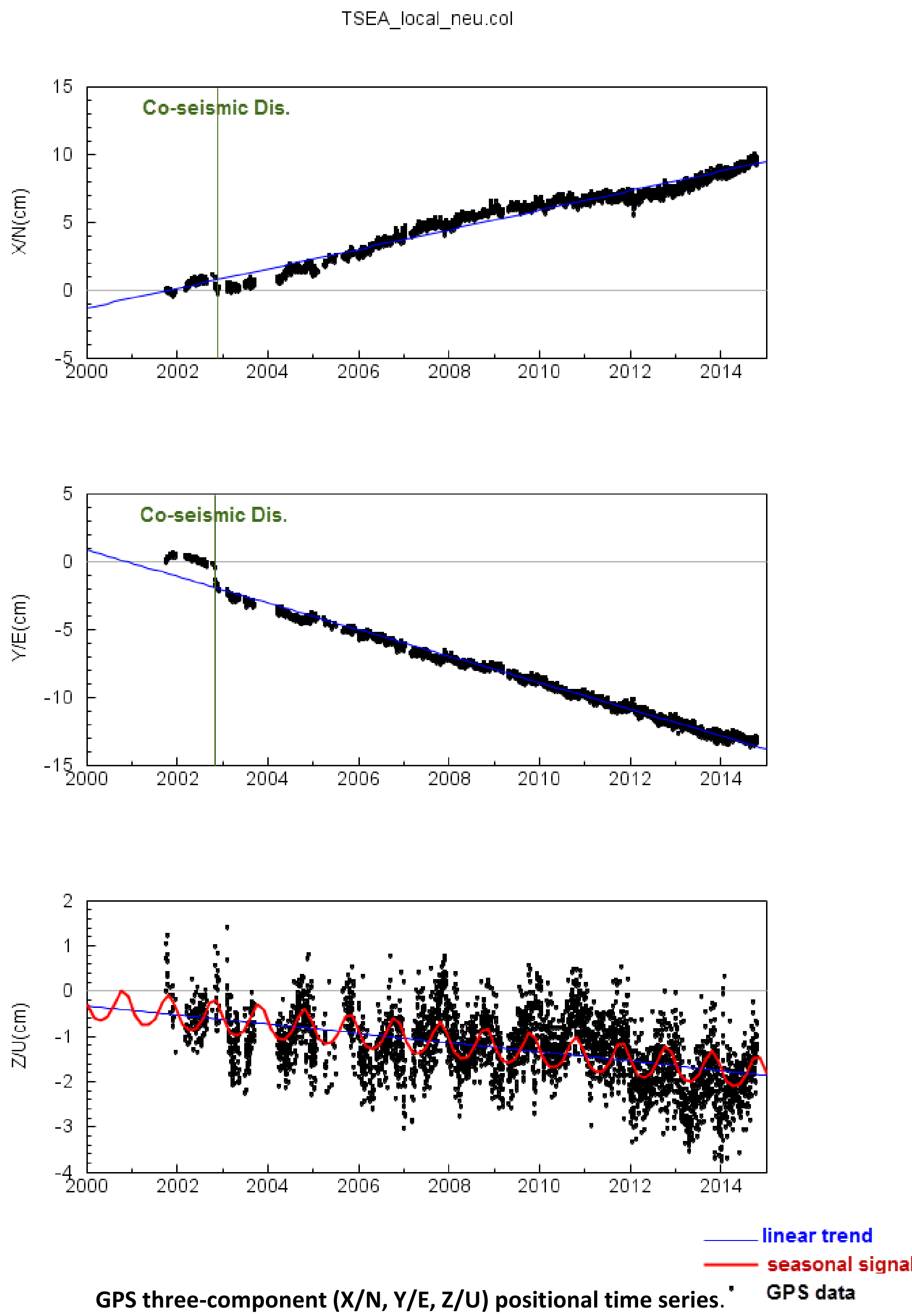

GPS three-component (X/N, Y/E, Z/U) positional time series. Raw GPS data that has been transformed to the local reference frame. No outliers have been removed. (North =positive X/N, South= negative X/N, East= positive Y/E, West= negative Y/E, rebound =positive Z/U, subsidence= negative Z/U). Green line represents 2002 Denali Earthquake and the co-seismic displacement.

APPENDIX C - GPS DISPLACEMENT RATES AND ERROR VALUES

Three-component displacement rates (Disp.Rate) for 20 GPS stations, in the global (IGS08) and local reference frames. Displacement rates and error (2σ) bar values given in cm/year. No outliers have been removed.

Station	Duration	Comp.	RF	Disp.Rate	Error	RF	Disp.Rate	Error
AB28	2006-2014	North	IGS08	-2.82	± 0.0034	LOCAL	+0.30	± 0.0032
		East		-0.66	± 0.0041		+0.30	± 0.0034
		Vertical		+0.47	± 0.0109		-0.14	± 0.0100
AB37	2004-2014	North	IGS08	-0.77	± 0.0044	LOCAL	+0.44	± 0.0043
		East		-2.79	± 0.0069		-1.11	± 0.0064
		Vertical		+0.62	± 0.0071		+0.81	± 0.0069
AC19	2008-2014	North	IGS08	-2.60	± 0.0049	LOCAL	+0.74	± 0.0046
		East		-0.62	± 0.0042		+0.52	± 0.0039
		Vertical		+0.28	± 0.0158		-0.24	± 0.0144
AC32	2007-2014	North	IGS08	-2.41	± 0.0014	LOCAL	+0.16	± 0.0066
		East		-0.96	± 0.0012		-0.22	± 0.0058
		Vertical		+0.36	± 0.0021		-0.32	± 0.0165
AC46	2006-2014	North	IGS08	-2.74	± 0.0029	LOCAL	+0.05	± 0.0034
		East		-0.86	± 0.0035		+0.11	± 0.0028
		Vertical		+0.47	± 0.0011		-0.10	± 0.0098
AC51	2008-2014	North	IGS08	-2.82	± 0.0065	LOCAL	+0.05	± 0.0057
		East		-0.65	± 0.0042		+0.05	± 0.0037
		Vertical		0.67	± 0.0016		-0.08	± 0.0150
AC53	2006-2015	North	IGS08	-2.23	± 0.0048	LOCAL	+0.17	± 0.0048
		East		-1.15	± 0.0048		-0.23	± 0.0047
		Vertical		+0.22	± 0.0018		-0.32	± 0.0120
AC55	2006-2011	North	IGS08	-1.37	± 0.0016	LOCAL	+1.49	± 0.014
		East		+4.51	± 0.0036		+5.68	± 0.029
		Vertical		-2.24	± 0.0040		-2.69	± 0.038
AC62	2004-2014	North	IGS08	-1.20	± 0.0029	LOCAL	+0.23	± 0.0024
		East		-2.60	± 0.0054		-0.89	± 0.0052
		Vertical		+0.46	± 0.0072		+0.62	± 0.0069
AC65	2004-2014	North	IGS08	+0.18	± 0.0075	LOCAL	+0.93	± 0.0085
* replaced MENT		East		-2.02	± 0.0057		-0.39	± 0.0053
		Vertical		+0.96	± 0.0019		+1.25	± 0.0182
MENT	2002-2004	North	IGS08	+4.29	± 0.0016	LOCAL	+5.05	± 0.1175
		East		-3.63	± 0.0010		-1.99	± 0.0851
		Vertical		+2.35	± 0.0023		+2.64	± 0.2459
AC70	2007-2014	North	IGS08	-1.90	± 0.0039	LOCAL	+0.02	± 0.0038
		East		-1.83	± 0.0038		-0.04	± 0.0036
		Vertical		+0.27	± 0.0016		+0.36	± 0.0131
AC74	2007-2014	North	IGS08	-1.95	± 0.0041	LOCAL	+0.14	± 0.0041
		East		-1.42	± 0.0033		+0.44	± 0.0033
		Vertical		+0.27	± 0.0013		+0.37	± 0.0115

Station	Duration	Compo nent	Referen ce	Displaceme nt	Error (2σ)	Reference	Displaceme nt	Error (2σ)
AC75 * replaced HURC	2008-2013	North East Vertical	IGS08	-2.13 -1.54 +0.43	± 0.0039 ± 0.0033 ± 0.0012	LOCAL	+0.16 +0.04 +0.33	± 0.0055 ± 0.0041 ± 0.0135
HURC	2003-2007	North East Vertical	IGS08	-2.16 -1.95 +0.67	± 0.0090 ± 0.0012 ± 0.0030	LOCAL	+0.13 -0.37 +0.56	± 0.0083 ± 0.0103 ± 0.0244
AC77	2008-2014	North East Vertical	IGS08	-0.79 -2.37 +0.65	± 0.0045 ± 0.0041 ± 0.0022	LOCAL	+0.41 -0.83 +0.75	± 0.0043 ± 0.0041 ± 0.0133
AC80	2010-2015	North East Vertical	IGS08	-2.68 -0.92 +0.37	± 0.0098 ± 0.0077 ± 0.0025	LOCAL	+0.18 +0.26 -0.08	± 0.0159 ± 0.0123 ± 0.0349
ATW2	2000-2015	North East Vertical	IGS08	-1.30 -1.96 +0.53	± 0.0052 ± 0.0079 ± 0.0084	LOCAL	+0.86 -1.09 +0.00	± 0.0056 ± 0.0083 ± 0.0082
FRIG	2003-2014	North East Vertical	IGS08	+0.23 -1.68 +0.53	± 0.0017 ± 0.0063 ± 0.0010	LOCAL	+0.80 -0.26 +0.74	± 0.0111 ± 0.0043 ± 0.0087
GNAA	1998-2014	North East Vertical	IGS08	-0.15 -2.49 +0.75	± 0.0092 ± 0.0012 ± 0.0097	LOCAL	+1.19 -1.26 +0.63	± 0.0102 ± 0.0133 ± 0.0092
TLKA	1999-2014	North East Vertical	IGS08	-2.43 -1.78 +0.60	± 0.0038 ± 0.0012 ± 0.0019	LOCAL	+0.08 -0.59 +0.21	± 0.0040 ± 0.0125 ± 0.0165
TSEA	2002-2015	North East Vertical	IGS08	-1.64 -1.61 +0.61	± 0.0045 ± 0.0043 ± 0.0066	LOCAL	+0.72 -0.98 -0.10	± 0.0049 ± 0.0037 ± 0.0063

APPENDIX D – LANDSAT COMPOSITE DATA

Combinations

Natural

Red (band 3) Green (band 2) and Blue (band 1)

This band combination represents the landscape in natural color. Band 3 detects chlorophyll absorption in vegetation (thus emitting a low reflection). Band 2 detects the green reflectance from vegetation. Band 1 represents water, differentiates between soil and vegetation.

Visible Near InfraRed (IR)

IR (band 4) Red (band 3) and Green (band 2)

These bands are combined to make a false color composite. From band 4 the high reflectance peak from vegetation is detected. The inclusion of IR, makes land water boundaries clearer and differentiates vegetation types. Bright red indicate healthy growning vegetation. Soils with no or sparse vegetation range from white (sand, salt) to green or browns depending on moisture and biomass content.

2002 Landsat ETM+

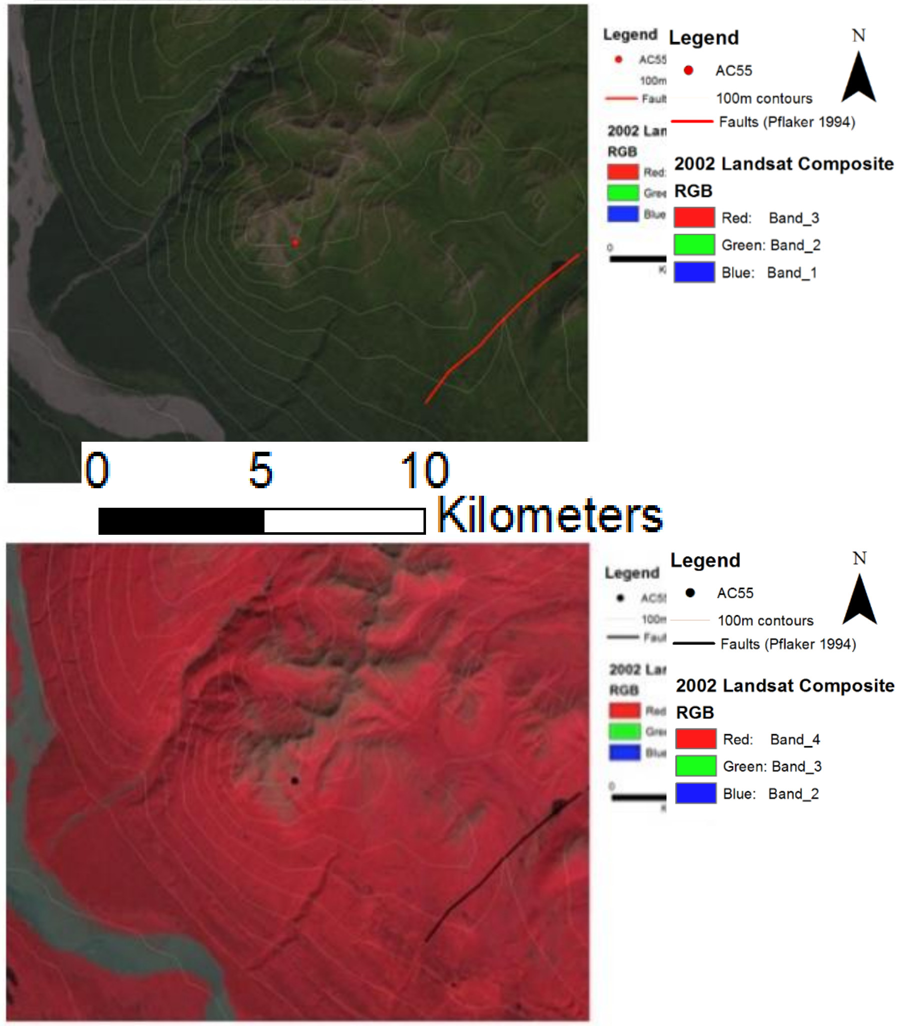

Appendix D: Landsat band combinations benefits and parameters. Individual bands can be composited in a Red, Green, and Blue (RGB) combination in order to visualize the data in color. There are many different combinations that can be made, and each has their own advantages and disadvantages. Above are some commonly used Landsat RGB band combinations (color composites), which image the GPS station AC55 but landslide extent is difficult to quantify from these composites.

Combinations

Visible Near IR and Short-wave IR

VNIR (band 4) SWIR (band 5) and Red (band 3)

This combination is crisper than the previous two images because the two shortest wavelength bands (bands 1 and 2) are not included. Different vegetation types can be more clearly defined and the land/water interface is very clear. Variations in moisture content are evident with this set of bands. This is probably the most common band combination for Landsat imagery.

Short-wave and Visible Near IR

SWIR (band 7) VNIR (band 4) and Green (band 2)

This has similar properties to the 4,5,3 band combination with the biggest difference being that vegetation is green. This is the band combination that was selected for the global Landsat mosaic created for NASA.

2002 Landsat ETM+

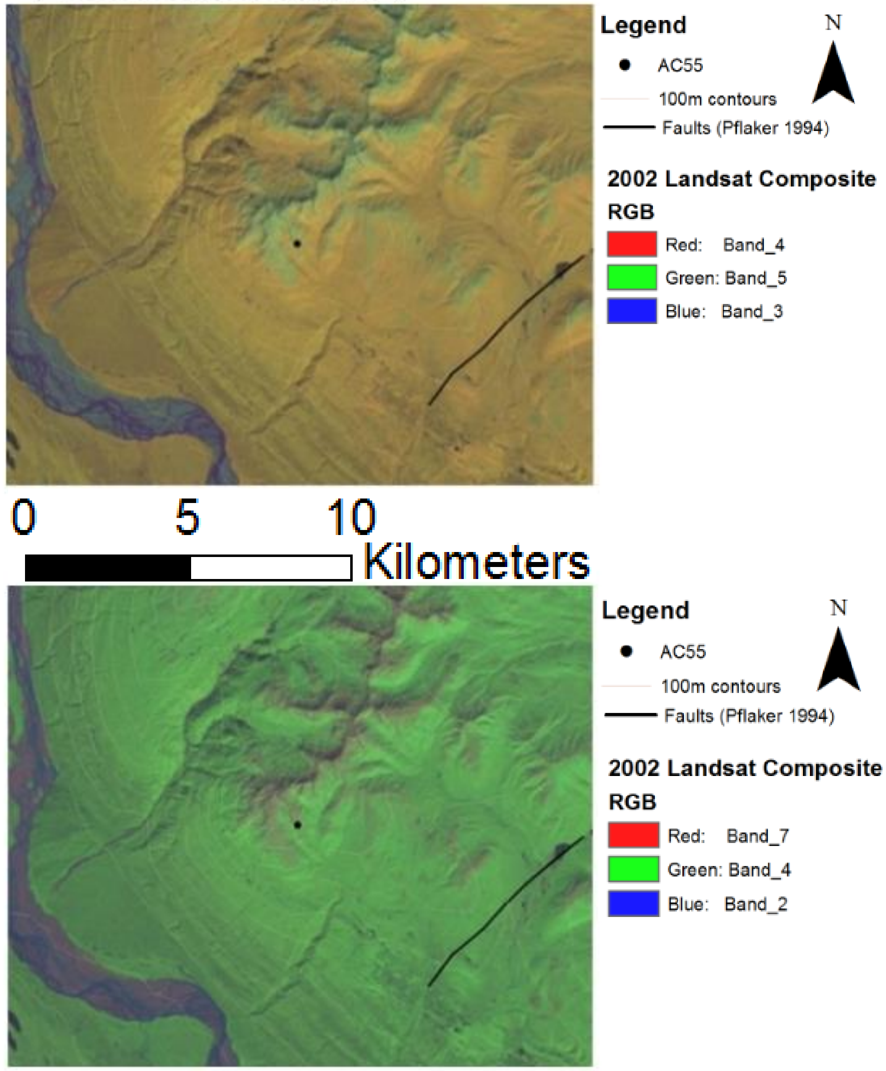

Combinations

2010 Landsat TM

Natural

Red (band 3) Green (band 2) and Blue (band 1)

This band combination represents the landscape in natural color. Band 3 detects chlorophyll absorption in vegetation (thus emitting a low reflection). Band 2 detects the green reflectance from vegetation. Band 1 represents water, differentiates between soil and vegetation.

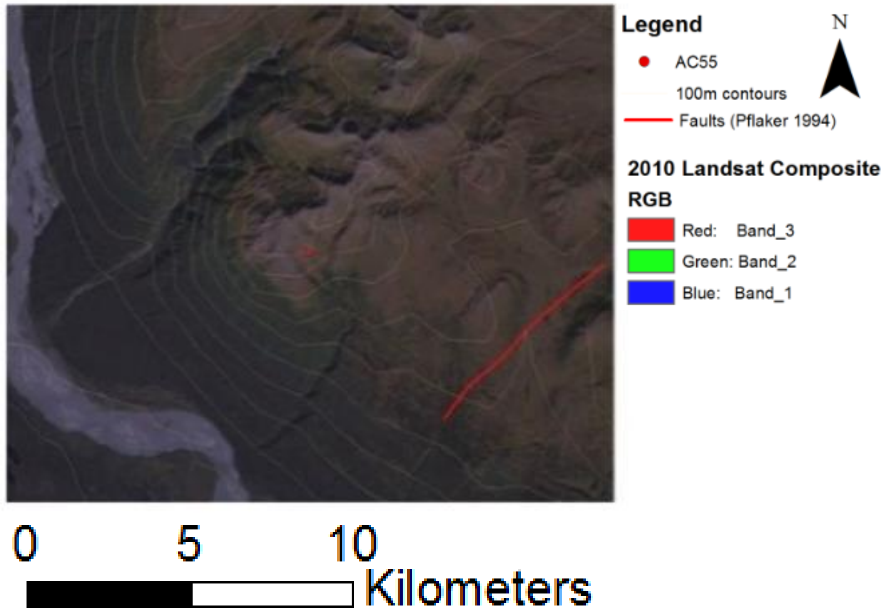

Visible Near InfraRed (IR)

IR (band 4) Red (band 3) and Green (band 2)

These bands are combined to make a false color composite. From band 4 the high reflectance peak from vegetation is detected. The inclusion of IR, makes land water boundaries clearer and differentiates vegetation types. Bright red indicate healthy growning vegetation. Soils with no or sparse vegetation range from white (sand, salt) to green or browns depending on moisture and biomass content.

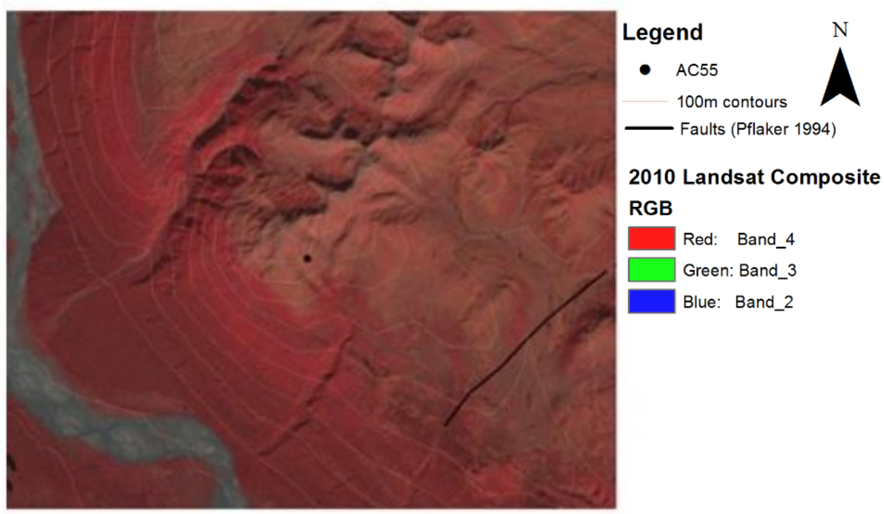

Combinations 2010 Landsat TM

Visible Near IR and Short-wave IR

VNIR (band 4) SWIR (band 5) and Red (band 3)

This combination is crisper than the previous two images because the two shortest wavelength bands (bands 1 and 2) are not included. Different vegetation types can be more clearly defined and the land/water interface is very clear. Variations in moisture content are evident with this set of bands. This is probably the most common band combination for Landsat imagery.

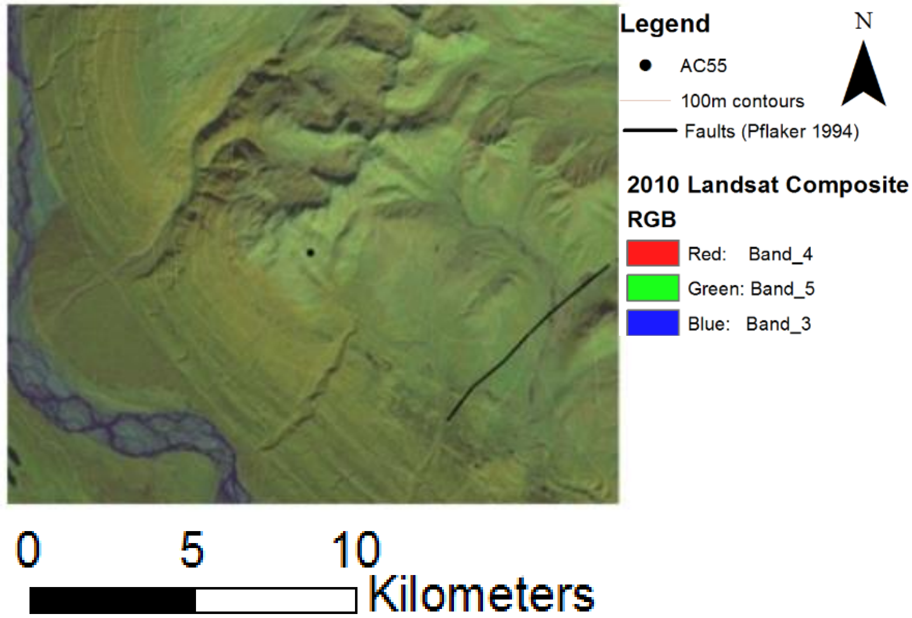

Short-wave and Visible Near IR

SWIR (band 7) VNIR (band 4) and Green (band 2)

This has similar properties to the 4,5,3 band combination with the biggest difference being that vegetation is green. This is the band combination that was selected for the global Landsat mosaic created for NASA.